

Advances in Characterization and Modeling of NanoReinforced Composites

Guest Editors: Roham Rafiee, Timon Rabczuk, Abbas S. Milani,
and Konstantinos I. Tserpes





Advances in Characterization and Modeling of NanoReinforced Composites

Advances in Characterization and Modeling of NanoReinforced Composites

Guest Editors: Roham Rafiee, Timon Rabczuk,
Abbas S. Milani, and Konstantinos I. Tserpes



Copyright © 2016 Hindawi Publishing Corporation. All rights reserved.

This is a special issue published in "Journal of Nanomaterials." All articles are open access articles distributed under the Creative Commons Attribution License, which permits unrestricted use, distribution, and reproduction in any medium, provided the original work is properly cited.

Editorial Board

- Domenico Acierno, Italy
Katerina Aifantis, USA
Nageh K. Allam, USA
Margarida Amaral, Portugal
Martin Andersson, Sweden
Raul Arenal, Spain
Ilaria Armentano, Italy
Vincenzo Baglio, Italy
Lavinia Balan, France
Thierry Baron, France
Andrew R. Barron, USA
Reza Bayati, USA
Hongbin Bei, USA
Daniel Bellet, France
Stefano Bellucci, Italy
Enrico Bergamaschi, Italy
Samuel Bernard, France
D. Bhattacharyya, New Zealand
Sergio Bietti, Italy
Giovanni Bongiovanni, Italy
T. Borca-Tasciuc, USA
Mohamed Bououdina, Bahrain
Torsten Brezesinski, Germany
C. Jeffrey Brinker, USA
Christian Brosseau, France
Philippe Caroff, Australia
V. M. Castaño, Mexico
Albano Cavaleiro, Portugal
Bhanu P. S. Chauhan, USA
Shafiul Chowdhury, USA
Jin-Ho Choy, Republic of Korea
Kwang-Leong Choy, UK
Yu-Lun Chueh, Taiwan
Elisabetta Comini, Italy
Giuseppe Compagnini, Italy
David Cornu, France
M. A. Correa-Duarte, Spain
P. Davide Cozzoli, Italy
Shadi A. Dayeh, USA
Luca Deseri, USA
Yong Ding, USA
Philippe Dubois, Belgium
Zehra Durmus, Turkey
Joydeep Dutta, Oman
Ali Eftekhari, USA
- Jeffrey Elam, USA
Samy El-Shall, USA
Ovidiu Ersen, France
Claude Estournès, France
Andrea Falqui, KSA
Matteo Ferroni, Italy
Elena J. Foster, USA
Ilaria Fratoddi, Italy
Alan Fuchs, USA
Miguel A. Garcia, Spain
Siddhartha Ghosh, Singapore
P. K. Giri, India
Russell E. Gorga, USA
Jihua Gou, USA
Jean M. Greneche, France
Smrati Gupta, Germany
Kimberly Hamad-Schifferli, USA
Simo-Pekka Hannula, Finland
Michael Harris, USA
Yasuhiko Hayashi, Japan
F. Hernandez-Ramirez, Spain
Michael Z. Hu, USA
Nay Ming Huang, Malaysia
Shaoming Huang, China
David Hui, USA
Zafar Iqbal, USA
Balachandran Jeyadevan, Japan
Xin Jiang, Germany
Rakesh Joshi, Australia
Jeong-won Kang, Republic of Korea
Hassan Karimi-Maleh, Iran
Antonios Kelarakis, UK
Alireza Khataee, Iran
Ali Khorsand Zak, Iran
Philippe Knauth, France
Ralph Krupke, Germany
Christian Kübel, Germany
Prashant Kumar, UK
Michele Laus, Italy
Eric Le Bourhis, France
Jun Li, Singapore
Meiyong Liao, Japan
Shijun Liao, China
Silvia Licoccia, Italy
Wei Lin, USA
- Nathan C. Lindquist, USA
Zainovia Lockman, Malaysia
Nico Lovergine, Italy
Jim Low, Australia
Jue Lu, USA
Ed Ma, USA
Laura M. Maestro, Spain
Gaurav Mago, USA
Muhamamd A. Malik, UK
Devanesan Mangalaraj, India
Sanjay R. Mathur, Germany
Tony McNally, UK
Yogendra Mishra, Germany
Paulo Cesar Morais, Brazil
Paul Munroe, Australia
Jae-Min Myoung, Republic of Korea
Rajesh R. Naik, USA
Albert Nasibulin, Russia
Toshiaki Natsuki, Japan
Koichi Niihara, Japan
Natalia Noginova, USA
Sherine Obare, USA
Won-Chun Oh, Republic of Korea
Atsuto Okamoto, Japan
Abdelwahab Omri, Canada
Ungyu Paik, Republic of Korea
Piersandro Pallavicini, Italy
Edward A. Payzant, USA
Alessandro Pegoretti, Italy
Ton Peijs, UK
O. Perales-Pérez, Puerto Rico
Jorge Pérez-Juste, Spain
Alexey P. Popov, Finland
Philip D. Rack, USA
Peter Reiss, France
Orlando Rojas, USA
Marco Rossi, Italy
Ilker S. Bayer, Italy
Cengiz S. Ozkan, USA
Sudipta Seal, USA
Shu Seki, Japan
V. Šepelák, Germany
Huaiyu Shao, Japan
Prashant Sharma, USA
Donglu Shi, USA



Bhanu P. Singh, India
Surinder Singh, USA
Vladimir Sivakov, Germany
Ashok Sood, USA
Adolfo Speghini, Italy
Marinella Striccoli, Italy
Xuping Sun, KSA
A. K. Sundramoorthy, USA
Angelo Taglietti, Italy
Bo Tan, Canada
Leander Tapfer, Italy
Valeri P. Tolstoy, Russia

M. S. Toprak, Sweden
R. Torrecillas, Spain
Achim Trampert, Germany
Takuya Tsuzuki, Australia
Tamer Uyar, Turkey
Bala Vaidhyanathan, UK
Luca Valentini, Italy
Rajender S. Varma, USA
Ester Vazquez, Spain
Antonio Villaverde, Spain
Ajayan Vinu, Australia
Ruibing Wang, Macau

Shiren Wang, USA
Yong Wang, USA
Magnus Willander, Sweden
Ping Xiao, UK
Zhi Li Xiao, USA
Yangchuan Xing, USA
Doron Yadlovker, Israel
Yoke K. Yap, USA
Kui Yu, Canada
William Yu, USA
Michele Zappalorto, Italy
Renyun Zhang, Sweden

Contents

Advances in Characterization and Modeling of Nanoreinforced Composites

Roham Rafiee, Timon Rabczuk, Abbas S. Milani, and Konstantinos I. Tserpes
Volume 2016, Article ID 9481053, 1 page

Micro/Nanostructure and Tribological Characteristics of Pressureless Sintered Carbon Nanotubes Reinforced Aluminium Matrix Composites

P. Manikandan, R. Sieh, A. Elayaperumal, H. R. Le, and S. Basu
Volume 2016, Article ID 9843019, 10 pages

Paraffin Nanocomposites for Heat Management of Lithium-Ion Batteries: A Computational Investigation

A. H. N. Shirazi, Farzad Mohebbi, M. R. Azadi Kakavand, B. He, and T. Rabczuk
Volume 2016, Article ID 2131946, 10 pages

Parametric Study of Strain Rate Effects on Nanoparticle-Reinforced Polymer Composites

B. Soltannia, I. Haji Gholami, S. Masajedian, P. Mertiny, D. Sameoto, and F. Taheri
Volume 2016, Article ID 9841972, 9 pages

An Overview on the Improvement of Mechanical Properties of Ceramics Nanocomposites

J. Silvestre, N. Silvestre, and J. de Brito
Volume 2015, Article ID 106494, 13 pages

In Situ Synthesis of Reduced Graphene Oxide-Reinforced Silicone-Acrylate Resin Composite Films Applied in Erosion Resistance

Yang Cao, Xiaoyong Tian, Yan Wang, Youyi Sun, Hailin Yu, Dian-sen Li, and Yaqing Liu
Volume 2015, Article ID 405087, 8 pages

Investigation of Theoretical Models for the Elastic Stiffness of Nanoparticle-Modified Polymer Composites

T. Thorvaldsen, B. B. Johnsen, T. Olsen, and F. K. Hansen
Volume 2015, Article ID 281308, 17 pages

Editorial

Advances in Characterization and Modeling of Nanoreinforced Composites

Roham Rafiee,¹ Timon Rabczuk,² Abbas S. Milani,³ and Konstantinos I. Tserpes⁴

¹Composites Research Laboratory, Faculty of New Sciences & Technologies, University of Tehran, Tehran 14399 57131, Iran

²Institute of Structural Mechanics, Bauhaus University, Weimar, Marienstraße 15, 99423 Weimar, Germany

³Composites Research Network-Okanagan Laboratory, University of British Columbia, Kelowna, BC, Canada V1V 1V7

⁴Laboratory of Technology & Strength of Materials, Department of Mechanical Engineering & Aeronautics, University of Patras, 26500 Patras, Greece

Correspondence should be addressed to Roham Rafiee; roham.rafiee@ut.ac.ir

Received 22 February 2016; Accepted 22 February 2016

Copyright © 2016 Roham Rafiee et al. This is an open access article distributed under the Creative Commons Attribution License, which permits unrestricted use, distribution, and reproduction in any medium, provided the original work is properly cited.

Exceptional mechanical, electrical, and thermal properties of nanoreinforced materials as well as their low density and high aspect ratios have now rendered them among desired reinforcing agents in a wide range of composites in high tech applications. The experimental measurement of nanoreinforced material properties, however, is still a challenging and tedious task. Extremely scattered data obtained through experimental observations, which often originated from different processing limitations, have led many researchers to pursue also analytical studies on the effective properties of nanoreinforcements and their corresponding composites. Consequently, next to experimental investigations, simulation and modeling techniques currently play a significant role in characterizing nanocomposites properties and understanding their mechanical behavior via atomistic modeling, continuum mechanics-based approach, and multiscale modeling techniques, among others.

Characterization of nanocomposites is often aimed at gaining knowledge on their global response, such as the macrodisplacement and stress fields at boundaries of a representative volume element. The continuum mechanics approaches are known to be adequate and sufficient for modeling nanocomposites within this scope. However, for more elaborated and in-depth analyses, the multiscale modeling techniques may be considered where the molecular dynamics and continuum mechanics models are integrated in a virtual computing environment. This approach would be detailed enough to account for the material physics at nanoscale, while

efficient enough to handle the field variables of interest at larger length scales.

This special issue deals with a range of recently developed characterization and modeling techniques employed to better understand and predict the response of nanoreinforced composites at different scales.

Acknowledgments

The guest editors would like to take this opportunity to express their sincere appreciations for the great work and contributions of all authors. They are also grateful to referees of the journal for their valuable time and constructive feedback during the review process of this special issue.

Roham Rafiee
Timon Rabczuk
Abbas S. Milani
Konstantinos I. Tserpes

Research Article

Micro/Nanostructure and Tribological Characteristics of Pressureless Sintered Carbon Nanotubes Reinforced Aluminium Matrix Composites

P. Manikandan,¹ R. Sieh,² A. Elayaperumal,¹ H. R. Le,³ and S. Basu²

¹Department of Mechanical Engineering, Anna University, Chennai 600 025, India

²School of Marine Science and Engineering, Plymouth University, Plymouth PL4 8AA, UK

³Department of Engineering, University of Derby, Derby DE22 3AW, UK

Correspondence should be addressed to H. R. Le; h.le@derby.ac.uk

Received 19 November 2015; Accepted 19 January 2016

Academic Editor: Roham Rafiee

Copyright © 2016 P. Manikandan et al. This is an open access article distributed under the Creative Commons Attribution License, which permits unrestricted use, distribution, and reproduction in any medium, provided the original work is properly cited.

This study reports the manufacture, microstructure, and tribological behaviour of carbon nanotube reinforced aluminium composites against pure aluminium. The specimens were fabricated using powder metallurgy method. The nanotubes in weight percentages of 0.5, 1.0, 1.5, and 2.0 were homogeneously dispersed and mechanically alloyed using a high energy ball milling. The milled powders were cold compacted and then isothermally sintered in air. The density of all samples was measured using Archimedes method and all had a relative density between 92.22% and 97.74%. Vickers hardness increased with increasing CNT fraction up to 1.5 wt% and then reduced. The microstructures and surfaces were investigated using high resolution scanning electron microscope (SEM). The tribological tests showed that the CNT reinforced composites displayed lower wear rate and friction coefficient compared to the pure aluminium under mild wear conditions. However, for severe wear conditions, the CNT reinforced composites exhibited higher friction coefficient and wear rate compared to the pure aluminium. It was also found that the friction and wear behaviour of CNT reinforced composites is significantly dependent on the applied load and there is a critical load beyond which CNTs could have adverse impact on the wear resistance of aluminium.

1. Introduction

Metal matrix composites (MMCs) reinforced with nanoparticles and nanotubes are finding increasing use in fields such as aerospace, architectural structure, renewable energy, alternative transport, and electronics in order to make lighter and stronger structures [1–3]. Among various MMCs, aluminium (Al) has attracted significant interest because of its excellent strength, low density, and corrosion resistance. Aluminium and its alloys are important lightweight materials with low density, high thermal conductivity, good mechanical properties, and corrosion resistance. The combination of unique properties of carbon nanotubes (CNTs) and aluminium alloys has, therefore, great potential in many weight sensitive applications [4, 5]. Since poor tribological performance limits its use in wear related applications, many efforts have been made to improve their wear and mechanical

resistance [4, 6]. Recent research has been extended to evaluate the effect of nanoparticles on the wear resistance of aluminium nanocomposites. There has been significant interest in carbon materials because of their special electrical, optical, and mechanical properties [7]. In particular, CNTs have attracted scientific and technological interest due to their unique chemical and physical properties. CNTs have also been proposed as a reinforcement material due to its high modulus of elasticity, high tensile strength, and large bending angles after being discovered by Iijima [8]. In particular, if the CNTs composite is made with aluminium matrix, it can inherit the lightweight property of aluminium [9]. To use CNTs for technical applications, the mechanical properties and characteristics of tribology need to be investigated through determination of the wettability between materials, the CNTs content, the homogeneous dispersion conditions, and the proper manufacturing method

[10, 11]. Several methods have been proposed and implemented to synthesize nanocrystalline matrix reinforced with multiwalled carbon nanotubes (MWCNTs), such as thermal spraying [12, 13], sintering [14–16], mechanical alloying (MA) [17–22], semisolid powder processing [23, 24], spark plasma sintering (SPS) [25, 26], friction stir processing [27, 28], flake powder metallurgy [29], spark plasma extrusion [30], and nanoscale dispersion [31]. However, the use of MWCNTs as reinforcement in aluminium MMCs is a great challenge due to their agglomeration and poor dispersion of the nanotubes. Among the aforementioned methods, SPS appears to be best for mechanical properties but requires expensive equipment. Pressureless sintering process is more economical and has the potential to produce large components. MA is employed prior to sintering or SPS to improve the dispersion of nanoparticles within metal matrices [32]. Improvement in wear resistance of aluminium with the addition of CNTs was reported in previous studies [4, 32, 33]. Al-Qutub et al. [4] clarified that the friction and wear behaviour of Al-CNTs composites is largely dependent on the applied load. There exists a critical load beyond which CNTs could have adverse impact on the wear resistance of aluminium alloys. Choi and coworkers [32] investigated the mechanical properties and wear mechanisms of aluminium nanocomposites. They found that aluminium infiltrated MWCNTs formed a strong interface with the aluminium matrix by mechanical interlocking. The strength and wear resistance were significantly improved due to the decrease of grain size and the addition of CNTs. The coefficient of friction was also reduced. The optimum CNTs content for minimum wear loss was reported to be 4.5 vol%. They also reported that the coefficient of friction and the wear rate increased with increasing load but decreased with increasing sliding speed. Zhou and coworkers [33] developed aluminium composites with CNTs via pressureless infiltration of aluminium into CNT-Mg-Al composite preformed in N_2 atmosphere at $800^\circ C$. They found that CNTs were well dispersed and embedded in the Al matrix and the friction coefficient and wear rate of the composite decreased with increasing volume fraction of CNTs content. It can therefore be summarised that the tribological properties of Al-CNTs composites are highly dependent on the method used for dispersing CNTs, the CNTs content, and the fabrication method used to consolidate the composite. Mechanical alloying (MA), also known as ball milling, is a process which has been highly developed and widely applied to preparing a wide range of alloys, intermetallic compounds, and composites in the amorphous or nanocrystalline form. Some alloys with homogenous microstructure can be readily obtained by MA from components having significant difference in specific weight and melting point or being even virtually immiscible [34]. MA is a powder metallurgy processing technique that involves repeated cold welding, fracturing, and rewelding of particles using a high energy ball mill [35]. It can be used to achieve a uniform distribution of the reinforcement in metal matrix nanocomposites (MMNCs) with reduced agglomeration. It was found that dispersion of CNTs in MMNCs through MA is related to several processing variables including pretreatment of CNTs, type of milling, ball-to-powder weight ratio, milling speed, milling time,

TABLE 1: Chemical composition of aluminium powder.

Element	Si	Cu	N	HCl	Fe	Mn	Ti	Al
Amount (%)	0.1	0.02	0.001	0.005	0.1	0.02	0.03	Balance

and process control agent [36]. Bakshi and coworkers [37] reviewed that most of the corrosion studies are performed on electrodeposited Ni-CNT composite coatings and Zn-CNT composite coating. They reported that electrodeposited coatings are more prone to corrosion due to the presence of pores and voids. These studies indicate that the addition of CNTs may improve the corrosion resistance due to two reasons. Firstly, the chemical inertness of the CNTs helps forming a passive layer on the coating surface. Secondly, CNTs help filling up the voids and pores of electrodeposited coatings reducing initiation of localised corrosion. The aim of the present study is to compare the hardness, density, microstructure, and sliding wear properties of Al-based composites fabricated by MA using a high energy ball mill. These composites were reinforced with various CNTs contents (0.5–2 wt%) based on previous works. Test samples were obtained by cold compaction and sintering from ball milled powders. Vickers hardness and density are obtained by established methods. Wear behaviour of the specimens was tested against steel discs using various loads in 300 m of sliding distance. Unless otherwise specified, CNTs in this work are referred to as MWCNTs.

2. Experimental Procedure

2.1. Materials. The matrix material used for the composite fabrication was pure Al (99.7%) powder with near spherical particle average sizes of $78 \mu m$ obtained from Loba Chemie in Mumbai, India. MWCNTs with a nominal diameter of 20–30 nm in lengths of 3–8 μm were used as reinforcement to the matrix. These were obtained from Intelligent Materials Private Ltd., a supplier in Punjab, India, for Nanoshel, a company based in the United States. Ethanol was used as a medium in the ball milling of CNT and Al powders. The chemical composition of Al powder is presented in Table 1.

2.2. Fabrication of Nanocomposite Material. Elemental powders were used to fabricate the aluminium. CNTs with a diameter in the range of 20–30 nm and length of 1–10 μm were added in 0.5, 1.0, 1.5, and 2.0 wt%. The CNTs were dispersed into the aluminium powder by ball milling for 2 hours. The ball-to-powder weight ratio was 10:1. The milled powders were cold pressed in steel mould at 650 MPa to form 8 mm diameter cylindrical pins of 50 mm height. Consolidated samples were pressurelessly sintered for 2 hours at 723 K with a heating and a cooling rate of 100 K/min. For the purpose of comparison monolithic aluminium was also prepared by the same process.

2.3. Pin-on-Disc Tests for Sliding Wear. A schematic representation of the sliding wear test machine is presented in Figure 1. The components were designed to get a pin-on-disc

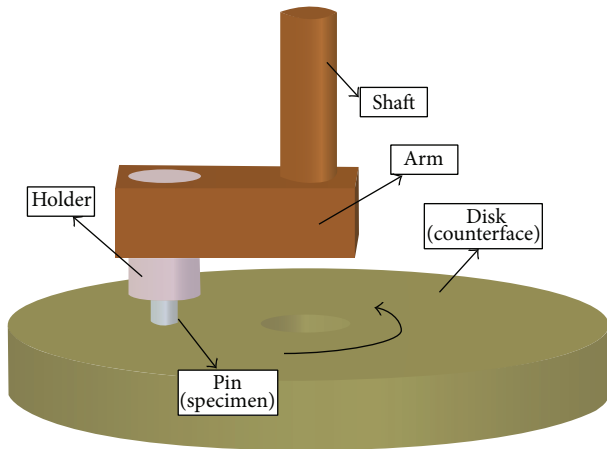


FIGURE 1: Pin-on-disc tribometer [3].

configuration with a holder positioned perpendicularly to the rotating disc. Specimens underwent the sliding wear tests against EN31 steel disc. Loads of 0.1 kg, 0.2 kg, 0.3 kg, 0.4 kg, and 0.5 kg were applied directly to the specimens with the use of the pin as indicated in Figure 1. The flat surface of the pin polished with $9\ \mu\text{m}$ polishing pad. An EN31 steel disc with a hardness of 59 HRC was used as counterface. An average roughness R_a value of $0.3\ \mu\text{m}$ was achieved for the disc through grinding using alumina abrasive wheel. The surfaces of the pin and disc were cleaned with acetone prior to the tests. The tests were carried out under dry sliding conditions at constant sliding speed of 0.5 m/s and normal loads in the range of 0.1 to 0.5 kg. The sliding distance was kept constant at 300 m. Wear rate values were obtained by taking the average from three repeated tests. The friction coefficient was continuously recorded using x - y plotter interfaced to the tribometer. A scanning electron microscope (SEM) was used to inspect the worn surfaces of the specimens.

3. Results and Discussion

3.1. Densification and Micro/Nanostructure. Pressureless sintering takes longer than spark plasma sintering reported previously by Silvestre [2]. There was an oxidised layer on the surface of the samples which is loose and brittle. Nevertheless, the material inside is a dense material. The density of all samples was measured by Archimede's method and all had a relative density between 92.22% and 97.74%.

High resolution SEM image of pure aluminium sintered for 2 h at 723 K showed a uniform and homogenous microstructure of the alloy as shown in a typical SEM micrograph in Figure 2(a). Similarly 0.5 wt%, 1.0 wt%, and 2.0 wt% composites sintered for 2 h at 723 K also exhibit a dense microstructure as shown in Figures 2(b)–2(d). With increasing content of CNTs, the microstructure is less uniform and there are more nanoporous areas observed. It is believed that these are the undispersed CNTs clusters showing the cross section of the hollow nanotubes. This is correlated with the slight reduction in relative density reported above.

TABLE 2: Effect of CNT content on density and hardness properties.

CNT wt.%	Theoretical density (g/cm^3)	Measured density (g/cm^3)	Hardness (HV)	Relative density (%)
0.0	2.70	2.639	19.66	97.74
0.5	2.697	2.584	25.60	95.81
1.0	2.694	2.598	27.45	96.44
1.5	2.691	2.570	30.60	95.50
2.0	2.688	2.479	23.05	92.22

3.2. Hardness. Vickers hardness was measured for pure aluminium and 0.5–2.0 wt% CNT composites as shown in Table 2. Each data point was an average of 3 measurements for the same material.

Figure 3 shows the hardness of the composites and monolithic aluminium processed by the same procedure. The hardness of the nanocomposites increased by about 50% with CNT fraction up to 1.5 wt% and then decreased significantly. The increase in hardness is mainly due to the strengthening effect of CNTs. The decrease in hardness when CNT fraction is over 1.5% is coincident with the significant increase in porosity. Simões et al. [38] also found that the hardness of composite is higher than the monolithic aluminium if the CNTs are well dispersed. The hardness of composite may decrease if the CNTs are damaged during the dispersion process.

3.3. Wear Rate. A widely used equation to compute the wear rate is Archard's equation:

$$V_i = K_i \times F \times S, \quad (1)$$

where F is normal load (kg), S is sliding distance (m), V_i is wear volume (mm^3), and K_i is specific wear rate coefficient (mm^3/kgm). The wear rate for the monolithic Al and the composite containing 0.5 wt%, 1.0 wt%, 1.5 wt%, and 2.0 wt% CNTs versus the applied load is shown in Figure 4. The experiments were carried in triplicate. The wear rate increased monotonically with the applied load. At lower loads of 0.1–0.2 Kg, the composite showed better wear resistance than pure Al. However, at higher loads of 0.3–0.5 Kg, the wear resistance of monolithic Al was better than the composite. The wear rate of the composite increased significantly as the normal load is increased from 0.2 to 0.3 Kg which indicates sharp change in wear mechanism from mild to severe wear regime. These results show that addition of 0.5 wt%, 1.0 wt%, 1.5 wt%, and 2.0 wt% CNTs improves wear resistance of the Al at lower loads (mild conditions) only. At higher loads pores present in the composite and CNTs agglomerates (as shown in Figure 5) act as a source of crack initiation and cause severe subsurface fragmentation resulting in poor wear resistance of the composite compared to the monolithic aluminium. Compared to SPS processed composites reported by Silvestre [2], the sintered composites appear to be more brittle and prone to subsurface fracture. This is owing to the oxidation during the long sintering process. Moreover, weak bonding between CNTs and aluminium particles could be another

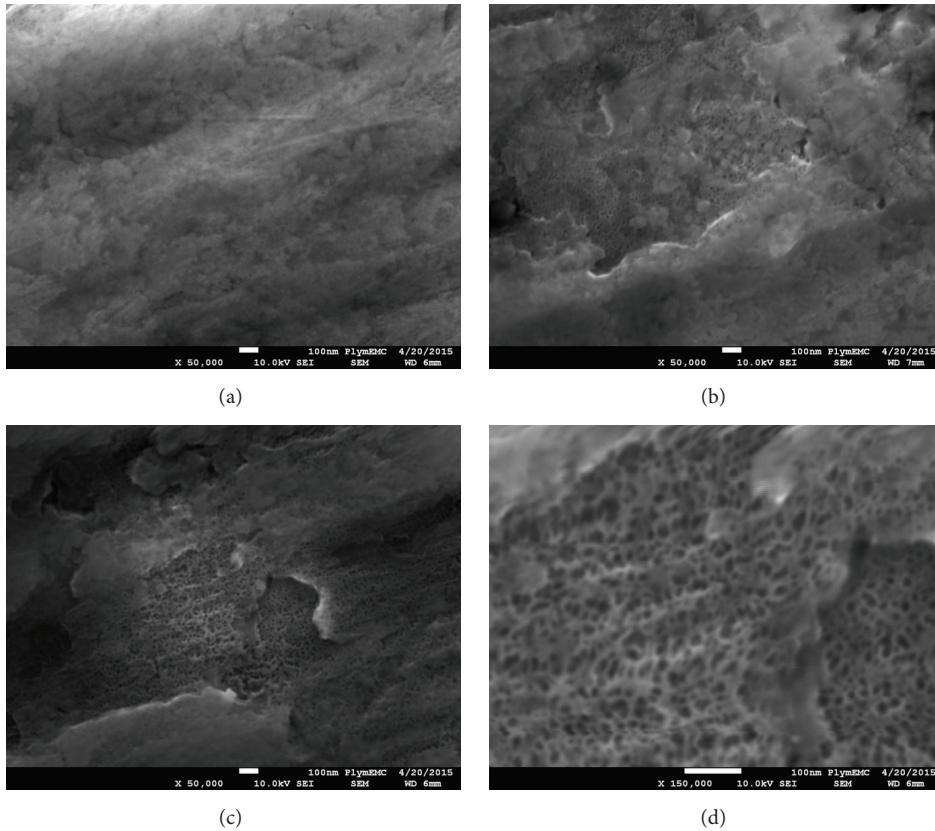


FIGURE 2: SEM micrograph of polished surface of (a) pure Al, (b) Al + 0.5 wt% CNT, (c) Al + 1 wt% CNT, and (d) Al + 2.0 wt% CNT.

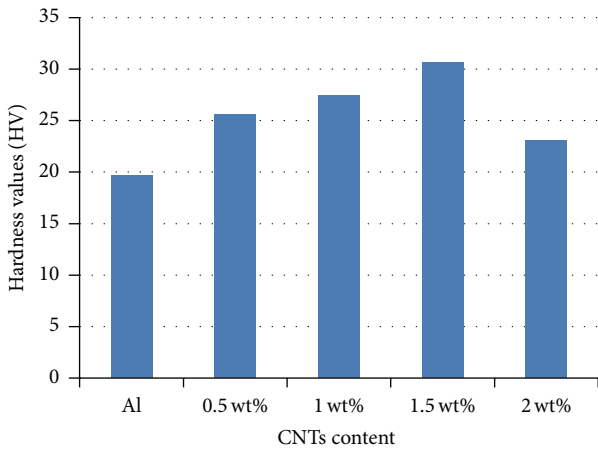


FIGURE 3: Hardness for the Al, 0.5 wt% to 2 wt% CNT.

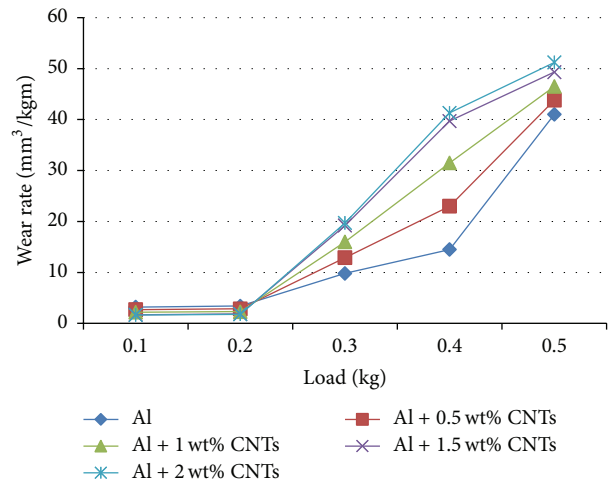


FIGURE 4: Wear rate for the Al and composites with 0.5 wt% to 2 wt% CNT.

possible reason for its severe subsurface fracturing at higher loads.

3.4. Friction Coefficient. The coefficients of friction versus the applied load for the pure aluminium and the 0.5 wt%, 1.0 wt%, 1.5 wt%, and 2.0 wt% composites are presented in Figure 6. At a load of 0.1 Kg, for the first 250 m of sliding distance, the friction coefficient of the monolithic Al increased continuously to about 0.62. Beyond 250 m, it decreased slightly to about 0.6

for the next 100 m. While for the 0.5 wt% CNT composite, the friction coefficient showed considerable increase in the first 150 m of sliding. It then stayed in the range of 0.4–0.45. It is evident that the friction coefficient of composite is not only lower but also less fluctuating compared to the monolithic alloy. Similarly for the 1 wt%, 1.5 wt%, and 2.0 wt% CNT composite, the friction coefficient increased in the first

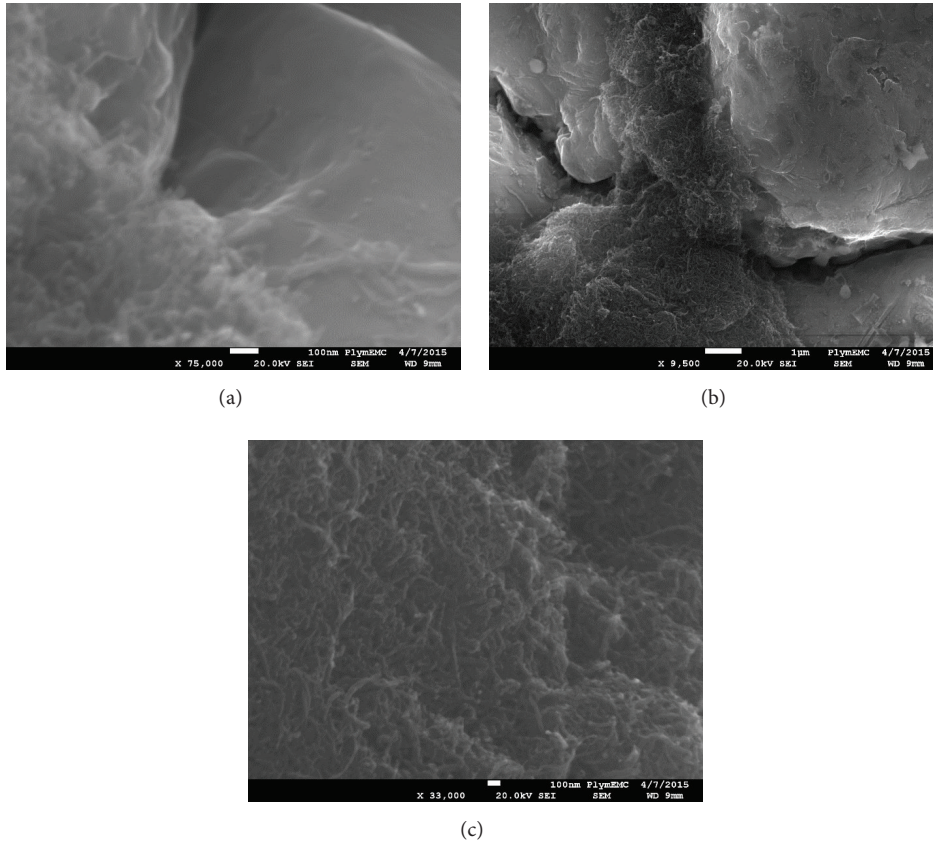


FIGURE 5: SEM micrograph of fractal surface of (a) Al + 1 wt% CNT, (b) Al + 1.5 wt% CNT, and (c) Al + 2 wt% CNT.

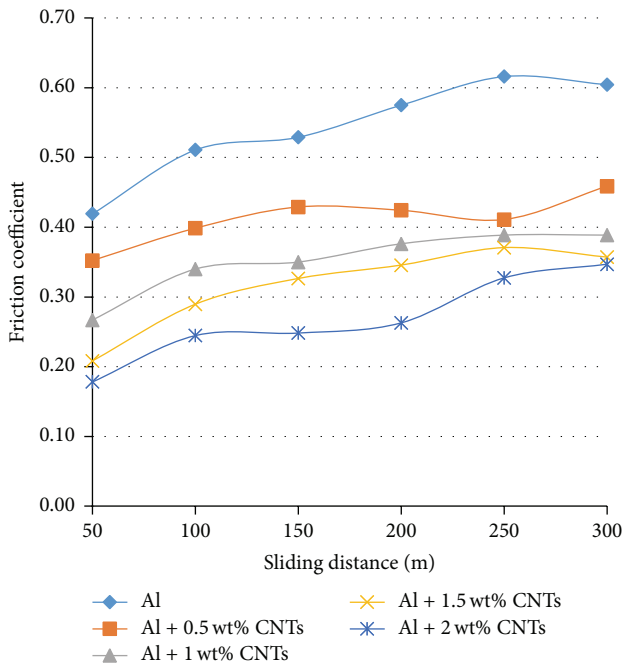


FIGURE 6: Friction coefficient for Al and 0.5 wt% to 2 wt% CNT at 0.1 kg.

200 m of sliding. Then it remained steady at an average value of 0.4, 0.35, and 0.3, respectively, for the remaining 100 m. This reduction in friction may be attributed to the lubricating effect of CNTs.

The coefficient of friction versus load for the monolithic alloy and the 0.5 wt% to 2.0 wt% composites are presented in Figure 7 for a load of 0.2 Kg. It can be seen that the friction coefficient of both monolithic aluminium and composites decreased considerably compared to that obtained at a load of 0.1 Kg. For the monolithic alloy and the composites with CNTs up to 1 wt%, the friction coefficient increased by about 20% in the first 150 m and then stabilises. For composites with CNTs 1.5 wt%, the friction coefficient stayed at about 0.18 to 0.2. For CNTs above 2 wt%, the friction coefficient dropped by 20% to about 0.15 after 100 m.

The coefficients of friction versus normal load for the pure aluminium and the 0.5 wt% to 2.0 wt% composites are presented in Figure 8 at a load of 0.2 kg. It can be seen that the trend of friction is very similar to that seen at 0.2 kg except the 2.0 wt% composite. The monolithic aluminium and composite materials with CNTs up to 1.5 wt% displayed slight increase in friction coefficient with sliding distance up to 150 m and then levels off. The composite with 2.0 wt% CNTs increased steadily from 0.15 to 0.22.

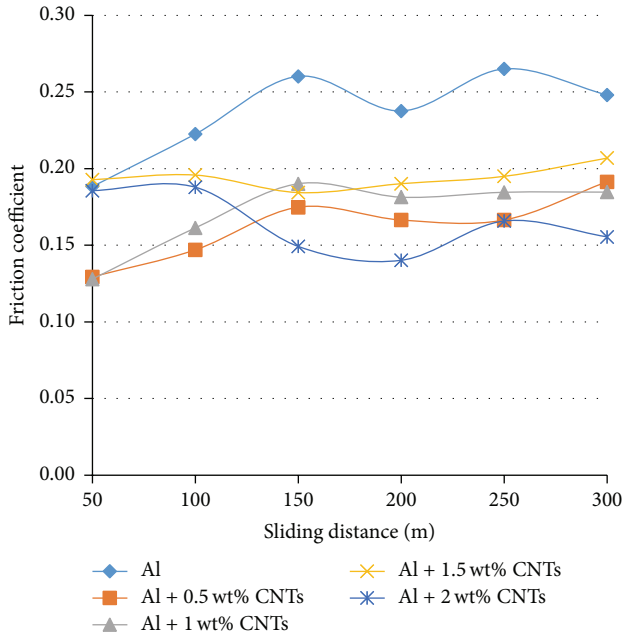


FIGURE 7: Friction coefficient for Al and 0.5 wt% to 2 wt% CNT at 0.2 kg.

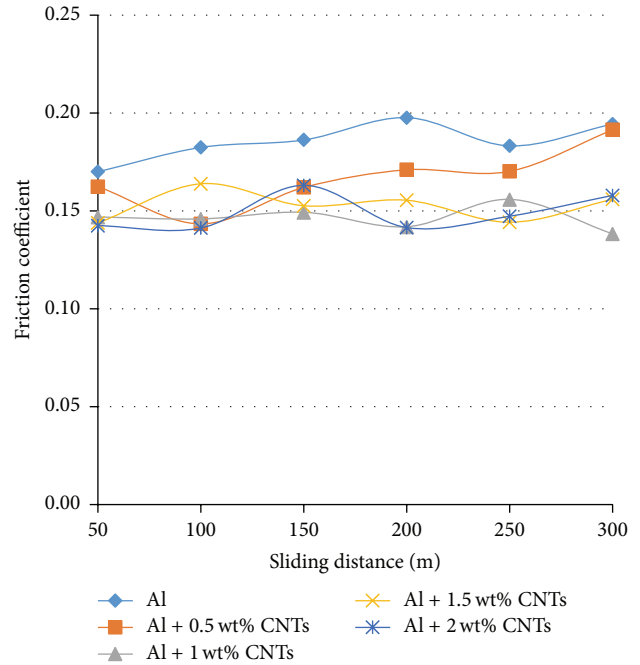


FIGURE 9: Friction coefficient for Al and 0.5 wt% to 2.0 wt% CNT at 0.4 kg.

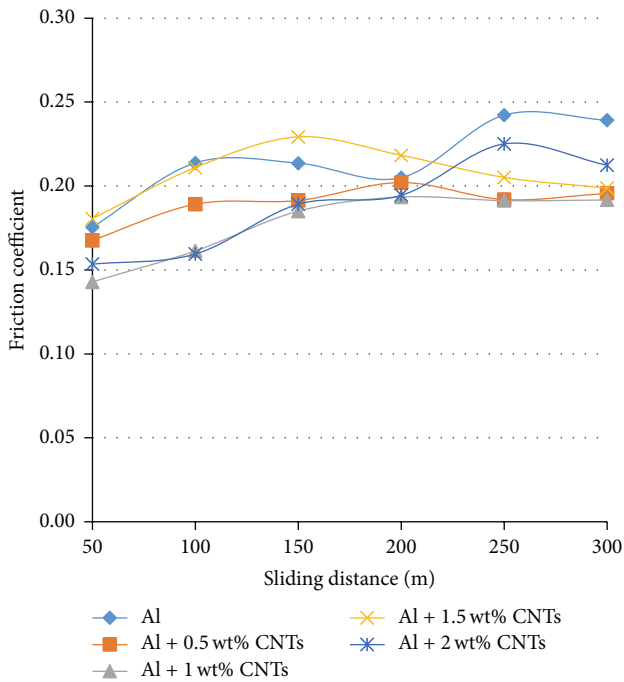


FIGURE 8: Friction coefficient for Al and 0.5 wt% to 2.0 wt% CNT at 0.3 kg.

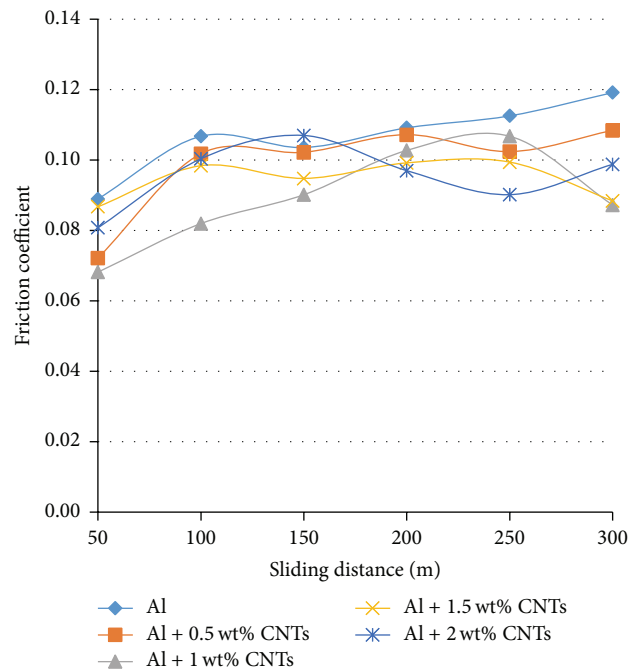


FIGURE 10: Friction coefficient for Al and 0.5 wt% to 2.0 wt% CNT at 0.5 kg.

The coefficients of friction for the applied load of 0.4 kg are presented in Figure 9. It can be seen that the variation of friction coefficient with sliding distance is smaller than that at lower applied load presented above. The friction coefficients of the monolithic alloy and the 0.5 wt%, 1.0 wt%, 1.5 wt%, and 2.0 wt% CNT composites remained almost

constant at average values of 0.185, 0.175, 0.152, 0.155, and 0.16, respectively.

The coefficients of friction for a load of 0.5 kg are presented in Figure 10. It can be seen that both aluminium and composite materials exhibited considerable variation in friction coefficient for the first 100 m of sliding, but for

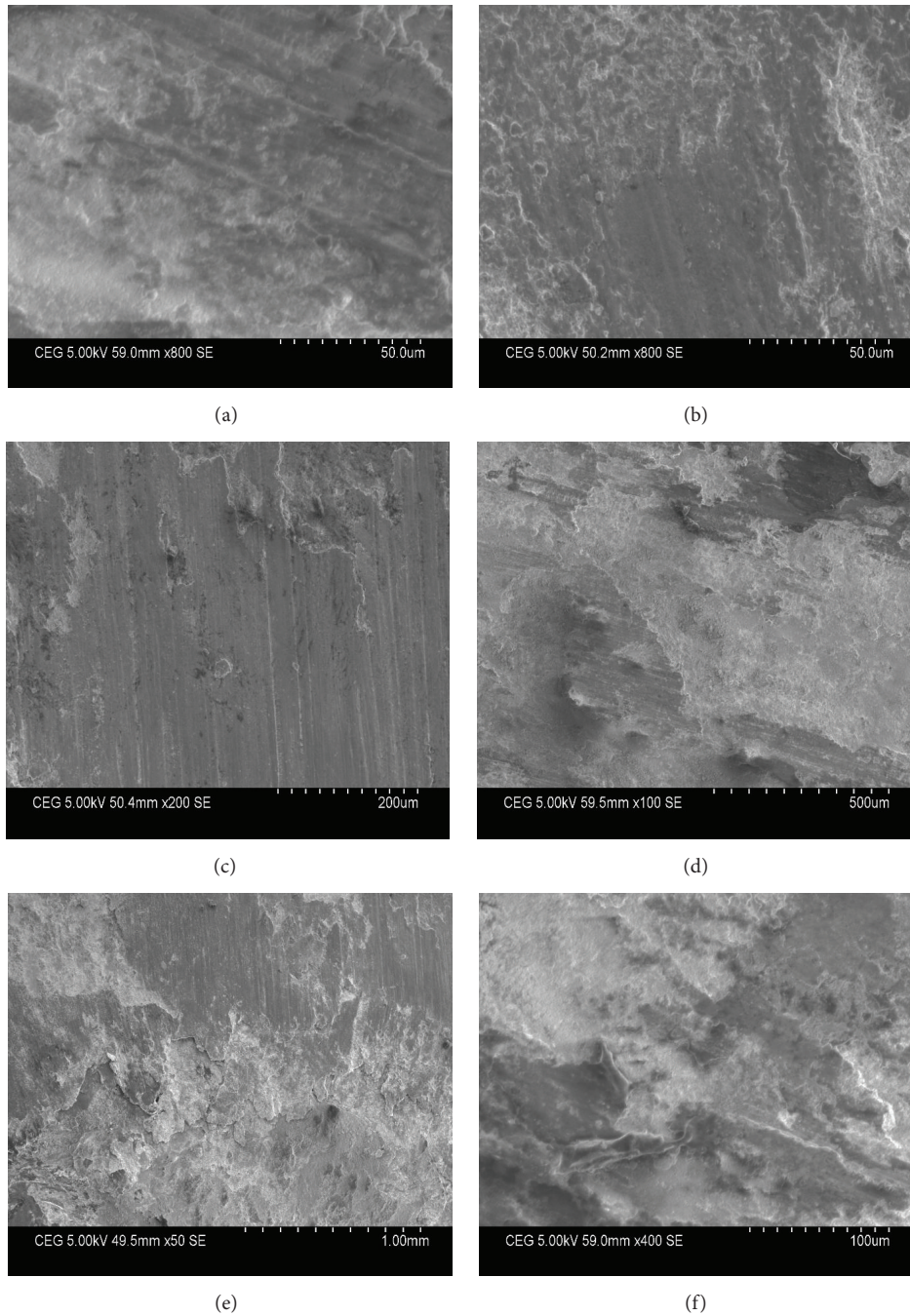


FIGURE 11: SEM micrographs of (a) Al at 0.1 kg, (b) Al + 1 wt% at 0.1 kg, (c) Al at 0.2 kg, (d) Al + 1 wt% at 0.2 kg, (e) Al at 0.3 kg, and (f) Al + 1 wt% at 0.3 kg.

the remaining sliding distance, the friction coefficient of the monolithic alloy and the 0.5 wt%, 1.0 wt%, 1.5 wt%, and 2.0 wt% CNT composites remained almost constant at average values of 0.11, 0.105, 0.10, 0.098, and 0.095, respectively.

3.5. Friction and Wear Mechanisms. SEM micrographs of worn surfaces after tests at different loads are presented in Figure 11. It can be seen that, at a load of 0.1 kg, abrasion is dominant for the monolithic alloy and CNT composite

leaving small wear marks as shown in Figures 11(a) and 11(b), respectively. Minor delamination can be found in monolithic alloy (cf. Figure 11(a)) whereas the composite did not show any delamination (cf. Figure 11(b)). This is due to greater hardness and strength imparted in the composite by the addition of CNTs. At a load of 0.2 kg, considerable abrasion along with mild delamination can be seen for monolithic alloy in Figure 11(c). Significant delaminated flakes with crack initiation can be seen at several locations for the composite in Figure 11(d). Increasing the applied load to

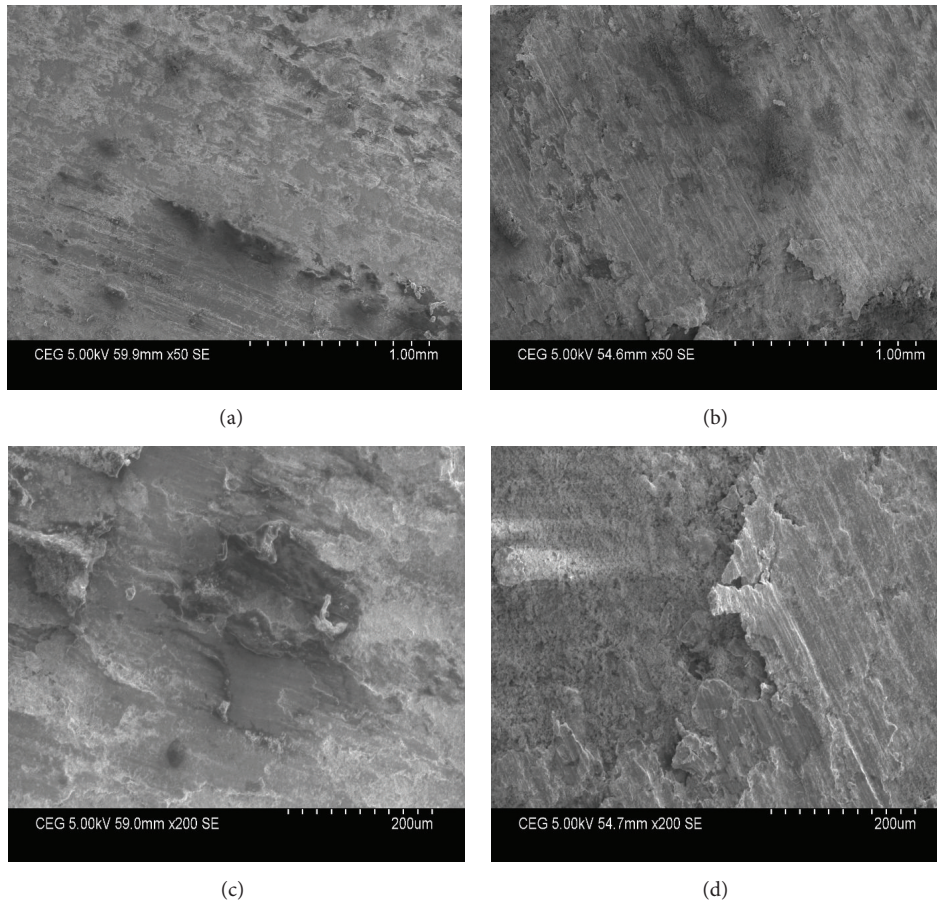


FIGURE 12: SEM micrograph at 0.5 kg of (a) and (c) Al and (b) and (d) Al + 1 wt%.

0.3 kg, the monolithic alloy displayed severe delamination with some possible breakage of adhesive junction as shown in Figure 11(e), while the composite showed severe subsurface fracturing and deep pits in Figure 11(f). It shows that cracks have initiated and propagated as a result of surface fatigue at higher loads during sliding leading to heavy delamination and hence high wear rate of the composite. The weak bonding between CNTs and Al particles in sintered samples could be another reason for crack initiation and propagation at higher loads.

Figures 12(a) and 12(b) show lower magnification SEM micrographs of worn surfaces at an applied load of 0.5 kg for the alloy and composite, respectively. The surface of the alloy is characterized by the formation of long and deep grooves. Such grooves could have been formed due to continuous abrasion of the specimen by the counterface. However, the surface of the composite is characterized by severe fracture and delamination, especially at the edges of the cylinder. This breaking of sharp edge during wear test at high loads may be attributed to weak bonding between CNTs and Al particles in the composite. Higher magnification SEM micrographs of worn surfaces clearly revealed the severe fracture and deep groove in the monolithic alloy and composite as can be seen in Figures 12(c) and 12(d), respectively. The deep grooves in the monolithic alloy (cf. Figure 12(c)) are typical of galling

and material transfer caused by the roughened counterface as found by Casati and Vedani [3]. The roughness of the grooves in the composite (cf. Figure 12(d)) indicates the breakage of material due to the subsurface fracture. The results infer that the higher wear rate of composites under an applied load larger than 0.2 kg is correlated with the subsurface fracturing due to the increase in hardness and the reduction in fracture toughness.

4. Conclusions

The specimens were successfully sintered at suitable temperatures in ambient air and relevant tests also had been done for evaluating density, hardness, and tribological behaviour of carbon nanotubes reinforced aluminium metal matrix composites. Compared to other processing methods, this process has the potential to make large parts and does not require expensive equipment. The density of all samples was measured by Archimedes method and all had a theoretical density between 92.22% and 97.74%. The microhardness was measured for aluminium and 0.5–2 wt% CNT composites. The hardness increased with increasing fraction up to 1.5 wt% and then reduced at 2 wt%. Wear and friction tests were conducted using “pin-on-disc” wear test apparatus. The micro/nanostructure was examined using high resolution

field emission SEM to examine the distribution of CNTs in the matrix before and after pin-on-disc wear test. The SEM results were found to be correlated with wear rates. Wear rates and friction coefficient results were briefly discussed. The results showed that, under mild wear conditions, the CNTs reinforced Al composite displayed lower wear rate and friction coefficient compared to the monolithic Al alloy. However, for severe wear conditions, the composite displayed higher wear rate and friction coefficient compared to the monolithic alloy. Analysis of worn surfaces revealed that, at lower loads, abrasion was the dominant wear mechanism for both monolithic aluminium and composites. At higher loads, adhesion was found to be dominant for the monolithic alloy while subsurface fracturing and delamination were observed for the composite. Also, it was clarified that the friction and wear behaviour of Al composites is largely dependent on the applied load and there appears a critical load beyond which CNTs could have a negative impact on the wear resistance of the aluminium alloy.

It is envisaged that the densification and tribological properties of CNTs reinforced composites could be further improved by optimising the chemical pretreatment and dispersion of CNTs and to minimise the oxidation of the powders by carrying out the milling experiments to be carried out at room temperature under argon atmosphere. The densification can also be improved by secondary consolidation such as forging and rolling after cold compaction and sintering.

Conflict of Interests

The authors declare that there is no conflict of interests regarding the publication of this paper.

Acknowledgments

The authors wish to acknowledge the financial support from UGC (India) and British Council (UK) through UKIERI-UGC Thematic Partnership (UKIERI-UGC-2012/13-032). Authors would like to thank the technicians of both Plymouth University and Anna University for their great support to conduct this research work.

References

- [1] S. R. Bakshi, D. Lahiri, and A. Agarwal, "Carbon nanotube reinforced metal matrix composites—a review," *International Materials Reviews*, vol. 55, no. 1, pp. 41–64, 2010.
- [2] N. Silvestre, "State-of-the-art review on carbon nanotube reinforced metal matrix composites," *International Journal of Composite Materials*, vol. 3, no. 6, pp. 28–44, 2013.
- [3] R. Casati and M. Vedani, "Metal matrix composites reinforced by nano-particles—a review," *Metals*, vol. 4, no. 1, pp. 65–83, 2014.
- [4] A. M. Al-Qutub, A. Khalil, N. Saheb, and A. S. Hakeem, "Wear and friction behavior of Al6061 alloy reinforced with carbon nanotubes," *Wear*, vol. 297, no. 1-2, pp. 752–761, 2013.
- [5] C. R. Bradbury, J.-K. Gomon, L. Kollo, H. Kwon, and M. Leparoux, "Hardness of multi wall carbon nanotubes reinforced aluminium matrix composites," *Journal of Alloys and Compounds*, vol. 585, pp. 362–367, 2014.
- [6] H. R. Le, M. P. F. Sutcliffe, and J. A. Williams, "Friction and material transfer in micro-scale sliding contact between aluminium alloy and steel," *Tribology Letters*, vol. 18, no. 1, pp. 99–104, 2005.
- [7] I.-Y. Kim, J.-H. Lee, G.-S. Lee, S.-H. Baik, Y.-J. Kim, and Y.-Z. Lee, "Friction and wear characteristics of the carbon nanotube–aluminum composites with different manufacturing conditions," *Wear*, vol. 267, no. 1–4, pp. 593–598, 2009.
- [8] S. Iijima, "Helical microtubules of graphitic carbon," *Nature*, vol. 354, no. 6348, pp. 56–58, 1991.
- [9] Y. H. Lee, "The physical property and application of carbon nanotube," *Sae Mulli*, vol. 51, pp. 84–114, 2005.
- [10] D. S. So, I. H. Lee, G. J. Bae, and W. J. Bak, "R&D and market trend of carbon nanotube devices," *Prospects of Industrial Chemistry*, vol. 10, pp. 58–66, 2007.
- [11] C. Qin, X. Shi, S. Q. Bai, L. D. Chen, and L. J. Wang, "High temperature electrical and thermal properties of the bulk carbon nanotube prepared by SPS," *Materials Science and Engineering A*, vol. 420, no. 1-2, pp. 208–211, 2006.
- [12] T. Laha, A. Agarwal, T. McKechnie, and S. Seal, "Synthesis and characterization of plasma spray formed carbon nanotube reinforced aluminum composite," *Materials Science & Engineering A*, vol. 381, no. 1-2, pp. 249–258, 2004.
- [13] S. R. Bakshi, V. Singh, S. Seal, and A. Agarwal, "Aluminum composite reinforced with multiwalled carbon nanotubes from plasma spraying of spray dried powders," *Surface and Coatings Technology*, vol. 203, no. 10-11, pp. 1544–1554, 2009.
- [14] T. Kuzumaki, K. Miyazawa, H. Ichinose, and K. Ito, "Processing of carbon nanotube reinforced aluminum composite," *Journal of Materials Research*, vol. 13, no. 9, pp. 2445–2449, 1998.
- [15] R. George, K. T. Kashyap, R. Rahul, and S. Yamdagni, "Strengthening in carbon nanotube/aluminium (CNT/Al) composites," *Scripta Materialia*, vol. 53, no. 10, pp. 1159–1163, 2005.
- [16] R. P. Bustamante, I. Estrada Guel, W. A. Flores, M. Yoshida, and P. J. Ferreira, "Novel Al-matrix nanocomposites reinforced with multi-walled carbon nanotubes," *Journal of Alloys and Compounds*, vol. 450, no. 1-2, pp. 323–326, 2008.
- [17] A. M. K. Esawi, K. Morsi, A. Sayed, A. A. Gawad, and P. Borah, "Fabrication and properties of dispersed carbon nanotube-aluminum composites," *Materials Science & Engineering A*, vol. 508, no. 1-2, pp. 167–173, 2009.
- [18] L. Wang, H. Choi, J.-M. Myoung, and W. Lee, "Mechanical alloying of multi-walled carbon nanotubes and aluminium powders for the preparation of carbon/metal composites," *Carbon*, vol. 47, no. 15, pp. 3427–3433, 2009.
- [19] D. Poirier, R. Gauvin, and R. A. L. Drew, "Structural characterization of mechanically milled carbon nanotube/aluminum mixture," *Composites Part A: Applied Science and Manufacturing*, vol. 40, pp. 1482–1489, 2009.
- [20] R. P. Bustamante, G. D. Esparza, I. Guel, and M. Yoshida, "Microstructural and mechanical characterization of Al-MWCNT composites produced by mechanical alloying," *Materials Science & Engineering A*, vol. 502, pp. 159–163, 2009.
- [21] A. M. K. Esawi, K. Morsi, A. Sayed, M. Taher, and S. Lanka, "The influence of carbon nanotube (CNT) morphology and diameter on the processing and properties of CNT-reinforced aluminium composites," *Composites Part A: Applied Science and Manufacturing*, vol. 42, no. 3, pp. 234–243, 2011.

- [22] J. Stein, B. Lenczowski, N. Fréty, and E. Anglaret, "Mechanical reinforcement of a high-performance aluminium alloy AA5083 with homogeneously dispersed multi-walled carbon nanotubes," *Carbon*, vol. 50, no. 6, pp. 2264–2272, 2012.
- [23] Y. Wu, G.-Y. Kim, and A. M. Russell, "Effects of mechanical alloying on an Al6061-CNT composite fabricated by semi-solid powder processing," *Materials Science and Engineering A*, vol. 538, pp. 164–172, 2012.
- [24] Y. Wu and G.-Y. Kim, "Carbon nanotube reinforced aluminum composite fabricated by semi-solid powder processing," *Journal of Materials Processing Technology*, vol. 211, no. 8, pp. 1341–1347, 2011.
- [25] J. Wu, H. Zhang, Y. Zhang, and X. Wang, "Mechanical and thermal properties of carbon nanotube/aluminum composites consolidated by spark plasma sintering," *Materials and Design*, vol. 41, pp. 344–348, 2012.
- [26] J.-Z. Liao, M.-J. Tan, and I. Sridhar, "Spark plasma sintered multi-wall carbon nanotube reinforced aluminum matrix composites," *Materials and Design*, vol. 31, no. 1, pp. S96–S100, 2010.
- [27] Z. Y. Liu, B. L. Xiao, W. G. Wang, and Z. Y. Ma, "Singly dispersed carbon nanotube/aluminum composites fabricated by powder metallurgy combined with friction stir processing," *Carbon*, vol. 50, no. 5, pp. 1843–1852, 2012.
- [28] H. Izadi and A. P. Gerlich, "Distribution and stability of carbon nanotubes during multi-pass friction stir processing of carbon nanotube/aluminum composites," *Carbon*, vol. 50, no. 12, pp. 4744–4749, 2012.
- [29] L. Jiang, Z. Li, G. Fan, L. Cao, and D. Zhang, "The use of flake powder metallurgy to produce carbon nanotube (CNT)/aluminum composites with a homogenous CNT distribution," *Carbon*, vol. 50, no. 5, pp. 1993–1998, 2012.
- [30] H. Kwon, D. H. Park, J. F. Silvain, and A. Kawasaki, "Investigation on carbon nanotube reinforced aluminum matrix composite materials," *Composites Science and Technology*, vol. 70, no. 3, pp. 546–550, 2010.
- [31] T. Noguchi, A. Magario, S. Fukazawa, S. Shimizu, J. Beppu, and M. Seki, "Carbon nanotube/aluminium composites with uniform dispersion," *Materials Transactions*, vol. 45, no. 2, pp. 602–604, 2004.
- [32] H. J. Choi, S. M. Lee, and D. H. Bae, "Wear characteristic of aluminum-based composites containing multi-walled carbon nanotubes," *Wear*, vol. 270, no. 1-2, pp. 12–18, 2010.
- [33] S.-M. Zhou, X.-B. Zhang, Z.-P. Ding, C.-Y. Min, G.-L. Xu, and W.-M. Zhu, "Fabrication and tribological properties of carbon nanotubes reinforced Al composites prepared by pressureless infiltration technique," *Composites Part A: Applied Science and Manufacturing*, vol. 38, no. 2, pp. 301–306, 2007.
- [34] M. Zhu, Y. Gao, C. Y. Chung et al., "Improvement of the wear behaviour of Al–Pb alloys by mechanical alloying," *Wear*, vol. 242, no. 1-2, pp. 47–53, 2000.
- [35] C. Suryanarayana, "Synthesis of nanocomposites by mechanical alloying," *Journal of Alloys and Compounds*, vol. 509, no. 1, pp. S229–S234, 2011.
- [36] S. C. Tjong, *Carbon Nanotube Reinforced Composites. Metal and Ceramic Composites*, Wiley-VCH, New York, NY, USA, 2009.
- [37] S. R. Bakshi, V. Singh, K. Balani, D. G. McCartney, S. Seal, and A. Agarwal, "Carbon nanotube reinforced aluminum composite coating via cold spraying," *Surface & Coatings Technology*, vol. 202, no. 21, pp. 5162–5169, 2008.
- [38] S. Simões, F. Viana, M. A. Reis, and M. F. Vieira, "Influence of dispersion/mixture time on mechanical properties of Al–CNTs nanocomposites," *Composite Structures*, vol. 126, pp. 114–122, 2015.

Research Article

Paraffin Nanocomposites for Heat Management of Lithium-Ion Batteries: A Computational Investigation

A. H. N. Shirazi,^{1,2} Farzad Mohebbi,² M. R. Azadi Kakavand,² B. He,² and T. Rabczuk^{1,2}

¹*Institute of Research & Development, Duy Tan University, Quang Trung, Da Nang, Vietnam*

²*Institute of Structural Mechanics, Bauhaus-Universität Weimar, Weimar, Germany*

Correspondence should be addressed to A. H. N. Shirazi; ali.hn.s@outlook.com and T. Rabczuk; timon.rabczuk@uni-weimar.de

Received 25 September 2015; Accepted 2 February 2016

Academic Editor: Zafar Iqbal

Copyright © 2016 A. H. N. Shirazi et al. This is an open access article distributed under the Creative Commons Attribution License, which permits unrestricted use, distribution, and reproduction in any medium, provided the original work is properly cited.

Lithium-ion (Li-ion) batteries are currently considered as vital components for advances in mobile technologies such as those in communications and transport. Nonetheless, Li-ion batteries suffer from temperature rises which sometimes lead to operational damages or may even cause fire. An appropriate solution to control the temperature changes during the operation of Li-ion batteries is to embed batteries inside a paraffin matrix to absorb and dissipate heat. In the present work, we aimed to investigate the possibility of making paraffin nanocomposites for better heat management of a Li-ion battery pack. To fulfill this aim, heat generation during a battery charging/discharging cycles was simulated using Newman's well established electrochemical pseudo-2D model. We couple this model to a 3D heat transfer model to predict the temperature evolution during the battery operation. In the later model, we considered different paraffin nanocomposites structures made by the addition of graphene, carbon nanotubes, and fullerene by assuming the same thermal conductivity for all fillers. This way, our results mainly correlate with the geometry of the fillers. Our results assess the degree of enhancement in heat dissipation of Li-ion batteries through the use of paraffin nanocomposites. Our results may be used as a guide for experimental set-ups to improve the heat management of Li-ion batteries.

1. Introduction

In recent years, communication technologies have been rapidly progressed. Therefore, increasing the efficiency is inevitable in applications ranging from portable electronics to renewable energies and power plant is inevitable. In portable electronics, the battery plays a crucial role in their efficiency. On the other hand, there are some deficiencies in the application of the present batteries in which the thermal management of battery packs is one of the most important problems. In some cases, uncontrollable temperature inside the batteries may result in fire or even explosion. Recently, Goli and coworkers [1] proposed the utilization of paraffin phase change material (PCM) with graphene fillers to enhance the performance of lithium-ion (Li-ion) batteries versus intense self-heating. The above-mentioned methodology describes a heat storage-heat conduction approach that has affirmative effects on thermal management of any types of batteries including Li-ion batteries. Kumaresan

et al. [2] assessed discharge efficiency prediction of Lithium-ion cell at various operating temperatures (15–45°C) by a thermal model. Numerical results were compared with experimental data obtained from lithium-ion pouch cells. In addition, Goyal and Balandin [3] investigated the thermal properties of some materials with the hybrid graphene-metal particle fillers. In this research activity, the thermal conductivity of composites was measured with the variation of temperature. The achieved results are applicable for the thermal management of electronics and optoelectronics. Zolot et al. [4] presented the hybrid vehicle test focusing on battery thermal management. The results of tests proved that the performance of battery packs significantly changes due to thermal condition. Yeow et al. [5] developed 3D finite element (FE) models with consideration of geometry variations in order to model the treatment of Lithium ion cells of vehicle electrification applications. The results show that the 3D electrothermal model satisfactorily describes the electrothermal behaviour of the Li-ion battery cells and

the results are in acceptable agreement with battery temperature measurements. To simulate various cell types for an electric drive system, Bengner et al. [6] developed a parameterized model for the electrochemical and thermal properties. The comparison between modelling results and the measurement indicates that the developed model can predict the current voltage behaviour and the temperature development of the various cells. Mohammadian et al. [7] made a comparison between internal and external cooling procedures for thermal management of LIBs. They performed 2D and 3D transient thermal analysis of a prismatic Li-ion battery cell. The results showed that, with the same pumping power, external cooling decreases the bulk temperature less than internal cooling and, moreover, internal cooling considerably decreases the standard deviation of the temperature inside the battery.

It is quite well-known that the phase change materials can store a large amount of heat according to their high capacity of latent heat storage. They can absorb high amount of heat while their temperature remains nearly constant. According to their applications, there are various types of PCMs that each of them is applicable for certain temperature ranges [8]. However, the properties of PCMs yet can be varied by changing their chemical composition or by adding additional components. In this regard, one solution is to fabricate nanocomposites structures through adding nanoscale fillers to PCMs. For the application in Li-ion batteries, the thermal conductivity is the main parameter to improve. Carbon based nanostructures such as graphene and carbon nanotubes offer the highest thermal conductivities available in the nature [9]. Therefore, they could be considered as the best candidates to enhance heat conduction for PCMs. Shahil and Balandin [10] showed that adding multilayer graphene to commercial grease can enhance drastically the thermal conductivity of the mixture even in low fillers volume percent. There exist numerous theoretical and experimental studies available in the direction of composite materials with superior thermal and mechanical properties [11–17].

In this paper, we investigate the temperature rise in a Lithium ion battery pack. In this regard, the simulations are used to provide a general viewpoint to guide experiments which are expensive and time consuming as well [18, 19]. We used pure and nanocomposites paraffin PCMs to dissipate the heat produced during the charge/discharge cycles of a battery pack containing 16 individual Li-ion batteries. Fullerene, graphene, and CNT were used as fillers with different volumes concentration to enhance the thermal conductivity of paraffin hybrid phase change material. The effects of various volume percent of fillers on thermal behaviour of batteries were investigated at different charging/discharging rates (C-rates). Our results show remarkable effect of using paraffin PCMs on the heat dissipation of a battery pack. Thermal conductivity coefficients of hybrid paraffin PCMs were obtained through finite element modelling of representative volume elements. Heat generation rates during the charging/discharging cycles were simulated using Newman's well established electrochemical pseudo-2D model [20]. It is shown that as the filler's volume fraction inside the paraffin increases, the amount of heat dissipation to the ambient environment increases, which is due to the increase in the thermal conductivity of PCMs.

2. Theory and Modeling

Numerical simulations of electrochemical response of Li-ion battery at different charging/discharging cycles were simulated within the framework of the pseudo-2D electrochemical model proposed by Newman and Thomas-Alyea [20]. In this model, the dynamic performance of a cell is characterized by the solution of four partial differential equations describing the time evolution of the lithium concentration profile in the electrode and electrolyte phases, under charge conservation. Then, based on the electrochemical response, heat generation was calculated which was used in the heat transfer model for the evaluation of temperature rises in a battery pack. Accordingly, we first present the electrochemical model which is considered as a 1D problem. Then, we discuss the heat sources and temperature evolution in the battery cell. We note that the heat sources are calculated based on the 1D electrochemical problem, which is then coupled with 3D heat transfer modelling. Figure 1 illustrates the 1D Li-ion cell model which consists of three main regions: the mesocarbon microbead (MCMB) negative composite electrode (graphite type structure), an electron-blocking separator, and LiCoO₂ positive composite electrode.

Lithium concentration in the electrolyte phase is obtained by using Fick's second law along the x -coordinate with a source term coupled to the local reaction current density which yields the following equation:

$$\frac{\partial (\epsilon_e C_e)}{\partial t} = \frac{\partial}{\partial x} \left(D_e^{\text{eff}} \frac{\partial C_e}{\partial x} \right) + \frac{1 - t_+^0}{F} j^{\text{Li}}, \quad (1)$$

where ϵ_e is the volume fraction of electrolyte, C_e is the concentration of Li in electrolyte, D_e^{eff} is the effective diffusion coefficient of Li in the electrolyte, t_+^0 is the transference number of Li-ions with respect to the velocity of solvent, and F is the Faraday constant. j^{Li} is the reaction current density.

The Li-ions cannot diffuse through the current collectors, as set by the boundary conditions in (2), which is valid at the two electrode/current collector interfaces

$$\frac{\partial C_e}{\partial x} \Big|_{x=0} = \frac{\partial C_e}{\partial x} \Big|_{x=L} = 0. \quad (2)$$

At the interfaces between the positive electrode/separator and separator/negative electrode, the concentration of the binary electrolyte (C_e) and its flux ($\partial C_e / \partial x$) are continuous.

For the modelling of diffusion of Li-ions inside the solid particles, Newman's model assumes the electrode can be described by a lattice of spherical particles of identical size representing the intercalation centre into which metallic lithium diffuses. The distribution of lithium in the solid phase (C_s) is described by Fick's second law of diffusion in polar coordinates (r), as shown in the following relation:

$$\frac{\partial C_s}{\partial t} = \frac{D_s}{r^2} \frac{\partial}{\partial r} \left(r^2 \frac{\partial C_s}{\partial r} \right), \quad (3)$$

where D_s is the diffusion coefficient in solid particles. The solution is constrained by a zero gradient boundary condition at the centre of the particle from symmetry arguments,

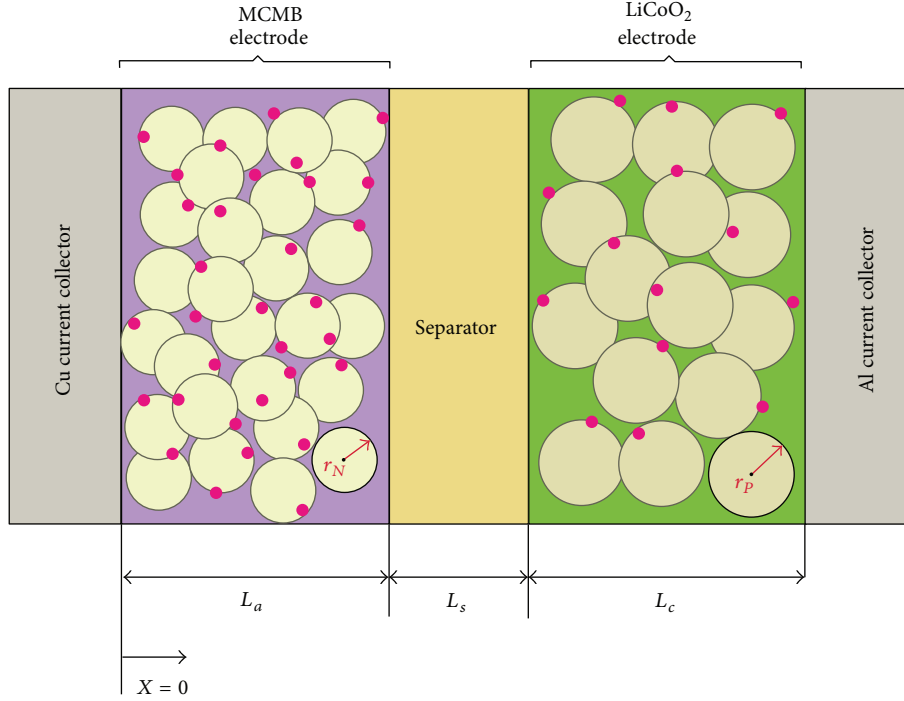


FIGURE 1: Schematic illustration of Newman's electrochemical model based on 1D (x -direction) electrochemical cell model coupled with 1D microscopic (r -direction) solid diffusion model.

while at the surface of the particle the lithium flux must correspond to the reaction current density j^{Li} , as imposed by the following equation:

$$\begin{aligned} \left. \frac{\partial C_s}{\partial r} \right|_{r=0} &= 0, \\ -D_s \left. \frac{\partial C_s}{\partial r} \right|_{r=R_s} &= \frac{j^{\text{Li}}}{a_s F}, \end{aligned} \quad (4)$$

where r is the particle radius of negative or positive electrodes. Potential in the electrolyte phase ϕ_e is a function of reaction current density j^{Li} and the local concentration of Li (C_e) by the following relation:

$$\frac{\partial}{\partial x} \left(k^{\text{eff}} \frac{\partial \phi_e}{\partial x} \right) + \frac{\partial}{\partial x} \left(k_D^{\text{eff}} \frac{\partial}{\partial x} \ln C_e \right) + j^{\text{Li}} = 0, \quad (5)$$

where k^{eff} is the effective ionic conductivity of electrolyte and k_D^{eff} is the effective diffusional conductivity of a specie. The solution of (5) is subject to a zero gradient boundary condition at the two current collector/electrode interfaces

$$\left. \frac{\partial \phi_e}{\partial x} \right|_{x=0} = \left. \frac{\partial \phi_e}{\partial x} \right|_{x=L} = 0. \quad (6)$$

Finally, the potential in the solid phase ϕ_s is introduced as a function of the conductivity of the electrode σ^{eff} and the reaction current density j^{Li} , as described by the following relation:

$$\frac{\partial}{\partial x} \left(\sigma^{\text{eff}} \frac{\partial \phi_s}{\partial x} \right) = j^{\text{Li}}. \quad (7)$$

The boundary conditions are then introduced as follows: at the electrode/separators interface, there is no flux of charge, and thus a zero gradient boundary condition is applied. Moreover, at the electrode/current collector interface, the charge flux corresponds to the current in the outside circuit

$$\begin{aligned} -\sigma_-^{\text{eff}} \left. \frac{\partial \phi_s}{\partial x} \right|_{x=0} &= \sigma_+^{\text{eff}} \left. \frac{\partial \phi_s}{\partial x} \right|_{x=L} = \frac{I}{A}, \\ \left. \frac{\partial \phi_s}{\partial x} \right|_{x=\delta-} &= \left. \frac{\partial \phi_s}{\partial x} \right|_{x=L-\delta+} = 0. \end{aligned} \quad (8)$$

Last, but not the least, j^{Li} which is a parameter that simulate charge transfer rate in all previous four PDEs is determined by the Butler-Volmer equation as follows:

$$j^{\text{Li}} = a_s i_0 \left\{ \exp \left[\frac{0.5F}{RT} \eta \right] - \exp \left[-\frac{0.5F}{RT} \eta \right] \right\}, \quad (9)$$

where a_s is the active surface area per electrode unit volume (m^2/m^{-3}), F is the Faraday constant, T is temperature, R is the universal gas constant, and finally i_0 is exchange current density which is introduced as follows:

$$i_0 = K_i (C_e)^{0.5} (C_{s,\text{max}} - C_{s,\text{surf}})^{0.5} (C_{s,\text{surf}})^{0.5}, \quad (10)$$

where K_i is the reaction rate coefficient, $C_{s,\text{max}}$ is the maximum Li concentration in the solid phase particles, $C_{s,\text{surf}}$ is the concentration of Li at the surface of solid phase particles, and C_e is the Li-ion concentration in electrolyte. The overpotential η in (9) is given by

$$\eta = \phi_s - \phi_e - U, \quad (11)$$

TABLE 1: Parameters for 1D lithium ion battery cell [2].

Parameter	Description	Negative electrode	Separator	Positive electrode
t^0	Transference number of electrolytes	0.435	0.435	0.435
L	Length of electrode (μm)	73.5	25	70
r	Solid particle radius (μm)	12.5	—	8.5
ε_s	Solid phase volume fraction	0.5052	—	0.55
ε_e	Electrolyte phase volume fraction	0.4382	0.45	0.30
ε_b	Binder volume fraction	0.0566	—	0.15
D_s	Solid phase diffusion coefficient (m^2/s)	1.4523×10^{-13}	—	1.0×10^{-11}
ρ	Active material density (kg/m^3)	2292	—	5031.67
$C_{s,\text{max}}$	Maximum concentration in solid phase (mol/m^3)	31 858	—	49 943
SOC	State of charge in charge/discharge (%)	5/95	—	95/50
$C_{l,0}$	Initial electrolyte concentration (mol/m^3)	1000	1000	1000
brug	Bruggeman coefficient for tortuosity	4.1	2.3	1.5
k_i	Reaction rate coefficient at 25°C	1.764×10^{-11}	—	6.6667×10^{-11}
K_T	Thermal conductivity ($\text{W}/(\text{m}\cdot\text{K})$)	1.7	0.16	2.1
α_a, α_c	Charge transfer coefficients	0.5, 0.5	—	0.5, 0.5
σ	Solid phase conductivity (S/m)	100	—	10

where U is the equilibrium potential which is the function of intercalated Li and is on the basis of empirical functions. The parameters used in the presented equations are listed in Table 1 which are on the basis of the work by Kumaresan et al. [2]. In addition, the equilibrium potentials for solid electrodes and electrolyte ionic conductivity as a function of Li concentration were all adopted from [2]. To calculate the effective ionic conductivity (k_{eff}) and lithium diffusion coefficients (D_{eff}) in the electrolyte in the different parts of the cell, we used the Bruggeman approximation as follows:

$$\begin{aligned} k_{\text{eff}} &= k_i \varepsilon^{\text{brug}_i}, \\ D_{\text{eff}} &= D_e \varepsilon^{\text{brug}_i}, \end{aligned} \quad (12)$$

where index i refers to different cell regions (anode, separator, or cathode) and the exponent (brug) is the Bruggeman exponents (the values are listed in Table 1). The total generated heat is taken as the sum of reaction and joule (ohmic) heats. Typically, heat generation in lithium-ion batteries can be attributed to three main sources: heat from the reaction current and overpotentials (q_r), ionic ohmic heat from the motion of lithium/lithium-ions through the solid (q_j), and reversible heat (q_{rev}). In this study, these sources of heat are expressed as follows:

$$q_r = A \int_0^L j^{\text{Li}} (\phi_s - \phi_e - U) dx, \quad (13)$$

$$q_j = A \int_0^L \sigma^{\text{eff}} \left(\frac{\partial \phi_s}{\partial x} \right)^2 dx, \quad (14)$$

$$q_{\text{rev}} = j^{\text{Li}} T \frac{\partial U}{\partial T}. \quad (15)$$

Equation (15) presents the reversible heat generation which can be either positive or negative. This is related to the entropy changes in solid electrode materials which are referred to as $\partial U/\partial T$. As discussed in [2], the reversible heat plays

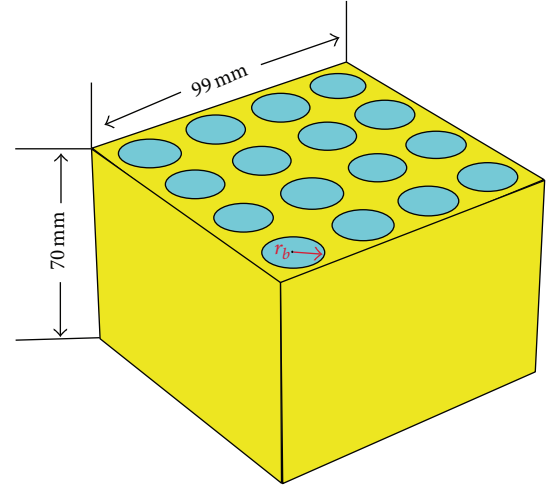


FIGURE 2: 3D heat transfer model coupled with electrochemical model to evaluate the temperature rises during the battery charging/discharging cycles. The Li-ion batteries and paraffin based structures are illustrated by blue and yellow colors, respectively. The battery radius, r_b , was chosen to be 9.2 mm. The outer surface of the model is exposed to air.

an important role in the LiCoO_2 electrode. In the present work, $\partial U/\partial T$ curves, as a function of Li concentration in solid particles, were adopted from [2]. We note that the coupled electrochemical heat transfer models have also been developed in numerous previous works [21–27].

The calculated heat generation rates based on Newman's model were then used to simulate the temperature rises in a battery pack containing 16 individual batteries. The heat transfer model is shown in Figure 2. This model includes two materials: Li-ion batteries and paraffin based structures. The material parameters used in the simulation are given in Table 2. The heat capacity of paraffin nanocomposites

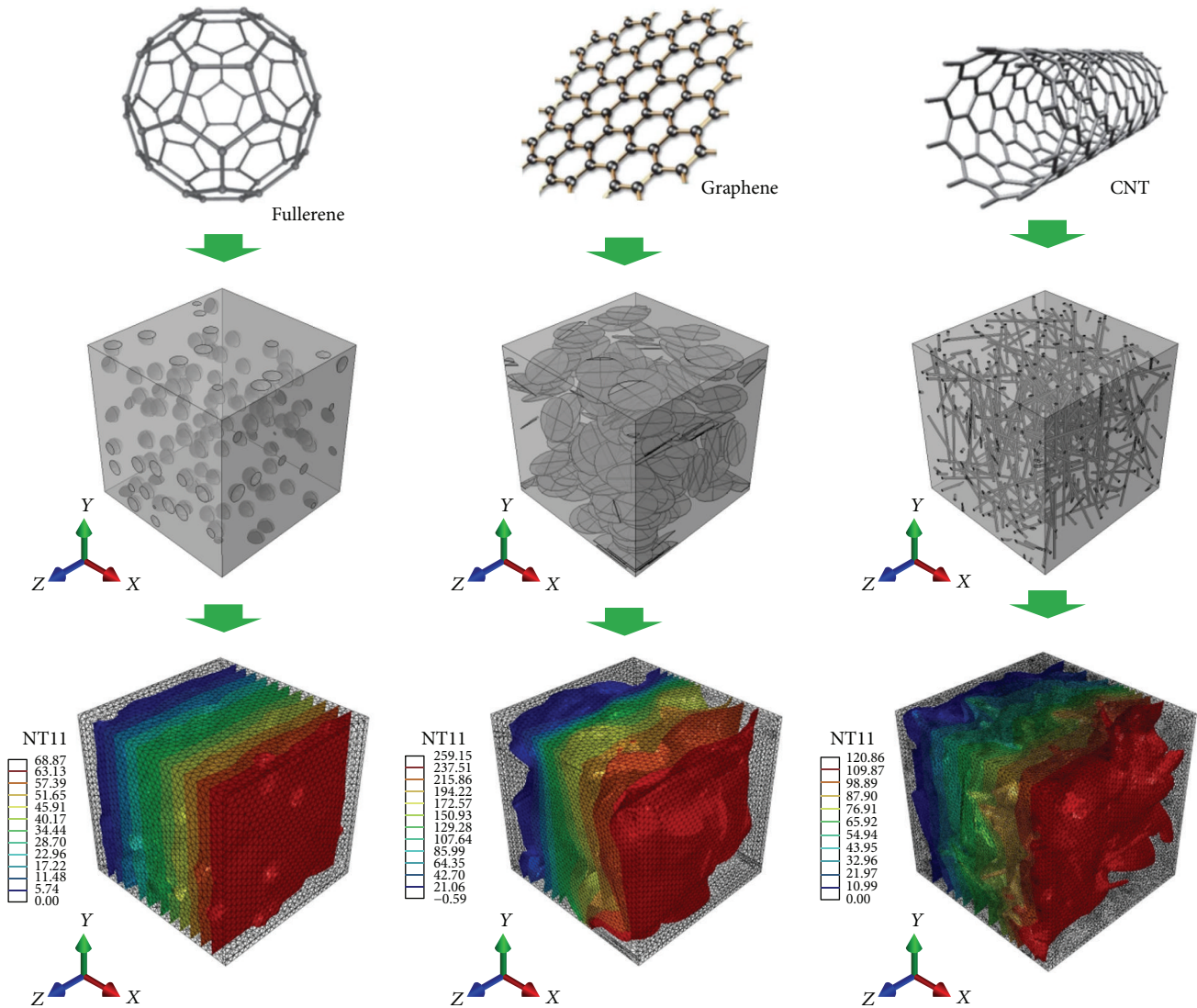


FIGURE 3: Different structures of nanofillers used in this study. We studied the thermal conductivity of paraffin nanocomposites filled with fullerene, graphene, and carbon nanotubes (CNT). Under each filler, the constructed finite element model in Abaqus is shown with 5% volume concentrations for filler. Under each finite element model, the temperature distribution obtained from the application of the heat flux is plotted.

TABLE 2: Material properties.

Material	Density (kg/m ³)	Heat capacity (J/(kg·K))	Thermal conductivity (W/(m·K))
Battery cell	2680	1280	1
Paraffin	900	2500	0.25
Fullerene	2200	717	3000
CNT	2200	717	3000
Graphene	2200	717	3000

was also calculated using the rule of mixtures. The outer surfaces of 3D heat transfer model were exposed to air with convective heat transfer coefficient of 2.5 W/m²·K.

The coupled electrochemical and heat transfer models were built in COMSOL/Multiphysics package using Li-ion battery and heat transfer modules.

In this work, we also studied the effective thermal conductivity of paraffin nanocomposites. Here, we include three different fillers of graphene, carbon nanotubes, and fullerene to study the thermal conductivities using the finite element approach. Computational limits of finite element method impose restrictions on the maximum number of elements used in a model. Thus, the simulations of composite materials are limited to the modeling of a representative volume element (RVE) of the system. In an attempt to construct the RVEs in a status closer to those in experimentally fabricated random composites, the 3D fillers were randomly distributed and oriented in the RVE. The atomic structures of three studied fillers along with the FE models constructed in

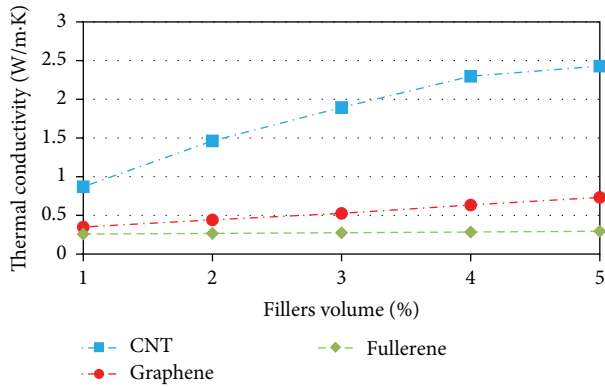


FIGURE 4: Calculated effective thermal conductivity of paraffin nanocomposites as a function of different fillers volume concentration.

ABAQUS software are illustrated in Figure 3. The RVEs were modeled in such a way that they satisfy the periodicity criterion. This means that if a filler is cut by a boundary face of RVE, the remaining part of that particle should continue from the opposite face. The random RVEs were constructed in ABAQUS by developing Python scripts as input files. We developed advanced C++ codes for creating randomly distributed/oriented fillers with high volume concentrations and without intersection [28, 29]. In our FE modeling, we assumed perfect heat transfer condition (no interfacial resistance) between the fillers and the paraffin matrix. For the evaluation of thermal conductivity, we merged two thin auxiliary parts to the RVE as discussed in our previous work [29]. We then applied a constant heat flux along the sample and based on the established temperature profile the effective thermal conductivity was evaluated which is discussed in detail in [29]. We note that length to diameter ratio for CNT (with cylindrical geometry) and diameter to thickness ratio for graphene (defined with disc geometry) were both assumed to be 50. The thermal conductivity of all fillers was assumed to be 3000 W/m·K [30]. It is worth noting that this thermal conductivity may not be realistic for fullerene. Nevertheless, based on previous theoretical investigation [11], for spherical particles the thermal conductivity of composite does not correlate strongly with the fillers to matrix, contrast in properties.

3. Results and Discussions

Figure 4 depicts the finite element results for effective thermal conductivity of paraffin nanocomposites as a function of different filler's volume concentration. It is worthy to note that in our finite element modeling, for each RVE, we calculated the effective conductivities along three Cartesian directions. For each volume concentration, three or four RVEs were constructed with different filler distributions. To obtain converged effective thermal conductivity, the results for different RVEs as well as different directions were all averaged. Our results shown in Figure 4 reveal that the thermal conductivity of paraffin can be drastically improved

by the addition of CNT. In addition, it is shown that the addition of fullerene leads to insignificant enhancement of effective thermal conductivity. In composite materials, the heat flux is transferred between matrix and filler through their contacting surfaces. Therefore, the filler's surface to volume ratio plays an important role in the final reinforcement. This can justify the least reinforcement in thermal conductivity by the addition of spherical shaped fullerene. The calculated effective parameters were then used in our 3D heat transfer model to introduce the thermal conductivity of paraffin structures.

Simulated maximum temperature rises for the battery pack for different charging/discharging C-rates are depicted in Figure 5. As the first finding, we could observe remarkable decline in temperature rises by the use of PCM materials for all applying C-rates. However, in all studied cases, fabrication of paraffin nanocomposites does not show huge effect on the temperature damping in comparison with pure paraffin. It is worthy to note that in the electrochemical simulations in this study, we considered stop conditions of 4.8 V and 3.0 V for charging and discharging cycles, respectively. This way, by increasing the C-rate, the simulations were stopped in much earlier times because of reaching the stopping criteria. So, the temperature rises decrease by increasing the C-rate because the heat generation was achieved in a much shorter time. From the theoretical point of view, by increasing the battery current, the reaction and ohmic heats ((13) and (14)) increase by the power of two while reversible heats increase linearly. On the other hand, the simulation results in Figure 5 also show that during discharging process the temperature rises are approximately twice the ones during the charging process. This is due to the fact that during the charging process reversible heat generated in the positive LiCoO_2 electrode is negative which results in the cooling of the battery. However, during the discharging process the reversible heating in the positive electrode is mainly positive leading to the heating of the batteries. It should be emphasized that based on the $\partial U/\partial T$ curves reported in [2], the reversible heating is mainly dominated by the positive LiCoO_2 electrode compared with MCMC negative electrode.

Simulation results for the maximum temperature rises for the battery pack with the use of paraffin nanocomposites with different concentrations of nanofillers during a 1C current for a single charging (a) and discharging (b) cycle are illustrated in Figure 6. As expected, by increasing the nanofiller's concentration inside the paraffin, the maximum temperature rises in the battery decrease continuously. In the discharging cycles, the maximum temperature rise decreases by around 3 K through the addition of 5% volume ratio of CNT fillers inside the paraffin which is a remarkable enhancement. This temperature decrease might be crucial in applications in which the performance of the building blocks is sensitive to the temperature changes such as in nanoelectronics. Our modeling results suggest that fabrication of paraffin nanocomposites as a PCM for the heat management of batteries could be considered as a solution if the battery is supposed to work under fast and continuous discharging cycles. Nonetheless, our simulation results clearly confirm the importance of the use of paraffin based PCMs for

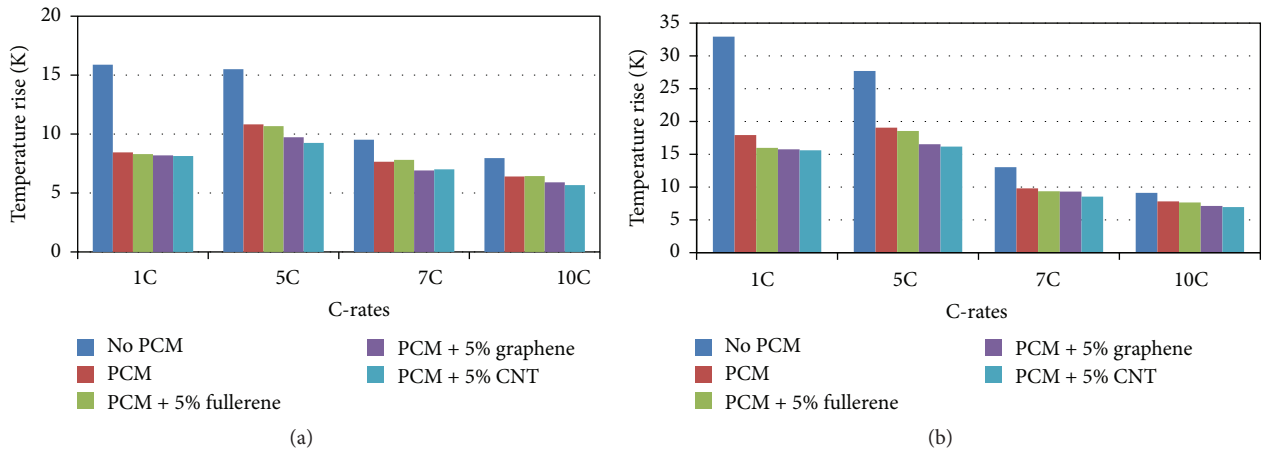


FIGURE 5: Simulated temperature rises for the battery pack for different charging (a) and discharging (b) C-rates.

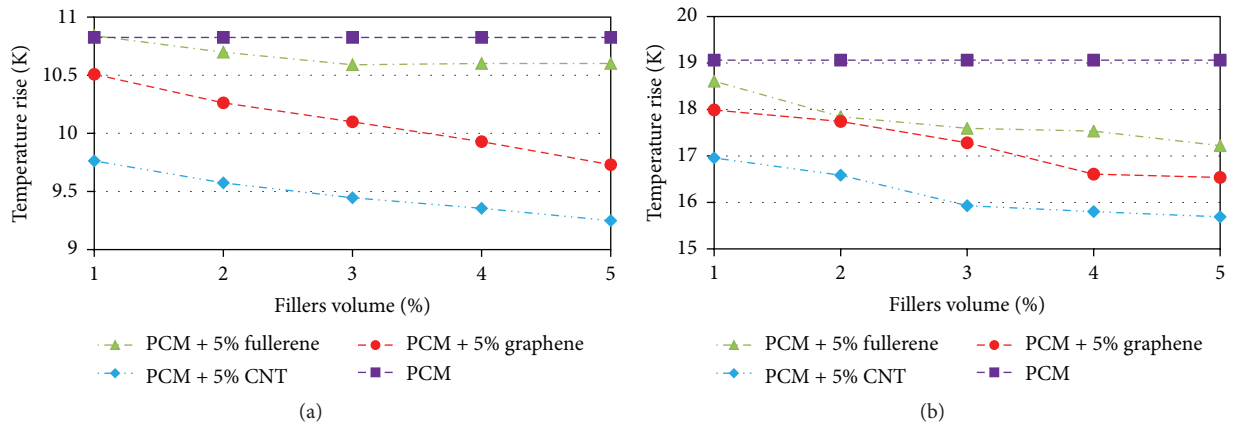


FIGURE 6: Modeling result for the maximum temperature rises for the battery pack with the use of paraffin nanocomposites with different concentrations of nanofillers during a 1C current for a single charging (a) and discharging (b) cycle.

the thermal management of Li-ion batteries for both charging and discharging cycles.

In Figure 7, two samples of calculated voltage curves and simulated 3D temperature profiles of the battery pack surrounded by a paraffin matrix mixed with 5% carbon nanotubes at different times during a 1C charging and discharging cycles are plotted. Interestingly, for the charging cycle at the time of 10 seconds we noticed that the battery pack temperature is lower than that of ambient. This means that reversible cooling due to the entropy changes that occurred in the positive electrode was large enough to surpass ohmic and reaction heat generations. The simulated temperature profiles reveal that regardless of the initial times of charging cycle, for the rest of times, the maximum temperature rises take place inside the batteries somewhere close to the center of the battery pack. Therefore, one solution to improve the temperature management of the battery pack is to include higher concentration of the fillers within the paraffin materials in the sections that are closer to the center of the pack in order to enhance the heat conduction to the surroundings. Consequently, our modeling suggests that the heat management of a battery pack can be improved by an

appropriate use of paraffin nanocomposites in the positions where the maximum temperature rises occur.

4. Conclusion

We developed an electrochemical model based on Newman's pseudo-2D model coupled with a 3D heat transfer model to investigate the heat management of a battery pack. The considered battery is made of LiCoO_2 positive composite electrode and mesocarbon microbead negative electrode. Based on the electrochemical theory, the heat generation during charging/discharging cycles was calculated which was used in the 3D heat transfer model for the evaluation of temperature rises in a battery pack under various loading conditions. Our modelling results revealed remarkable decrease in temperature rises by embedding the batteries inside a paraffin wax. This effect was found to be more considerable for discharging cycles. Then, we studied the effects of fabrication of paraffin nanocomposites on temperature rises of a battery pack. We included different carbon based nanofillers such as graphene, carbon nanotubes, and fullerene for the improvement of thermal conduction of paraffin. The thermal conductivity

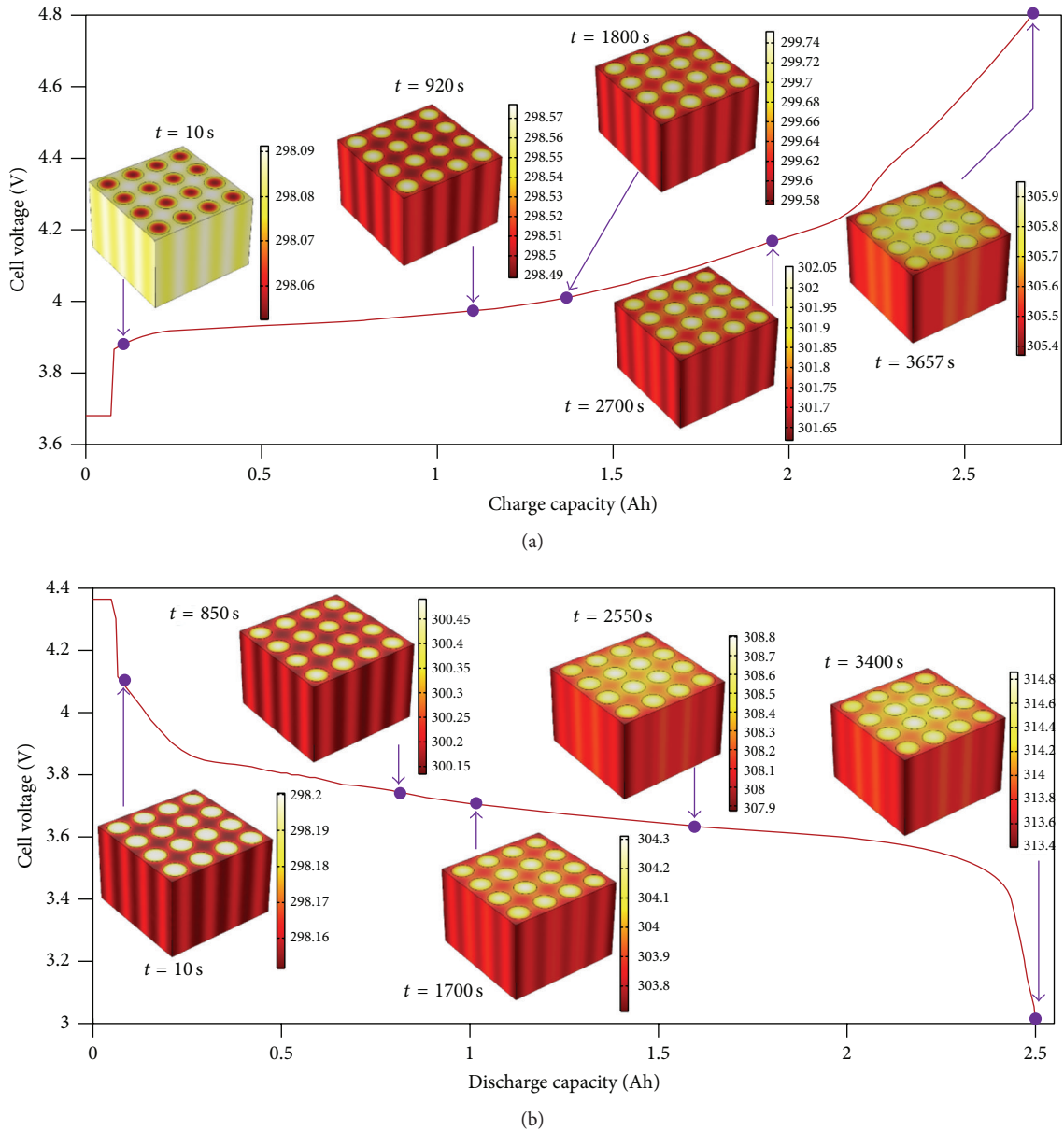


FIGURE 7: Calculated voltage curves and simulated 3D temperature profiles at various times during a 1C charging (a) and discharging (b) cycle. The ambient temperature was set to the room temperature (298.15 K).

for all fillers has been considered to be the same so that our emphasis in the present study is related to the effect of fillers geometry. The effective thermal conductivity of paraffin nanocomposites was evaluated using advanced 3D finite element models. It is shown that the fabrication of paraffin nanocomposites can increase the enhancement of the heat management of batteries. In this case, a favorable case was found to be the paraffin wax that was enhanced by the carbon nanotubes. We note that we did not include the effect of temperature on the thermal properties of paraffin structures; however, a separate investigation can be yet conducted in this direction. It was shown that during the charging process,

the reversible heat generated in the positive LiCoO_2 resulted in the cooling of the battery so that there is a remarkably lower temperature rises compared to discharging cycles. Our modeling results suggest that fabrication of paraffin nanocomposites for the heat management of batteries can be considered as a promising solution if the battery is to be work under fast and continuous discharging cycles. In summary, the proposed modeling methodology can be considered as an efficient method for the design of Li-ion batteries packs with enhanced heat management. In the future, we intend to extend our framework to a multiscale approach accounting also for the fine scale features [31–35] of the batteries which

is of utmost importance for the design of new battery materials.

Conflict of Interests

The authors declare that there is no conflict of interests regarding the publication of this paper.

Acknowledgment

The authors greatly acknowledge the financial support by European Union through ERC grant for COMBAT project.

References

- [1] P. Goli, S. Legedza, A. Dhar, R. Salgado, J. Renteria, and A. A. Balandin, "Graphene-enhanced hybrid phase change materials for thermal management of Li-ion batteries," *Journal of Power Sources*, vol. 248, pp. 37–43, 2014.
- [2] K. Kumaresan, G. Sikha, and R. E. White, "Thermal model for a Li-ion cell," *Journal of the Electrochemical Society*, vol. 155, no. 2, pp. A164–A171, 2008.
- [3] V. Goyal and A. A. Balandin, "Thermal properties of the hybrid graphene-metal nano-micro-composites: applications in thermal interface materials," *Applied Physics Letters*, vol. 100, Article ID 073113, 2012.
- [4] M. D. Zolot, K. Kelly, M. Keyser, M. Mihalic, and A. Pesaran, "Thermal evaluation of the Honda insight battery pack," in *Proceedings of the 36th Intersociety Energy Conversion Engineering Conference*, Savannah, Ga, USA, June 2001.
- [5] K. Yeow, H. Teng, M. Thelliez, and E. Tan, "3D thermal analysis of Li-ion battery cells with various geometries and cooling conditions using abaqus," in *Proceedings of the SIMULIA Community Conference*, Providence, RI, USA, May 2012.
- [6] R. Benger, H. Wenzl, H.-P. Beck, M. Jiang, D. Ohms, and G. Schaedlich, "Electrochemical and thermal modeling of lithium-ion cells for use in HEV or EV application," *World Electric Vehicle Journal*, vol. 3, no. 1, pp. 342–351, 2009.
- [7] S. K. Mohammadian, Y. He, and Y. Zhang, "Internal cooling of a lithium-ion battery using electrolyte as coolant through microchannels embedded inside the electrodes," *Journal of Power Sources*, vol. 293, pp. 458–466, 2015.
- [8] A. Sharma, V. V. Tyagi, C. R. Chen, and D. Buddhi, "Review on thermal energy storage with phase change materials and applications," *Renewable and Sustainable Energy Reviews*, vol. 13, no. 2, pp. 318–345, 2009.
- [9] S. Ghosh, W. Bao, D. L. Nika et al., "Dimensional crossover of thermal transport in few-layer graphene," *Nature Materials*, vol. 9, no. 7, pp. 555–558, 2010.
- [10] K. M. F. Shahil and A. A. Balandin, "Graphene-multilayer graphene nanocomposites as highly efficient thermal interface materials," *Nano Letters*, vol. 12, no. 2, pp. 861–867, 2012.
- [11] B. Mortazavi, J. Bardon, and S. Ahzi, "Interphase effect on the elastic and thermal conductivity response of polymer nanocomposite materials: 3D finite element study," *Computational Materials Science*, vol. 69, pp. 100–106, 2013.
- [12] N. Sheng, M. C. Boyce, D. M. Parks, G. C. Rutledge, J. I. Abes, and R. E. Cohen, "Multiscale micromechanical modeling of polymer/clay nanocomposites and the effective clay particle," *Polymer*, vol. 45, no. 2, pp. 487–506, 2004.
- [13] Q. H. Zeng, A. B. Yu, and G. Q. Lu, "Multiscale modeling and simulation of polymer nanocomposites," *Progress in Polymer Science*, vol. 33, no. 2, pp. 191–269, 2008.
- [14] D. Luo, W.-X. Wang, and Y. Takao, "Effects of the distribution and geometry of carbon nanotubes on the macroscopic stiffness and microscopic stresses of nanocomposites," *Composites Science and Technology*, vol. 67, no. 14, pp. 2947–2958, 2007.
- [15] J. D. Renteria, D. L. Nika, and A. A. Balandin, "Graphene thermal properties: applications in thermal management and energy storage," *Applied Sciences*, vol. 4, no. 4, pp. 525–547, 2014.
- [16] J. Renteria, S. Legedza, R. Salgado et al., "Magnetically-functionalized self-aligning graphene fillers for high-efficiency thermal management applications," *Materials & Design*, vol. 88, pp. 214–221, 2015.
- [17] J. D. Renteria, S. Ramirez, H. Malekpour et al., "Strongly anisotropic thermal conductivity of free-standing reduced graphene oxide films annealed at high temperature," *Advanced Functional Materials*, vol. 25, no. 29, pp. 4664–4672, 2015.
- [18] A. A. Khatibi and B. Mortazavi, "A study on the nanoindentation behaviour of single crystal silicon using hybrid MD-FE method," *Advanced Materials Research*, vol. 32, pp. 259–262, 2008.
- [19] B. Mortazavi, A. A. Khatibi, and C. Politis, "Molecular dynamics investigation of loading rate effects on mechanical-failure behaviour of FCC metals," *Journal of Computational and Theoretical Nanoscience*, vol. 6, no. 3, pp. 644–652, 2009.
- [20] J. Newman and K. E. Thomas-Alyea, *Electrochemical Systems*, John Wiley & Sons, Prentice-Hall, Eaglewood Cliffs, NJ, USA, 3rd edition, 2004.
- [21] M. Guo and R. E. White, "A distributed thermal model for a Li-ion electrode plate pair," *Journal of Power Sources*, vol. 221, pp. 334–344, 2013.
- [22] K. Smith and C.-Y. Wang, "Power and thermal characterization of a lithium-ion battery pack for hybrid-electric vehicles," *Journal of Power Sources*, vol. 160, no. 1, pp. 662–673, 2006.
- [23] L. Cai and R. E. White, "Mathematical modeling of a lithium ion battery with thermal effects in COMSOL Inc. Multiphysics (MP) software," *Journal of Power Sources*, vol. 196, no. 14, pp. 5985–5989, 2011.
- [24] B. Wu, V. Yufit, M. Marinescu, G. J. Offer, R. F. Martinez-Botas, and N. P. Brandon, "Coupled thermal-electrochemical modelling of uneven heat generation in lithium-ion battery packs," *Journal of Power Sources*, vol. 243, pp. 544–554, 2013.
- [25] M. Sievers, U. Sievers, and S. S. Mao, "Thermal modelling of new Li-ion cell design modifications," *Forschung im Ingenieurwesen*, vol. 74, no. 4, pp. 215–231, 2010.
- [26] H. Maleki, S. Al Hallaj, J. R. Selman, R. B. Dinwiddie, and H. Wang, "Thermal properties of lithium-ion battery and components," *Journal of the Electrochemical Society*, vol. 146, no. 3, pp. 947–954, 1999.
- [27] A. H. N. Shirazi, M. R. Azadi Kakavand, and T. Rabczuk, "Numerical study of composite electrode's particle size effect on the electrochemical and heat generation of a Li-ion battery," *Journal of Nanotechnology in Engineering and Medicine*, In press.
- [28] B. Mortazavi, F. Hassouna, A. Laachachi et al., "Experimental and multiscale modeling of thermal conductivity and elastic properties of PLA/expanded graphite polymer nanocomposites," *Thermochimica Acta*, vol. 552, pp. 106–113, 2013.
- [29] B. Mortazavi, O. Benzerara, H. Meyer, J. Bardon, and S. Ahzi, "Combined molecular dynamics-finite element multiscale modeling of thermal conduction in graphene epoxy nanocomposites," *Carbon*, vol. 60, pp. 356–365, 2013.

- [30] A. A. Balandin, "Thermal properties of graphene and nanostructured carbon materials," *Nature Materials*, vol. 10, no. 8, pp. 569–581, 2011.
- [31] P. R. Budarapu, R. Gracie, S. P. A. Bordas, and T. Rabczuk, "An adaptive multiscale method for quasi-static crack growth," *Computational Mechanics*, vol. 53, no. 6, pp. 1129–1148, 2014.
- [32] P. R. Budarapu, R. Gracie, S.-W. Yang, X. Zhuang, and T. Rabczuk, "Efficient coarse graining in multiscale modeling of fracture," *Theoretical and Applied Fracture Mechanics*, vol. 69, pp. 126–143, 2014.
- [33] H. Talebi, M. Silani, S. P. A. Bordas, P. Kerfriden, and T. Rabczuk, "Molecular dynamics/xfem coupling by a three-dimensional extended bridging domain with applications to dynamic brittle fracture," *International Journal for Multiscale Computational Engineering*, vol. 11, no. 6, pp. 527–541, 2013.
- [34] H. Talebi, M. Silani, S. Bordas, P. Kerfriden, and T. Rabczuk, "A computational library for multiscale modeling of material failure," *Computational Mechanics*, vol. 53, no. 5, pp. 1047–1071, 2014.
- [35] H. Talebi, M. Silani, and T. Rabczuk, "Concurrent multiscale modeling of three dimensional crack and dislocation propagation," *Advances in Engineering Software*, vol. 80, pp. 82–92, 2015.

Research Article

Parametric Study of Strain Rate Effects on Nanoparticle-Reinforced Polymer Composites

B. Soltannia,¹ I. Haji Gholami,² S. Masajedian,³ P. Mertiny,¹ D. Sameoto,¹ and F. Taheri⁴

¹Mechanical Engineering Department, University of Alberta, Edmonton, AB, Canada T6G 1H9

²Mechanical Engineering Department, Sharif University of Technology, Tehran 1458889694, Iran

³Civil Engineering Department, University of Alberta, Edmonton, Canada

⁴Civil and Resource Engineering Department, Dalhousie University, Halifax, NS, Canada B3H 4R2

Correspondence should be addressed to F. Taheri; farid.taheri@dal.ca

Received 4 September 2015; Revised 22 October 2015; Accepted 27 October 2015

Academic Editor: Timon Rabczuk

Copyright © 2016 B. Soltannia et al. This is an open access article distributed under the Creative Commons Attribution License, which permits unrestricted use, distribution, and reproduction in any medium, provided the original work is properly cited.

Crashworthiness, energy absorption capacity, and safety are important factors in the design of lightweight vehicles made of fiber-reinforced polymer composite (FRP) components. The relatively recent emergence of the nanotechnology industry has presented a novel means to augment the mechanical properties of various materials. As a result, recent attempts have contemplated the use of nanoparticles to further improve the resiliency of resins, especially when resins are used for mating FRP components. Therefore, a comprehensive understanding of the response of nanoreinforced polymer composites, subjected to various rates of loading, is of paramount importance for developing reliable structures. In this paper, the effects of nanoreinforcement on the mechanical response of a commonly used epoxy resin subjected to four different strain rates, are systematically investigated. The results are then compared to those of the neat resin. To characterize the mechanical properties of the nanocomposite, a combination of the strain rate-dependent mechanical (SRDM) model of Goldberg and his coworkers and Halpin-Tsai's micromechanical approach is employed. Subsequently, a parametric study is conducted to ascertain the influences of particle type and their weight percentage. Finally, the numerical results are compared to the experimental data obtained from testing of the neat and the nanoreinforced epoxy resin.

1. Introduction

Nanoparticle-reinforced polymer composites (NRPs) are receiving special attention, especially for bonding applications in automotive, marine, aerospace, and oil and gas industries. NRPs are known to enhance the mechanical, electrical, thermal, and permeability properties and diffusion barrier attributes of their host polymers. Moreover, in some cases, they could also provide self-healing ability. The enactment of mechanical properties gained by inclusion of nanoparticles includes improved strength and stiffness to weight and cost ratios, improved fatigue and corrosion resistance, more controllable damage mechanism, and augmentation of the energy-absorption capacity of their host polymer. Therefore, these attributed properties render them as effective candidates for reinforcing polymers [1–11].

Nanoparticle-reinforced polymer composites (NRPs) are increasingly being used in various engineering applications, especially in the form of adhesives. Adhesives are becoming increasingly more popular for joining structural components because of the recent advancements in techniques used for toughening them. One such emerging technique has been the inclusion of an appropriate amount of inexpensive nanocarbon, namely, Graphene Nanoplatelets (GNPs), in resins/adhesives. GNPs, which have larger diameter and aspect ratio than their more commonly used nanocarbon tubes counterpart, are less expensive and are more widely available.

One of the thrusts of our current research has been to promote the use of NRPs, in form of adhesives, in automobile applications. In such applications, the NRPs become often subject to large loading rates. Unfortunately, there is a

clear paucity in databases that convey the performance of nanoparticle-reinforced adhesives, especially when subject to high loading (or strain) rates. This issue, in turn, has impeded the greater usage of NRPs in such engineering applications. Therefore, the mechanical characterization of such nanoreinforced adhesives is vital, especially when they are subject to large loading rates.

The use of carbon nanotubes, which are essentially sheets of graphite rolled into tubes [12, 13], was first proposed by Iijima in 1991 and later by Iijima and Ichihashi in 1993. Even though CNTs (both single-walled and multiwalled varieties) are quite flexible in the direction perpendicular to their longitudinal axis [14], the strength and elastic modulus of MWCNTs have been estimated to be as high as 150 GPa and 900 GPa, respectively [15]. Their superior mechanical characteristics and optimal length-to-diameter ratio have rendered CNTs as an effective reinforcing agent for resins. Nevertheless, in order to fully harness the exceptional mechanical properties of CNTs, a strong interfacial bond between the polymer matrix and CNTs must exist [16].

Since the advent of nanotechnology, nanoparticle-reinforced adhesives have also been increasingly used in many other advanced applications such as naval, automotive, aerospace, and medical industries. Kim and Reneker reported that Young's modulus of a nanofiber-reinforced composite was ten times greater than that of the neat adhesive [17]. It has also been demonstrated that MWCNT particles enhance the strength and toughness of epoxies, because nanoparticles strengthen the polymeric chains of the resin and resist crack initiation and propagation by acting as bridges [18]. Qian et al. suggested that nanotubes (CNTs) could enhance the composite strength by as much as 25% [19]. It should also be noted that a nanoparticle-reinforced adhesive with the most optimum properties can only be produced if the nanoparticles are distributed uniformly and fully dispersed (exfoliated) within the polymer. This is a very challenging process, because the formation of agglomerations can act as defect regions, thus reducing the performance instead of enhancing it.

Despite the noted studies, to date, there are only a limited number of studies that have explored the mechanical properties of resins reinforced with carbon nanoparticles, especially GNPs. Moreover, the lack of such studies becomes even more noticeable when one requires information on the effect of loading/strain rates on the response of nanoparticle-reinforced resins.

Therefore, in order to better understand the mechanical behavior of the nanoparticle-reinforced polymer composites under dynamic loading conditions (hence, to be able to establish and assess the safety factor of the structure hosting NRPs), one should gain a better understanding of the mechanical response of such resins under different strain rates. Several researchers have demonstrated the rate-dependent mechanical behavior of neat polymers and have developed constitutive models for their characterization (see, for instance, [20–28]). Notwithstanding the abovementioned studies and those alike, there exists no unified and robust theoretical approach capable of mimicking the atomic interaction between nanoparticles and polymers. The involved

challenges in constructing such a model have therefore necessitated the use of multiscale techniques to identify the macroscale mechanical behavior of nanoparticle-reinforced polymer composites. An example of such modeling approach can be found in the work of Shokrieh et al. [29]. They incorporated a strain rate-dependent continuum-based macroscale level constitutive model developed by Goldberg et al. [22–24], combined with the Halpin-Tsai micromechanical model [30], to study the loading rate effects on a CNT-reinforced polymer composite.

In this paper, using a similar approach adopted by Shokrieh et al. [29], the effects of nanoreinforcement on the mechanical response of a nanoreinforced resin, subjected to different strain rates, are modeled and systematically investigated. More specifically, neat and nanoreinforced resins are subjected to tensile loadings applied at the rates of 1.5, 15, 150, and 1500 mm/min (strain rates of 10^{-3} , 10^{-2} , 10^{-1} , and 1 s^{-1}). Subsequently, a parametric study is conducted to ascertain the influences of various parameters (i.e., the particle type, their weight percentage) on the mechanical properties of the nanocomposite. Finally, the numerical results are compared to the experimental data obtained for the neat and the nanoreinforced epoxy resins [31, 32].

2. Experimental Investigation

2.1. Materials and Specimen Preparation. A commonly used thermoset epoxy resin (i.e., the West System 105 resin and 206 hardener (Bay City, MI)) was used as the baseline adhesive to fabricate the test specimens. This resin was selected, because it is a commonly used resin, has a relatively low cost, and is readily available.

In order to establish a cost-effective means for enhancing the mechanical properties of the resin/adhesive, different types of nanocarbon particles were utilized as the reinforcing agent. However, the uniform distribution and dispersion of nanocarbon particles in resin were found to be quite time-consuming and challenging, hence increasing the processing cost. It should be noted that not only do the distribution and dispersion of particles directly influence adhesive's mechanical properties, but also more importantly the nanoparticle agglomeration results in significant statistical discrepancies in performance of the final product.

Three different forms of nanocarbon particles were chosen to be dispersed into the epoxy resin:

- (i) Graphitized Carbon Nanofibers (CNFs) with an outer diameter of 200 to 600 nm and more than 99.9% purity (obtained from the US Research Nanomaterials, Inc., Houston, TX).
- (ii) Graphene Nanoplatelets (GNP-M-25) with an average diameter of 25 μm , thickness of 6 nm, and surface area of 100 m^2/g (obtained from XG Science Ltd., Lansing, MI).
- (iii) Multiwalled Carbon Nanotubes (MWCNTs) with an outer diameter of 5 to 15 nm and more than 95% purity (obtained from the US Research Nanomaterials, Inc., Houston, TX).

To facilitate uniform dispersion of the nanoparticles in resin, a mechanical stirrer was used first. Each slurry of resin/nanoparticle was stirred at a speed of 2000 rpm for 10 min. This procedure was followed by calendering the resin/nanoparticles mix with a three-roll mill. The calendering rollers' speed was set to the machine's maximum rotational speed of 174 RPM. To maximize dispersion quality and minimize agglomerations, the calendering was performed seven times. The roller gaps were set at $20\ \mu\text{m}$. Note that concentrations of CNF, MWCNT, and GNP with weight percentages of 0.25%, 0.5%, and 1% were considered. It should be noted that selection of the rollers gap size is quite important. It is postulated that when the nanoparticles are dispersed into adhesives, they are surrounded by monomer molecules. After each round, the quality of the distribution and dispersion was monitored by sampling the mixed slurry and assessing the uniformity of the dispersion with a digital microscope.

The subsequent addition of the curing agent would initiate the chemical reaction process of the resin, promoting the monomer molecules to surround the GNPs as the resin cures. In addition to the mechanical bonding, chemical bonding known as Van der Waals bond is also generated. The inclusion of nanoparticles into resin also increases resin's viscosity (thickens it). It should also be noted that, in comparison to other types of nanoparticles (e.g., CNFs or CNTs), the relatively greater aspect ratio of GNPs helps to increase the resin/nanoparticles interactions, thus forming a tougher adhesive.

Following the aforementioned procedures, the curing agent (hardener) was added to the slurry and mixed using a stirrer at a speed of 400 rpm for 4 to 6 minutes. The mixture was then degassed under $28''\ \text{Hg}$ vacuum for 2 to 3 minutes (the degassing time period depends on the gel time of the resin). After degassing, the mixture was poured into appropriately designed and fabricated molds and allowed to cure for at least 12 hours at room temperature. The final products in the form of dog-bone tensile coupons with dimensions as per ASTM D638 for both neat and nanoparticle-reinforced resins are shown in Figure 1 [33].

2.2. Characterization of the Mechanical Properties of Adhesives. The prepared dog-bone shaped samples were tested in tension using an Instron servo-hydraulic universal test machine equipped with 8500⁺ electronics. To establish the stress-strain characteristics of the neat and nanoreinforced resins, the specimens were subjected to a displacement-controlled tensile loading [33]. First, tensile tests were performed on the neat resin at room temperature, at cross-head speeds of 1.5, 15, and 150 mm/min, per ASTM D 897 (as the baseline tests for the static and quasistatic loading conditions), and at 1500 mm/min, per ASTM D 950 (as the baseline tests for the high-strain rate loading condition) [34, 35]. Subsequently, the reinforced adhesive specimens underwent testing with the same loading rates. The gauge-length displacement of specimens tested under quasistatic loading rates (1.5 mm/min) was recorded using an Instron extensometer (Instron Industrial Products, Grove, PA) as well as an EIR Laser Extensometer (Electronic Instrument

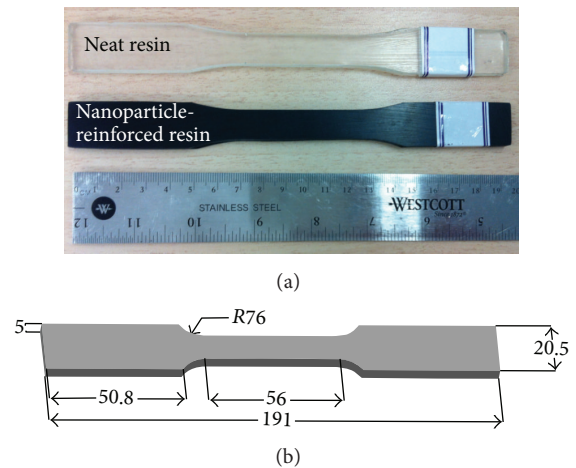


FIGURE 1: Representative tensile coupons of the neat and nanoparticle-reinforced epoxy resins and their dimensions (in mm).

Research, Irwin, PA). An Instron dynamic extensometer and the laser extensometer were used to record the gauge-length displacement of the specimens tested under the quasistatic and higher loading rate experiments (i.e., 15, 150, and 1500 mm/min), as shown in Figure 2. Using the recorded load and gauge length displacement, the stress-strain curve of each adhesive was constructed and their elastic modulus was evaluated. The initial gauge length for all cases was 25.4 mm.

The experimental results revealed that not only did the inclusion of nanoparticles improve the mechanical properties of the adhesive, but it also enhanced the resin's viscosity. The improved viscosity renders the adhesive suitable for use in adhesively bonded joints that oriented vertically, which are often encountered in several industrial applications, especially in marine and other applications where relatively thick bond-lines are commonly used [31, 32].

Figure 3 shows that the inclusion of the nanoparticles produced the same effect as did the increase in the strain rate. In other words, the increase in the amount of dispersed nanoparticles enhanced the stiffness of the matrix; similarly, the apparent stiffness of the composite increased as the applied strain rate increased.

3. Problem Statement and Modeling Strategy

The rate-dependent mechanical behavior of nanoparticle-reinforced polymers has been studied by different researchers. Nonetheless, to the best of the authors' knowledge, there exists a clear lack of coherent and comprehensive parametric studies that have either theoretically or experimentally characterized the effects of nanoparticle types, their weight content, and strain rates on their response. Therefore, in this work, the macroscale rate-dependent constitutive equation of Goldberg et al. [22–24] will be modified by incorporating the Halpin-Tsai micromechanical model [30], including the inclusion of more specific shape factors, in order to assess the influence of different strain rates on the response of a polymer

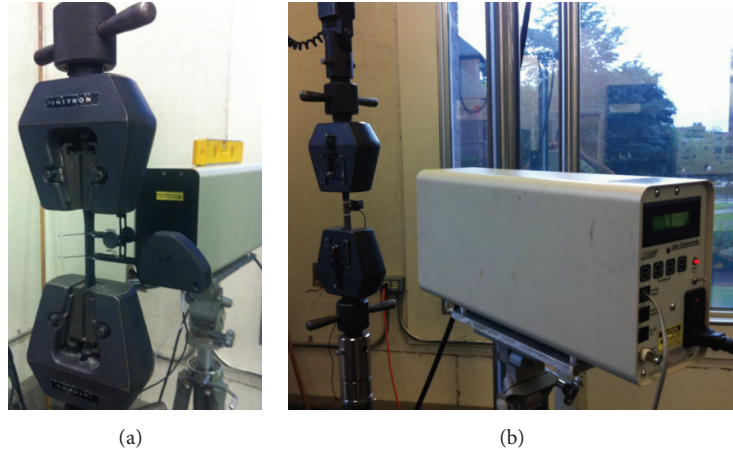


FIGURE 2: Experimental setup for the (a) static and (b) quasistatic and higher loading rate tests.

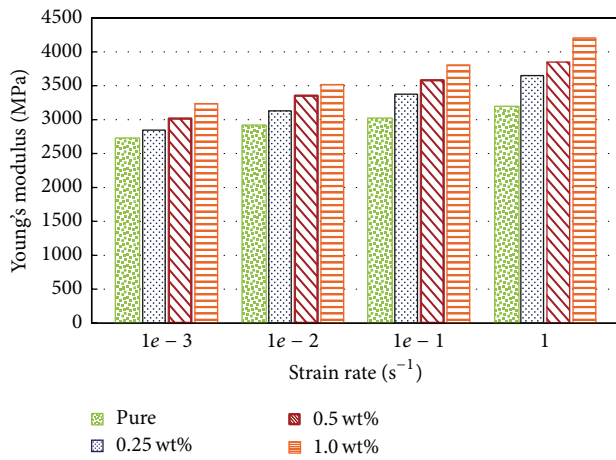


FIGURE 3: Influence of strain rate on the tensile elastic modulus of the epoxy resin reinforced with various amounts (wt%) of GNPs.

reinforced by different types of nanoparticles with various weight contents. The predicted results obtained through the aforementioned superposition technique (as incorporated by Shokrieh et al. [29]) will be validated with the experimental results. At this juncture, it should be noted that one could equally adopt other micromechanical modeling techniques (such as that developed by Mori-Tanaka [4, 6], or others), in place of the Halpin-Tsai model used in this study.

3.1. Strain Rate-Dependent Continuum-Based Constitutive Equation of Polymers. Various researchers [21–24] have shown that the stress-strain response of nanoparticle-reinforced polymer composites is dominated by the nonlinear response of its main constituent. In order to determine the viscoelastic-viscoplastic response of the polymer, the total strain (ϵ^T) can be decomposed into elastic (ϵ^E) and inelastic (ϵ^I) components. Analogously, the inelastic strain can be calculated as the difference of the total strain and elastic strain.

Goldberg et al. [22–24] proposed a model for predicting the viscoplastic response of neat polymers, utilizing

a set of state variables as an indication of the resistance of polymeric chains against flow. It should also be mentioned that polymer's mechanical properties and loading/strain rate are the two main parameters that govern the nonlinear response of the polymer. The inelastic strain components can be expressed in terms of the deviatoric stress components as follows [21–24]:

$$\dot{\epsilon}_{ij}^I = 2D_0 \exp \left[-\frac{1}{2} \left(\frac{Z}{\sigma_e} \right)^{2n} \right] \left(\frac{S_{ij}}{2\sqrt{J_2}} + \alpha \delta_{ij} \right), \quad (1)$$

where $\dot{\epsilon}_{ij}^I$ is the inelastic strain rate tensor which can be defined as a function of deviatoric stress; J_2 is the second invariant of the deviatoric stress tensor; and Z and α are the state variables. Moreover, D_0 and n are material constants; D_0 represents the maximum inelastic strain rate; and n controls the rate dependency of the material. The equivalent (effective) stress is also defined as a function of the mean stress, such that the summation of the normal stress components σ_{kk} is three times of the mean stress, as follows:

$$\sigma_e = \sqrt{3J_2} + \sqrt{3}\alpha\sigma_{kk}, \quad (2)$$

where α controls the level of hydrostatic stress' effect as a state variable. The term $\dot{\epsilon}_e^I$ represents the effective deviatoric inelastic strain rate $\dot{\epsilon}_{ij}^I$:

$$\dot{\epsilon}_e^I = \sqrt{\frac{2}{3} \dot{\epsilon}_{ij}^I \dot{\epsilon}_{ij}^I}, \quad (3)$$

$$\dot{\epsilon}_{ij}^I = \dot{\epsilon}_{ij}^I - \frac{\dot{\epsilon}_{kk}^I}{3} \delta_{ij}. \quad (4)$$

The rate of change of the other two-state variables, Z and α , can be determined using the following evolution equations:

$$\dot{Z} = q(Z_1 - Z) \dot{\epsilon}_e^I, \quad (5)$$

$$\dot{\alpha} = q(\alpha_1 - \alpha) \dot{\epsilon}_e^I.$$

Here, q is a material constant, representing the hardening rate, which is determined through trial and error, based on the inelastic shear strain attaining a plateau, or the tensile strain corresponding to the saturation region of the stress-strain curve. Z_1, α_1 are material constants, representing the maximum values of Z and α . Z_0 and α_0 are the initial values of the material constants Z and α . Z_0 is the magnitude of the stress at the point where the shear stress-strain curve becomes nonlinear. α_0 and α_1 are defined using (2) and tensile stress-strain and shear stress-strain curves (the values of stress at the plateau and first nonlinearity points of the stress-strain curves, resp.).

The material constants $Z_1, Z_0, \alpha_1, \alpha_0, n$, and D_0 can be determined using the shear stress-strain and tensile or compression stress-strain curves, obtained by experiments conducted under constant strain rates on neat polymers. Empirically, it has been shown that the value of D_0 , quantitatively, can be set equal to 10^4 times the maximum applied total strain rate; qualitatively, it is the restricting (controlling) value of the inelastic strain rate. The values of n, Z_1 can be identified using the shear stress-strain curves constructed under various strain rates. The plateau region of the effective stress under a uniaxial tensile loading at a particular strain rate corresponds to the saturation region of the effective stress obtained under pure shear loading.

To solve the implicit Goldberg constitutive equation (1), one should utilize an appropriate numerical discretization technique. Moreover, one should ensure that the selected technique for solving the equation would be stable. For that, the four-step Runge-Kutta (R-K-4) method is adopted and implemented in this work, which is similar to the procedure that was first proposed by Tabiei and Aminjikai [36, 37] and was also used by Shokrieh et al. [29]. The numerical representations of (1) and (5) take the following incremental forms after multiplying the rate-dependent equation by the time step (dt):

$$d\epsilon_{ij}^I = \left(2D_0 \exp \left[-\frac{1}{2} \left(\frac{Z}{\sigma_e} \right)^{2n} \right] \left(\frac{S_{ij}}{2\sqrt{J_2}} + \alpha \delta_{ij} \right) \right) dt, \quad (6)$$

$$d\epsilon_{ij}^I = d\epsilon_{ij}^I - \frac{d\epsilon_{kk}^I}{3} \delta_{ij}, \quad (7)$$

$$d\epsilon_e^I = \sqrt{\frac{2}{3} d\epsilon_{ij}^I d\epsilon_{ij}^I}, \quad (8)$$

$$dZ = q (Z_1 - Z) d\epsilon_e^I, \quad (9)$$

$$d\alpha = q (\alpha_1 - \alpha) d\epsilon_e^I. \quad (10)$$

As in any forward numerical method, the parameters' values from a previous step are available to be used as an input in the subsequent step. Therefore, usually a value less than the yield stress is considered as the initial guess for σ_{ij}^n to start the numerical integration. Another given input parameter is the total strain rate, $\dot{\epsilon}_{ij}^{(n+1)}$, which can be described as

$$\dot{\epsilon}_{ij}^{(n+1)} = \dot{\epsilon}_{ij}^{(n)} + \dot{\epsilon}_{ij}^{(n+1)} dt. \quad (11)$$

As the first time step of the R-K-4, values of $\sigma_{ij} = \sigma_{ij}^{m(0)}$, $Z = Z^{m(0)} = Z_0$, and $\alpha = \alpha^{m(0)} = \alpha_0$ are considered as the input parameters (note: the superscript "m" refers to the matrix). For an initial guess, the magnitude of $\sigma_{ij}^{m(0)}$ is selected such that it is less than the material's yield strength. One can then determine the values of $d\epsilon_{ij}^I$ by substituting the values of Z_0 and α_0 into (6). As a result, based on (4), (6), and (8)–(10), the first step of the R-K-4 can be represented as follows:

$$\begin{aligned} d\epsilon_{ij}^{I(\text{step1})} &= d\epsilon_{ij}^I, \\ dZ^{(\text{step1})} &= dZ, \\ d\alpha^{(\text{step1})} &= d\alpha, \\ \epsilon_{ij}^I &= \epsilon_{ij}^{I(n)} + \frac{1}{2} d\epsilon_{ij}^{I(\text{step1})}, \\ \{\sigma\} &= [C_m] (\{\epsilon\}^{n+1} - \{\epsilon\}^I), \\ Z &= Z^{m(n)} + \frac{1}{2} dZ^{(\text{step1})}, \\ \alpha &= \alpha^{m(n)} + \frac{1}{2} d\alpha^{(\text{step1})}, \end{aligned} \quad (12)$$

where $[C_m]$ is the stiffness matrix of the polymer and the stress can be determined based on elastic and inelastic strain's constituents. The remaining steps of the R-K-4 procedure are shown in Appendix.

3.2. The Halpin-Tsai Micromechanical Model. There are different micromechanical models available for characterizing the elastic behavior of nanoparticle-reinforced polymer composites under static loading condition. The models developed by Halpin-Tsai, Mori-Tanaka, and Nielsen, to mention a few [4–6, 30], are some examples. The Halpin-Tsai model [4–6, 30] used in this work can be expressed in the following form:

$$\frac{E_c}{E_m} = \frac{1 + \xi \eta \phi}{1 - \eta \phi}, \quad (13)$$

$$\text{where, } \eta = \left(\frac{E_f}{E_m} - 1 \right) \left(\frac{E_f}{E_m} + \xi \right)^{-1},$$

where E_c is the composite's tangential modulus, which can be determined by another equation developed by Halpin and Kardos [30], E_m is the tangential modulus of neat polymer, determined using the predicted stress-strain curve as described in the previous section, and E_f is the nanoparticle's modulus of elasticity. Moreover, ϕ is the nanoparticles volume fraction in the mixture. Depending on the nanoparticles type, different shape factors, ξ , would have to be used (i.e., $\xi_{\text{GNP}}^I = 2(l/t)$, $\xi_{\text{GNP}}^I = 2$, and $\xi_{\text{CNT}} = 2(l/d)$, where l , t , and d refer to the length, thickness, and diameter of the nanoparticles).

In the following section, the abovementioned techniques will be employed to establish the integrity of the proposed models and solution scheme. For that, first the stress-strain response of the neat resin will be predicted. That will be

TABLE 1: Calculated rate-dependent material constants of WS-105 epoxy resin.

Material	Strain rate (s^{-1})	Tangential modulus (GPa)	Poisson's ratio	D_0 (s^{-1})	n	Z_0 (MPa)	Z_1 (MPa)	q	α_0	α_1
WS-105 epoxy	1×10^{-3}	3.1	0.3	5×10^6	0.745	200	1130	610	0.202	0.430
	1×10^{-2}									
	1×10^{-1}									
	1									

followed by a parametric study that will assess the strain-rate effects on the nanoparticle-reinforced epoxy resin. To calculate the stress-strain of nanoparticle-reinforced polymer composite, first the global stress-strain curve of the neat resin is predicted using the Goldberg model [22–24]. Then, the tensile tangent moduli of the pure polymer in appropriate strain intervals are determined, sequentially. Subsequently, the tangent moduli of the nanoparticle-reinforced resin are evaluated at each strain interval by modifying the obtained tangential moduli of the pure polymer using the Halpin-Tsai equation. As a result, the stress corresponding to each strain interval can be determined for the nanoparticle-reinforced resin. Finally, after establishing the stress values, one would be able to establish the global stress-strain curve.

4. Results and Discussion

In this section, we discuss the integrity and accuracy of the developed SRDM model introduced in Section 3, for predicting the tensile stress-strain response of the neat epoxy resin reinforced with various nanoparticles. For that, first by following the steps noted in Section 3 and those in Appendix, the stability of the iterative R-K-4 numerical procedure for establishing the tensile stress-strain response of the neat resin under an arbitrary strain rate is tested, with the results illustrated in Figure 4. As can be seen, three different time steps, dt , were selected for this task.

As seen and anticipated, smoother and more continuous curves are obtained as the value of time step is decreased, and the numerical convergence is clearly evident. To establish the rate-dependent material constants, the experimental results of the tensile tests conducted under quasistatic loading rate of 150 mm/min ($= 10^{-1} s^{-1}$) are used. It should be noted that, by knowing the initial gauge length (i.e., 25.4 mm), one can easily convert the loading rates into strain rates. The rate-dependent material properties of the neat epoxy are provided in Table 1.

Due to the nonlinear behavior of nanoparticle-reinforced polymer composites, the value of the constant linear modulus should be replaced by the tangential modulus. To establish the strain rate-dependent response of the resin reinforced with different nanoparticles and their resulting response to different strain rates, first the instantaneous tangential modulus of the neat resin under quasistatic strain rate ($10^{-1} s^{-1}$) is established. Figure 5 illustrates the variation of the tangential modulus of the neat resin.

Subsequently, having established neat resin's stress-strain response, the SRDM micromechanical model is used to

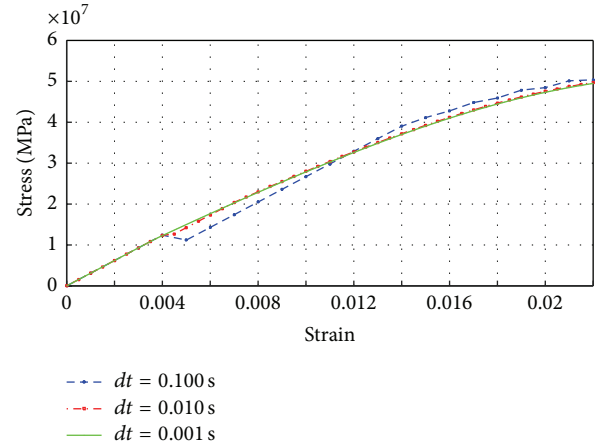


FIGURE 4: Influence of the time steps (dt) on the numerical stability of the adopted iterative procedure used for predicting the stress-strain curves of the neat WS-105 epoxy resin at an arbitrary strain rate.

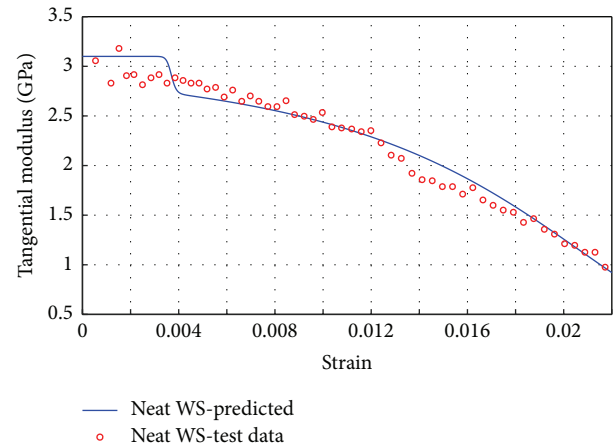


FIGURE 5: Variation of the tangential modulus of WS-105 neat epoxy resin, as a function of strain when the material loaded under quasistatic strain rate of $10^{-1} s^{-1}$.

establish the tensile stress-strain response of the resin reinforced with various weight contents (wt%) of the three nanoparticle types, subjected to different strain rates. The predicted responses are then compared to the experimental results.

Figure 6 shows comparison of the predicted and experimental stress-strain curves. Figure 6(a) illustrates the variation in stress-strain response as a function of nanoparticles type under quasistatic strain rate of $10^{-3} s^{-1}$. Figure 6(b)

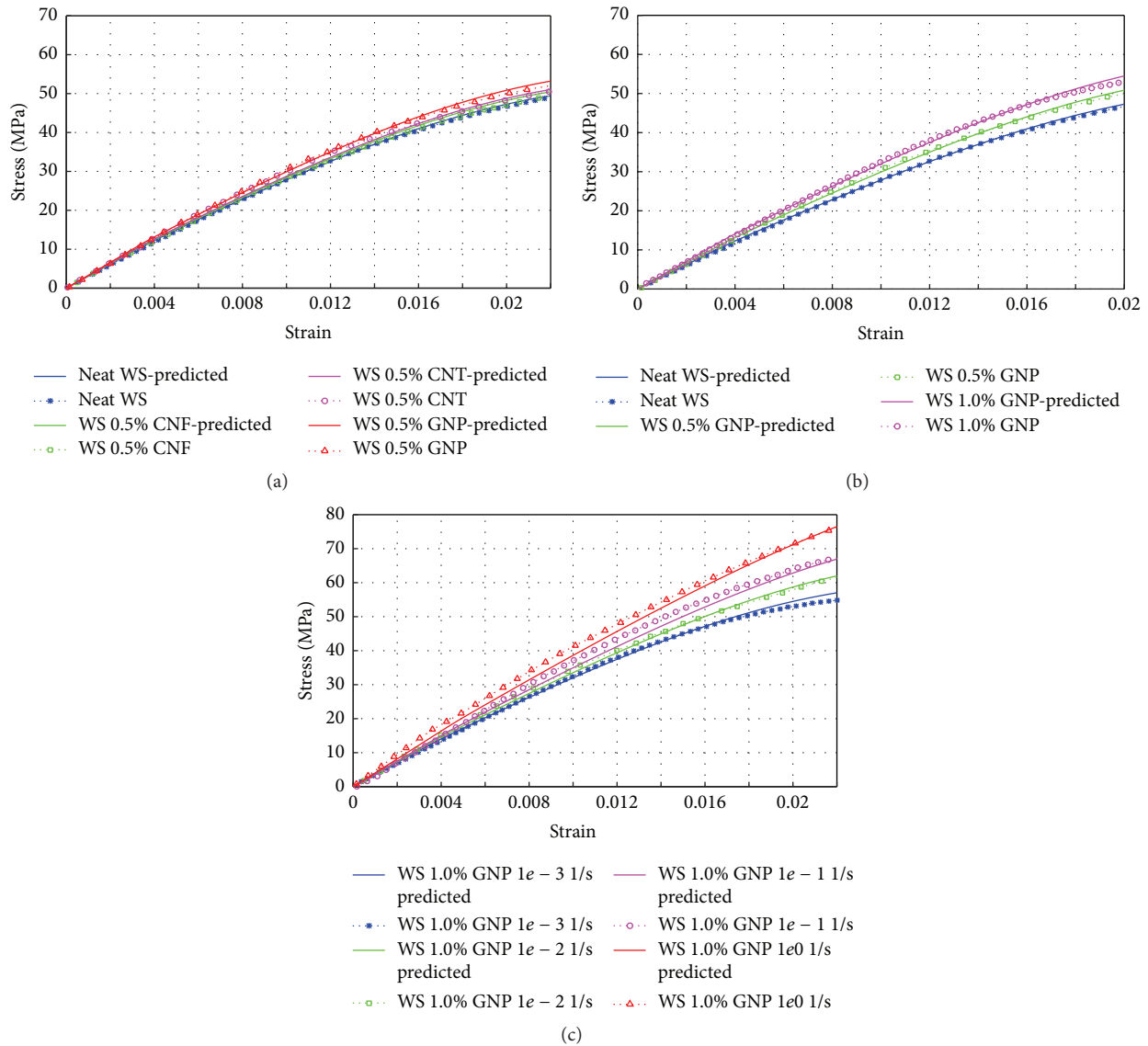


FIGURE 6: Comparison of the predicted and experimental stress-strain curves of WS-105 resins reinforced with various types of nanoparticles: (a) influence of nanoparticles type; (b) influence of GNP's weight content when the resin is subjected to a quasistatic strain rate of 10^{-3} s^{-1} ; (c) influence of strain rate on the stress-strain responses of the resin reinforced with 1 wt% GNP.

shows the influence of GNP weight content on the predicted stress-strain responses, loaded at a quasistatic strain rate of 10^{-3} s^{-1} . Finally, Figure 6(c) illustrates the influence of the different strain rates on the predicted stress-strain responses of the resin reinforced with 1 wt% GNP. It can be seen from the results illustrated in Figure 6 that, in all cases, the predicted values are in good agreement with the experimental results.

As seen from the results shown in Figure 6(b), the inclusion of the GNPs produced the most optimum enhancement of the mechanical response of the resin. Moreover, among the weight contents considered for the inclusion of GNPs in this study, 1 wt% was found to produce the most optimum mechanical response, regardless of the applied strain rates. It was also demonstrated that both the strength and stiffness of the nanoparticle-reinforced resin were increased as the strain rate was increased.

5. Conclusion

This study demonstrated that the combination of a strain rate-dependent mechanical (SRDM) model (in this case, the Goldberg et al. model) and a micromechanical model (in this case, the Halpin-Tsai model) could predict the stress-strain response of neat and nanoparticle-reinforced epoxy resins with good accuracy. The predicted results also revealed that the response of the resin was improved when it was reinforced with the relatively inexpensive type nanocarbon particles (i.e., GNPs), in comparison to the more expensive CNTs. It was also demonstrated that the increase in strain rate resulted in higher apparent strength and stiffness of nanoparticle-reinforced resin. Comparatively, this increase was even more significant than the enhancement obtained by inclusion of the nanocarbon particles. Moreover, the enhancement in resin's

stiffness was observed to be more significant compared to the gain in its strength.

As noted, inclusion of GNP into the neat resin improved the stiffness of the adhesive, resulting in enhancement of the elastic modulus by 11% and 21% for the resin reinforced 0.5 wt% GNPs, evaluated at the lowest and highest strain rates, respectively. Furthermore, based on the obtained results, one can conclude that the higher weight percentage (i.e., 1 wt% GNP) resulted in the highest stiffness. It was also observed that reinforced resin's modulus of elasticity was enhanced by 19% and 33% when the resin was reinforced with 1 wt% GNPs and when the material was tested under the lowest and highest loading rates, respectively.

Finally, comparison of the results obtained for the resin reinforced with 0.5 wt% of GNP and that reinforced with 0.5 wt% of CNF, subjected to the quasistatic strain rate, revealed that inclusion of the GNP produced a greater average ultimate tensile strength and modulus of elasticity than inclusion of CNF could.

Appendix

Details of the Runge-Kutta Procedure

The second step of the R-K-4 using the results of the first step takes the following form:

$$\begin{aligned}
 d\varepsilon_{ij}^{I(\text{step}2)} &= d\varepsilon_{ij}^I, \\
 dZ^{(\text{step}2)} &= dZ, \\
 d\alpha^{(\text{step}2)} &= d\alpha, \\
 \varepsilon_{ij}^I &= \varepsilon_{ij}^{I(n)} + \frac{1}{2}d\varepsilon_{ij}^{I(\text{step}2)}, \\
 \{\sigma\} &= [C_m] \left(\{\varepsilon\}^{n+1} - \{\varepsilon\}^I \right), \\
 Z &= Z^{m(n)} + \frac{1}{2}dZ^{(\text{step}2)}, \\
 \alpha &= \alpha^{m(n)} + \frac{1}{2}d\alpha^{(\text{step}2)}.
 \end{aligned} \tag{A.1}$$

And the 3rd step can be obtained using the results of the 2nd step:

$$\begin{aligned}
 d\varepsilon_{ij}^{I(\text{step}3)} &= d\varepsilon_{ij}^I, \\
 dZ^{(\text{step}3)} &= dZ, \\
 d\alpha^{(\text{step}3)} &= d\alpha, \\
 \varepsilon_{ij}^I &= \varepsilon_{ij}^{I(n)} + \frac{1}{2}d\varepsilon_{ij}^{I(\text{step}3)}, \\
 \{\sigma\} &= [C_m] \left(\{\varepsilon\}^{n+1} - \{\varepsilon\}^I \right), \\
 Z &= Z^{m(n)} + \frac{1}{2}dZ^{(\text{step}3)}, \\
 \alpha &= \alpha^{m(n)} + \frac{1}{2}d\alpha^{(\text{step}3)}.
 \end{aligned} \tag{A.2}$$

Similar to the previous steps, results of the third step are used in the final step:

$$\begin{aligned}
 d\varepsilon_{ij}^{I(\text{step}4)} &= d\varepsilon_{ij}^I, \\
 dZ^{(\text{step}4)} &= dZ, \\
 d\alpha^{(\text{step}4)} &= d\alpha.
 \end{aligned} \tag{A.3}$$

Then, the magnitude of stress and inelastic strain in the next time step can be calculated through the final step of the Runge-Kutta method as follows:

$$\begin{aligned}
 \varepsilon_{ij}^{I(n+1)} &= \varepsilon_{ij}^{I(n)} + \frac{1}{6}d\varepsilon_{ij}^{I(\text{step}1)} + \frac{1}{3}d\varepsilon_{ij}^{I(\text{step}2)} \\
 &\quad + \frac{1}{3}d\varepsilon_{ij}^{I(\text{step}3)} + \frac{1}{6}d\varepsilon_{ij}^{I(\text{step}4)}, \\
 \{\sigma\}^{m(n+1)} &= [C_m] \left(\{\varepsilon\}^{n+1} - \{\varepsilon\}^{I(n+1)} \right), \\
 Z^{m(n+1)} &= Z^{m(n)} + \frac{1}{6}dZ^{(\text{step}1)} + \frac{1}{3}dZ^{(\text{step}2)} \\
 &\quad + \frac{1}{3}dZ^{(\text{step}3)} + \frac{1}{6}dZ^{(\text{step}4)}, \\
 \alpha^{m(n+1)} &= \alpha^{m(n)} + \frac{1}{6}d\alpha^{(\text{step}1)} + \frac{1}{3}d\alpha^{(\text{step}2)} \\
 &\quad + \frac{1}{3}d\alpha^{(\text{step}3)} + \frac{1}{6}d\alpha^{(\text{step}4)}.
 \end{aligned} \tag{A.4}$$

Finally, the tensile stress-strain curve of the neat polymer under an arbitrary strain rate can be obtained accordingly.

Conflict of Interests

The authors declare that there is no conflict of interests regarding the publication of this paper.

Acknowledgments

The Natural Science and Engineering Research Council of Canada's financial support for this research work is gratefully acknowledged and appreciated.

References

- [1] M. R. Loos and K. Schulte, "Is it worth the effort to reinforce polymers with carbon nanotubes?" *Macromolecular Theory and Simulations*, vol. 20, no. 5, pp. 350–362, 2011.
- [2] O. Breuer and U. Sundararaj, "Big returns from small fibers: a review of polymer/carbon nanotube composites," *Polymer Composites*, vol. 25, no. 6, pp. 630–645, 2004.
- [3] G. Choudalakis and A. D. Gotsis, "Permeability of polymer/clay nanocomposites: a review," *European Polymer Journal*, vol. 45, no. 4, pp. 967–984, 2009.
- [4] J.-J. Luo and I. M. Daniel, "Characterization and modeling of mechanical behavior of polymer/clay nanocomposites," *Composites Science and Technology*, vol. 63, no. 11, pp. 1607–1616, 2003.

- [5] P.-G. Ren, D.-X. Yan, T. Chen, B.-Q. Zeng, and Z.-M. Li, "Improved properties of highly oriented graphene/polymer nanocomposites," *Journal of Applied Polymer Science*, vol. 121, no. 6, pp. 3167–3174, 2011.
- [6] T. D. Fornes and D. R. Paul, "Modeling properties of nylon 6/clay nanocomposites using composite theories," *Polymer*, vol. 44, no. 17, pp. 4993–5013, 2003.
- [7] D. Datashvili and H. Baier, "Membranes and thin shells for space reflectors," in *Proceedings of the Earth & Space*, pp. 1–8, Chicago, Ill, USA, 2006.
- [8] J.-K. Lee, "Prediction of thermal conductivity of composites with spherical fillers by successive embedding," *Archive of Applied Mechanics*, vol. 77, no. 7, pp. 453–460, 2007.
- [9] M. A. Rafiee, J. Rafiee, Z. Wang, H. Song, Z.-Z. Yu, and N. Koratkar, "Enhanced mechanical properties of nanocomposites at low graphene content," *ACS Nano*, vol. 3, no. 12, pp. 3884–3890, 2009.
- [10] J. Rotrekl, L. Matějka, L. Kaprálková, A. Zhigunov, J. Hromádková, and I. Kelnar, "Epoxy/PCL nanocomposites: effect of layered silicate on structure and behavior," *Express Polymer Letters*, vol. 6, no. 12, pp. 975–986, 2012.
- [11] S. Shadlou, B. Ahmadi-Moghadam, and F. Taheri, "Nano-enhanced adhesives," *Reviews of Adhesion and Adhesives*, vol. 2, no. 3, pp. 371–412, 2014.
- [12] S. Iijima, "Helical microtubules of graphitic carbon," *Nature*, vol. 354, no. 6348, pp. 56–58, 1991.
- [13] S. Iijima and T. Ichihashi, "Single-shell carbon nanotubes of 1-nm diameter," *Nature*, vol. 363, no. 6430, pp. 603–605, 1993.
- [14] R. Saito, G. Dresselhaus, and M. S. Dresselhaus, *Physical Properties of Carbon Nanotubes*, Imperial College Press, London, UK, 1998.
- [15] B. G. Demczyk, Y. M. Wang, J. Cumings et al., "Direct mechanical measurement of the tensile strength and elastic modulus of multiwalled carbon nanotubes," *Materials Science and Engineering: A*, vol. 334, no. 1-2, pp. 173–178, 2002.
- [16] M. Alexandre and P. Dubois, "Polymer-layered silicate nanocomposites: preparation, properties and uses of a new class of materials," *Materials Science and Engineering R: Reports*, vol. 28, no. 1-2, pp. 1–63, 2000.
- [17] J.-S. Kim and D. H. Reneker, "Mechanical properties of composites using ultrafine electrospun fibers," *Polymer Composites*, vol. 20, no. 1, pp. 124–131, 1999.
- [18] V. K. Srivastava and P. J. Hogg, "Moisture effects on the toughness, mode-I and mode-II of particles filled quasi-isotropic glass-fibre reinforced polyester resin composites," *Journal of Materials Science*, vol. 33, no. 5, pp. 1129–1136, 1998.
- [19] D. Qian, E. C. Dickey, R. Andrews, and T. Rantell, "Load transfer and deformation mechanisms in carbon nanotube-polystyrene composites," *Applied Physics Letters*, vol. 76, no. 20, pp. 2868–2870, 2000.
- [20] R. A. Schapery, "Nonlinear viscoelastic and viscoplastic constitutive equations based on thermodynamics," *Mechanics Time-Dependent Materials*, vol. 1, no. 2, pp. 209–240, 1997.
- [21] A. Plaseied and A. Fatemi, "Deformation response and constitutive modeling of vinyl ester polymer including strain rate and temperature effects," *Journal of Materials Science*, vol. 43, no. 4, pp. 1191–1199, 2008.
- [22] R. K. Goldberg, G. D. Roberts, and A. Gilat, "Implementation of an associative flow rule including hydrostatic stress effects into the high-strain rate deformation analysis of polymer matrix composites," *Journal of Aerospace Engineering*, vol. 18, no. 1, pp. 18–27, 2005.
- [23] R. K. Goldberg and D. C. Stouffer, "Strain rate dependent analysis of a polymer matrix composite utilizing a micromechanics approach," *Journal of Composite Materials*, vol. 36, no. 7, pp. 773–793, 2002.
- [24] A. Gilat, R. K. Goldberg, and G. D. Roberts, "Strain rate sensitivity of epoxy resin in tensile and shear loading," *Journal of Aerospace Engineering*, vol. 20, no. 2, pp. 75–89, 2007.
- [25] O. A. Hasan and M. C. Boyce, "Constitutive model for the nonlinear viscoelastic viscoplastic behavior of glassy polymers," *Polymer Engineering and Science*, vol. 35, no. 4, pp. 331–344, 1995.
- [26] S. P. Bao and S. C. Tjong, "Mechanical behaviors of polypropylene/carbon nanotube nanocomposites: the effects of loading rate and temperature," *Materials Science and Engineering A*, vol. 485, no. 1-2, pp. 508–516, 2008.
- [27] J. Ingram, Y. Zhou, S. Jeelani, T. Lacy, and M. F. Horstemeyer, "Effect of strain rate on tensile behavior of polypropylene and carbon nanofiber filled polypropylene," *Materials Science and Engineering: A*, vol. 489, no. 1-2, pp. 99–106, 2008.
- [28] S. Peter and E. Woldesenbet, "Nanoclay syntactic foam composites-high strain rate properties," *Materials Science and Engineering A*, vol. 494, no. 1-2, pp. 179–187, 2008.
- [29] M. M. Shokrieh, R. Mosalmani, and M. J. Omid, "Strain rate dependent micromechanical modeling of reinforced polymers with carbon nanotubes," *Journal of Composite Materials*, vol. 48, no. 27, pp. 3381–3393, 2014.
- [30] J. C. Halpin and J. L. Kardos, "The Halpin-Tsai equations: a review," *Polymer Engineering and Science*, vol. 16, no. 5, pp. 344–352, 1976.
- [31] B. Soltannia and F. Taheri, "Static, quasi-static and high loading rate effects on graphene nano-reinforced adhesively bonded single-lap joints," *International Journal of Composite Materials*, vol. 3, pp. 181–190, 2013.
- [32] B. Soltannia and F. Taheri, "Influence of nano-reinforcement on the mechanical behavior of adhesively bonded single-lap joints subjected to static, quasi-static, and impact loading," *Journal of Adhesion Science and Technology*, vol. 29, no. 5, pp. 424–442, 2015.
- [33] ASTM International, "Standard test method for tensile properties of plastics," ASTM D638, ASTM International, West Conshohocken, Pa, USA, 2012.
- [34] ASTM International, "Test method for tensile properties of adhesive bonds," ASTM D897, ASTM International, West Conshohocken, Pa, USA, 2012.
- [35] ASTM International, "Test method for impact strength of adhesive bonds," ASTM D950, ASTM International, West Conshohocken, Pa, USA, 2012.
- [36] A. Tabiei and I. Ivanov, "Micro-mechanical model with strain-rate dependency and damage for impact simulation of woven fabric composites," *Mechanics of Advanced Materials and Structures*, vol. 14, no. 5, pp. 365–377, 2007.
- [37] A. Tabiei and S. B. Aminjikai, "A strain-rate dependent micro-mechanical model with progressive post-failure behavior for predicting impact response of unidirectional composite laminates," *Composite Structures*, vol. 88, no. 1, pp. 65–82, 2009.

Review Article

An Overview on the Improvement of Mechanical Properties of Ceramics Nanocomposites

J. Silvestre,¹ N. Silvestre,² and J. de Brito¹

¹CERis-ICIST, Department of Civil Engineering, Architecture and Georesources, Instituto Superior Técnico, Universidade de Lisboa, Av. Rovisco Pais, 1049-001 Lisbon, Portugal

²LAETA, IDMEC, Department of Mechanical Engineering, Instituto Superior Técnico, Universidade de Lisboa, Av. Rovisco Pais, 1049-001 Lisbon, Portugal

Correspondence should be addressed to N. Silvestre; nsilvestre@ist.utl.pt

Received 4 September 2015; Accepted 24 November 2015

Academic Editor: Konstantinos I. Tserpes

Copyright © 2015 J. Silvestre et al. This is an open access article distributed under the Creative Commons Attribution License, which permits unrestricted use, distribution, and reproduction in any medium, provided the original work is properly cited.

Due to their prominent properties (mechanical, stiffness, strength, thermal stability), ceramic composite materials (CMC) have been widely applied in automotive, industrial and aerospace engineering, as well as in biomedical and electronic devices. Because monolithic ceramics exhibit brittle behaviour and low electrical conductivity, CMCs have been greatly improved in the last decade. CMCs are produced from ceramic fibres embedded in a ceramic matrix, for which several ceramic materials (oxide or non-oxide) are used for the fibres and the matrix. Due to the large diversity of available fibres, the properties of CMCs can be adapted to achieve structural targets. They are especially valuable for structural components with demanding mechanical and thermal requirements. However, with the advent of nanoparticles in this century, the research interests in CMCs are now changing from classical reinforcement (e.g., microscale fibres) to new types of reinforcement at nanoscale. This review paper presents the current state of knowledge on processing and mechanical properties of a new generation of CMCs: Ceramics Nanocomposites (CNCs).

1. Introduction

It is widely recognised that ceramic matrix composites (CMCs) are extremely valuable materials for applications with demanding mechanical and thermal requirements. Despite the fact that ceramic matrices often present brittle behaviour, CMCs have been developed to achieve quasi-ductile fracture behaviour and maintain all other advantages of monolithic ceramics at high temperatures. For instance, CMCs can be fabricated as strong as metals, but they are much lighter and can withstand much higher temperatures. These advantages led to their application in automotive and aerospace engineering (components and aircraft engine platforms; see Figure 1).

On the opposite side, there are many ceramic products in construction industry, like floor, wall and roofing tiles, cement, or bricks, but the level of sophistication of these products is still low. Due to the large scale and multibillion dollar industry, it is expected that construction and associated

manufacturing companies will invest in CMCs for building and structural components.

There are many different types of CMCs. The classification is usually done according to the matrix and fibre materials, separated by a slash. For example, C/SiC is a ceramic matrix composite made of carbon fibres and a silicon carbide matrix. Besides these types of matrices and fibre materials, the classification usually separates ceramic matrix composites in oxide and nonoxide composites. Table 1 shows the main materials used as ceramic matrix composites according to that classification. As shown in the examples, oxide fibres are usually combined with oxide matrices and nonoxide fibres with nonoxide matrices. Thus, the main CMC types are C/C, C/SiC, SiC/SiC, and O_x/O_x, where O_x represents one of the oxide materials presented in Table 1.

When nanotechnology was introduced in the production of CMCs and analysis went from micro to nanoscale (composites to nanocomposites), some of the previously existing



FIGURE 1: Oxide ceramic matrix composites exhaust ground test demonstrator consisting of a 1.60 m diameter nozzle (showing underneath the titanium-alloy faring) and 1.14 m diameter by 2.34 m conical centerbody with titanium end cap inspection portal (Courtesy of Wiley, Steyer [1]).

TABLE 1: Brief overview of CMCs reported in the literature.

Ceramic matrix composites	Materials	References	
Matrix	Nonoxide	Silicon carbide	[2, 3]
		Carbon	[4]
		Alumina	[5, 6]
	Oxide	Zirconia	[7]
		Mullite	[8]
		Aluminosilicates	[9]
Fibres	Nonoxide	Carbon	[10]
		Silicon carbide	[11–13]
		Alumina	[8]
		Mullite	[14]
		Zirconia	[15]

materials lost impact and others arose. For example, the introduction of CNTs [16, 17] and graphene nanosheets [18, 19] in CMCs led to great interest of the research community due to the outstanding inherent mechanical, thermal, and electrical properties of these materials. Authors reported remarkable improvements in properties like hardness, toughness, strength, damping, and thermal conductivity over monolithic ceramics by using these types of fillers. For example, in the case of alumina CMCs, Fan et al. [20] reported an improvement of approximately 100% in fracture toughness and 20% in flexural strength with the addition of only 1 wt% single-walled carbon nanotubes (SWCNTs). Moreover, Walker et al. [21] reported an increase of approximately 235% (from ~2.8 to ~6.6 MPa) at ~1.5% graphene platelets volume fraction.

As concluded from these preliminary remarks, the topic of Ceramics Nanocomposites (CNCs) is growing fast and the next years will demonstrate the need for a continuous and updated review on this theme. The objective of this paper is to bring to the scientific community a state-of-the-art review on the main developments and trends in CNCs. From the search carried out in scientific databases, this review is focused

on the most effective strengthening nanoparticles and the corresponding CNCs, which are

- (i) silica carbide (SiC);
- (ii) zirconia;
- (iii) carbon nanotubes (CNTs);
- (iv) graphene.

2. SiC-Based CNCs

Silicon carbide (SiC) is one of the most promising structural materials due to its superior thermomechanical properties, such as high chemical and thermal stability, good chemical inertness, high thermal conductivity, high hardness, low density, and low coefficient of thermal expansion [22]. Silicon carbide is a compound of silicon and carbon with chemical formula SiC. It occurs in nature as mineral moissanite. Because of the rarity of natural moissanite, most silicon carbides are synthetic. SiC is part of a family of materials that exhibit a one-dimensional polymorphism called polytypism. Thanks to its structure, an almost infinite number of SiC polytypes are possible, and more than 200 have already been discovered [23]. With the introduction of nanotechnology and manipulation at nanoscale, new opportunities have been opened. One-dimensional (1D) nanostructures such as nanowires or nanotubes have gained much interest in fundamental research as well as tremendous potential applications. Among many materials, SiC-based 1D nanostructures have very interesting physical, chemical, and electronic properties. SiC is a wide band gap semiconductor, from 2.2 eV to 3.4 eV depending on the polytype with a high electronic mobility and thermal conductivity. One of the other merits of SiC is that it can be used at high temperatures because its noncongruent melting point reaches 3100°K and its maximal operating temperature is considered to be 1200°K [24]. Moreover, SiC is resistant to corrosive environments because of its chemical inertness. These facts justify the high application of SiC in a wide range of areas, such as electronics, heating elements, and structural materials. More particularly, SiC nanoparticles have been introduced in CMCs to enhance the mechanical and thermal properties of ceramic materials such as Al₂O₃ and mullite. The purpose now is to present some examples of the main improvements achieved with these nanoadditions in ceramic materials and to evaluate how these improvements can be incorporated in ceramic products used in construction industry.

In terms of thermal behaviour and electrical conductivity, Parchovianský et al. [25] studied the influence of SiC nanoparticles additions on the electrical and thermal conductivity of Al₂O₃/SiC micro-/nanocomposites under normal and high temperatures. Different samples with various volume fraction of SiC ranging from 3 vol% to 20 vol% were prepared by hot pressing at 1740°C and at 30 MPa pressure in an argon atmosphere. The results showed that the thermal properties (thermal diffusivity and thermal conductivity) of Al₂O₃/SiC nanocomposites were not influenced by the size and shape of SiC particles but by the volume content of these particles. Thermal conductivity increased with higher contents of SiC nanoparticles up to a maximum

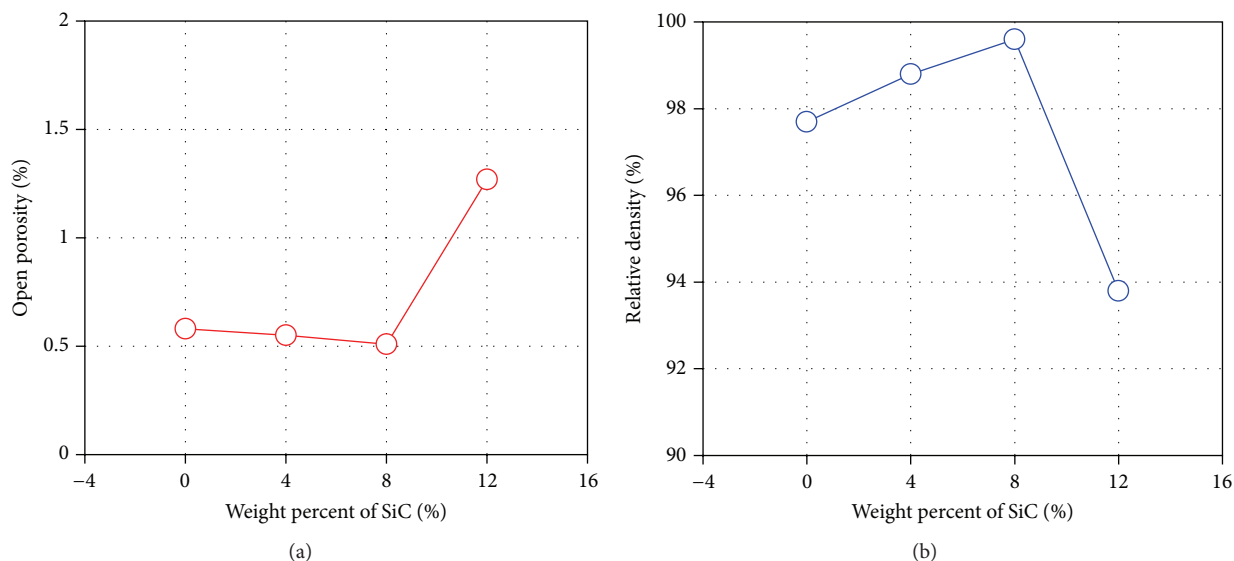


FIGURE 2: (a) Open porosity and (b) relative density of SiC-AlON composites measured via the Archimedes principle *versus* amount of SiC particles [22].

of 35% increase (from 28 W/m K to 38 W/m K) for 20 vol% of these nanoparticles. Barea et al. [26] obtained similar trends for these properties. However, if compared with the theoretical values of thermal conductivity reported for SiC (700 W/m K) or the value measured for a polycrystalline hot pressed SiC (270 W/m K), the resulting thermal conductivity of a composite with 20 vol% of SiC should be much higher. Hasselman and Johnson [27] stated that the existence of a thermal barrier resulted from unperfected thermal contacts at the matrix/dispersion interfaces, partially explained by the difference of thermal expansion coefficients of the two phases. Still, a relevant increase was achieved with the inclusion of SiC nanoparticles. Regarding electrical conductivity, Parchovianský et al. [25] also showed that the electrical conductivity increased with higher amounts of SiC nanoparticles, especially in the composites with the volume fraction of SiC higher, or equal to 10 vol%. The results indicated that at low SiC contents the SiC particles were not interconnected to form a continuous conductive network which was verified for amounts higher than 10%, when an increase from 10^{-5} S/m (for 5 vol%) to 10^{-3} S/m (for 10 vol%) was recorded. Other studies testified identical trends, such as those of Sawaguchi et al. [28] or Stauffer and Aharony [29] that, based on mathematical models, proposed a value of 17 vol% of addition of a secondary phase to create an effective conductive path.

Regarding the mechanical properties of SiC ceramic nanocomposites, Zhao et al. [22] investigated processing and mechanical behaviour of SiC, aluminium oxynitride (AlON) nanocomposites. AlON is widely used as ceramic material due to its high stiffness, good chemical stability and superior corrosion and wear resistances. However, its low flexural strength and poor fracture toughness justify the incorporation of nanoadditions in the production of these types of CNCs. In this study, four samples were tested with 0 wt%, 4 wt%, 8 wt%, and 12 wt% contents of SiC. The results showed interesting indicators. Concerning microstructure

and density, the authors reported a decrease in the number of visible pores with the addition of SiC up a maximum reduction for 8 wt% SiC sample. For 12 wt%, an increase in the number of pores was observed, in accordance with similar works such as Dong et al. [30], where a decrease in relative density was registered for higher contents of SiC (more than 10 wt%). Complementarily, a similar trend was observed for open porosity and relative porosity as shown in Figure 2.

Figure 2 shows that the open porosity decreased with the increasing content of SiC nanoparticles up to 8 wt% and then increased with additional SiC up to 12 wt%. Accordingly, the relative density showed an opposite trend. The authors proposed some explanations for these facts, namely, the agglomeration of SiC nanoparticles in these composites for higher addition amounts. Moreover, Djenkal et al. [31] also reported that additional amounts of SiC would bring a sintering inhibiting effect on the ceramic matrix, due to the strong covalent nature of Si-C bond, which makes it harder to fabricate self-bonded SiC ceramics below 2100°C [32].

Regarding the mechanical properties, the microhardness and Young's modulus of SiC-AlON composites were also evaluated. Figures 3(a) and 3(b) show that both microhardness and Young's modulus increased with increasing the addition of SiC nanoparticles up to 8 wt% and then significantly decreased for 12 wt%, showing a direct relationship between mechanical properties and microstructure (density) of SiC-AlON nanocomposites. Moreover, Smirnov and Bartolomé [33] also reported that the presence of porosity generally has a negative influence on the mechanical properties, due to the concentration of stress in pores, resulting in lower strength. In addition, the authors registered similar results for flexural strength and fracture toughness. The flexural and fracture toughness were 35% and 24% higher in comparison to pure AlON for an optimum content of 8 wt% addition. From these results, two main ideas should be emphasized from the use of SiC nanoparticles: (i) almost all properties of monolithic

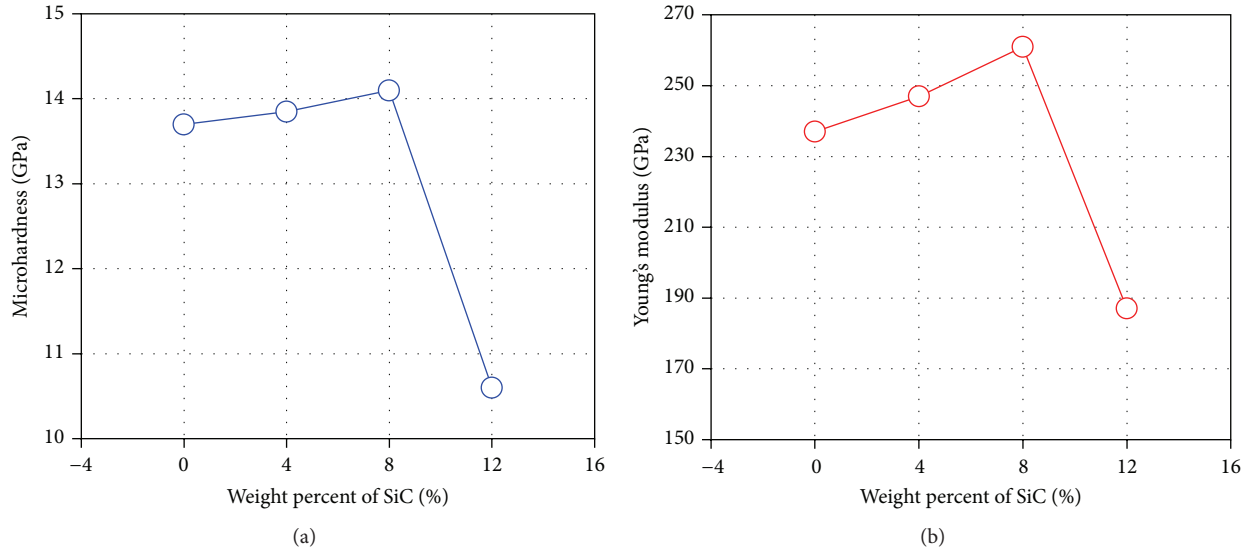


FIGURE 3: (a) Microhardness and (b) Young's modulus as a function of the content of SiC particles in SiC-ALON composites [22].

ceramics are enhanced, such as the thermal, mechanical, and electrical ones as well as the microstructure, but an optimum value of 8–10 wt% SiC is proposed to maximize the increase in mechanical properties and (ii) the thermal properties of ceramics with SiC particles improved with increasing SiC addition content.

According to the specific functions intended for these types of materials, a reasonable value (not higher than 10–15 wt%) should be considered, in order to reconcile these two goals (optimization of strength versus maximization of thermal conductivity). Contrary to other nanomaterials, the dispersion of these SiC nanoparticles into a cement matrix does not seem to be a critical issue for the scientific community, justifying the high application of SiC in ceramics materials. For example, the CoorsTek Company [34] developed ceramic products with the application of SiC powders. The producers present, as key benefits and properties of SiC ceramics, their high thermal conductivity, low thermal expansion coefficient, extreme hardness, and chemical attack resistance, making of SiC a nanomaterial with high potential for reinforced ceramics materials.

3. Zirconia-Based CNCs

Like SiC, zirconia (ZrO_2) is a specific material with high potential to be used in ceramic materials, due to its high ionic and thermal conductivity, in addition to mechanical properties. ZrO_2 is a white crystalline oxide of zirconium. It can occur naturally or synthesized in three main phases: monoclinic, tetragonal, and cubic. In addition, zirconia is chemically unreactive. Under higher temperatures, ZrO_2 adopts a tetragonal and cubic structure. ZrO_2 particles are used as one of the most common fillers, leading to an increase in fracture toughness and chemical inertness. Recent studies suggest that the mechanical properties of CNCs with ZrO_2 could be considerably increased by reducing the level of grain size and by achieving high levels of dispersion of these

particles in the matrix. Zirconia and alumina are very often associated [35]. Zirconia Toughened Alumina (ZTA) ceramics offer an improved performance for an exceptional cost ratio. ZTA nanocomposites are attractive structural materials that combine the high hardness and Young's modulus of the alumina matrix with an additional toughening effect of the zirconia dispersion. ZTA ceramics are produced to contain 2–20 vol% of fine zirconia particles in an alumina matrix, with increased strength and toughness. For example, Chinelatto et al. [36] studied the effect of sintering curves on the microstructure of alumina-zirconia CNCs. The purpose of sintering advanced composites is to control the material's final microstructure with high densification with low grain growth and elimination of porosity. Different samples with 5 vol% of nanometric ZrO_2 inclusions in an alumina matrix were tested. The results showed an important influence of the temperature on the grain size and growth. An increase of approximately 2.5 times (from 1000 nm to 2500 nm) was observed in the mean grain size with two distinct sintering procedures: 1500°C and 1600°C, respectively. These results have important consequences on the mechanical properties of CNCs that are summarized next. Most studies focus the toughening mechanisms in CNCs. For example, Benavente et al. [35] registered an increase from 5 $\text{MPa m}^{1/2}$ to approximately 6 $\text{MPa m}^{1/2}$ in the fracture toughness for samples with 15 vol% ZrO_2 in alumina matrix for a sintering temperature of 1200°C and 1400°C, respectively. Complementarily, as Figure 4 shows, a significant increase in hardness and Young's modulus was registered (from 9 GPa to 20 GPa and from 300 GPa to 367 GPa, resp.) for samples with 10 vol% of ZrO_2 .

Zirconia can also be used as the matrix and alumina as the addition. For example, Vasylykiv et al. [15] produced zirconia ceramic with 1 wt% to 5 wt% Al_2O_3 addition. The authors obtained an average hardness and toughness for 2.5 wt% alumina addition of 16.23 GPa and 7.86 $\text{MPa m}^{1/2}$, respectively. Zirconia can also play an important role as a ceramic matrix

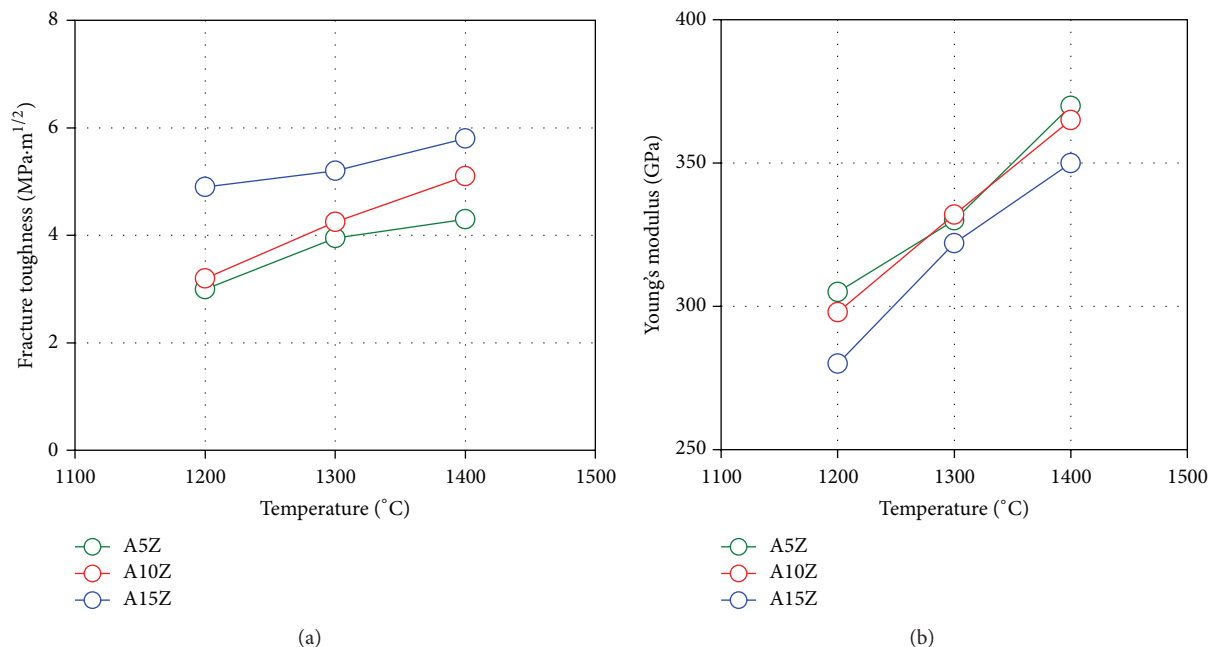


FIGURE 4: Influence of microwave sintering temperature on (a) fracture toughness and (b) Young's modulus of Al₂O₃-ZrO₂ materials with different contents [35].

material. Danilenko et al. [37] studied the effect of nickel oxide (NiO) in ZrO₂ composites. The authors registered that NiO and inclusions can increase the indentation fracture toughness of zirconia-nickel oxide composite material more than 50%, but only when the sintering occurs in a neutral atmosphere.

In this context, the CoorsTek Company [38] also developed a zirconia ceramic product named Technox zirconia [39] for application in several industries, such as refractories, telecommunications, or electronics with the following advantages: high strength, high fracture toughness, high wear resistance, good frictional behaviour, low thermal conductivity, and electrical insulation. Still, as observed for silicon carbide, if improved electrical properties are needed, other nanomaterials are more suitable, such as carbon nanotubes or graphene oxide.

4. CNT-Based CNCs

The excellent properties of carbon nanotubes (CNTs) together with their one-dimensional nature (high aspect ratio) dimensionality make them ideal candidates for reinforcement in almost any type of materials. CNCs are naturally included in these areas, where CNTs can be used as toughening elements to overcome the intrinsic brittleness of the ceramic materials. Thanks to their structure, CNTs tend to form complex networks of aggregates within composite materials, playing a major role in defining the mechanical, electrical, and thermal properties of the composites [40]. The majority of works addressing CNT composites were focused on polymer matrices, whilst comparatively few investigations explored inorganic (ceramic) matrices and the potential of CNTs reinforcements as toughening mechanisms. However,

the increasing interest on CNTs applications and fabrication with lower cost maintain the potential of this issue. For example, Cho et al. [40] presented an extended overview on CNCs containing CNTs. According to the authors, for successful CNT/composite development, two major challenges must be considered. Primarily, CNTs with intrinsically good mechanical properties must be obtained in reasonable quantity at acceptable cost for consistent incorporation in materials production industry. Secondly, CNTs must be processed in such a way that a homogeneous dispersion is obtained within the matrix with an appropriate degree of interfacial bonding.

These requirements are naturally common to all CNT composites, but, in the case of inorganic matrix composites, such as ceramics, they play a key role in the production of CNCs with CNTs. In the case of CNCs, obtaining a high degree of inorganic matrix densification without damaging the CNTs is a widely discussed and challenging task. A good dispersion of CNTs in composites means that the individual nanotubes are distributed uniformly throughout the matrix and well-separated from each other. However, CNCs with CNTs tend to form aggregates spontaneously during the growth process. These agglomerates are extremely undesirable especially in ceramic matrices, as they may act as defects leading to stress concentration and premature failure.

Figure 5 shows the typical microstructures of agglomerated (Figure 5(a)) and homogeneous (Figure 5(b)) CNT/glass matrix composites. CNTs easily agglomerate thanks to their high aspect ratios and typically poor interaction with solvents or cement matrix composites. Within CNTs, SWCNTs are more prone to agglomerate into "ropes" or "bundles," consisting of many parallel nanotubes bound by van der Waals forces. These agglomerations lead to a decrease in mechanical and functional properties of CNCs.

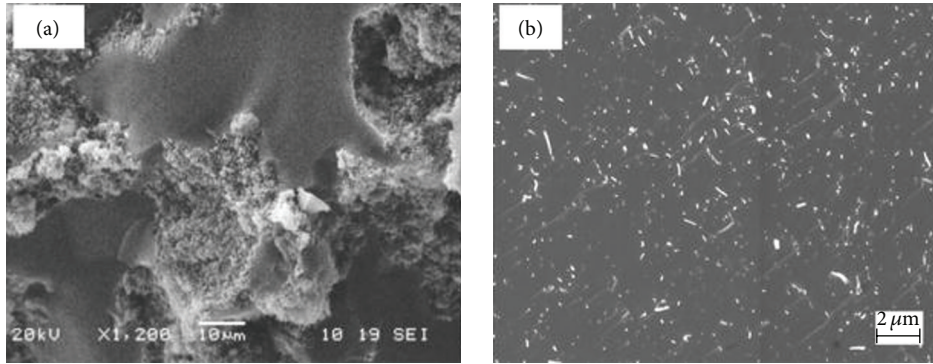


FIGURE 5: SEM images of fracture surfaces of (a) agglomerated CNTs in a borosilicate glass matrix and (b) homogeneously dispersed CNTs in a silica matrix (individually pullout CNT segments can be observed that may be related to possible toughening mechanisms) [40].

Regarding the influence of surfactants and sonication parameters on the homogeneous distribution of CNTs in ceramics, the works by Estili et al. [41] and Dassios et al. [42] must be cited. Estili et al. [41] applied a powder technology to investigate the load-carrying and reinforcing capabilities of CNT-based CNCs. They prepared surfactantless, hydrophilic, slightly disordered, crystalline, multiwalled CNTs and then incorporated them in an α -alumina ceramic. The homogeneous incorporation of these CNTs within the alumina ceramic led to a considerable increase in the fracture toughness after spark plasma sintering (SPS), proving their effectiveness in the ceramics. The bundled CNTs observed in some dried samples were individually separated by mild ultrasonication in distilled water. Although having the same crystalline structure as in these samples, the poor dispersion observed in other slightly disordered samples was probably due to inadequate functionalization. The authors attributed this evidence to cause difficulties in surrounding effectively CNTs by water molecules, and thus CNTs cannot be redispersed after drying even by strong ultrasonication. Very recently, and in order to quantify the effects of sonication parameters on CNT length and sample polydispersity, Dassios et al. [42] suggested a straightforward methodology based on CNT agglomerate size analysis by liquid mode laser diffraction. Their methodology allowed a surfactant-assisted homogeneous dispersions of multiwalled CNTs in aqueous solutions by optimization of sonication parameters (duration, energy, and surfactant loading ratio).

Typically, high loading fractions favour agglomeration, because particles come into contact more often, which explains common results for CNCs where properties are enhanced at low loading fractions but cannot be increased further due to CNT agglomeration above a small vol%. In fact, with good dispersion, each CNT is loaded individually over a maximum interfacial area, contributing directly to mechanical and toughening mechanisms. However, the situation becomes more ambiguous when addressing transport properties, such as electrical conductivity, as a network of touching CNTs is desired. Also in this case, the results indicate that an initial good dispersion favours these properties, allowing the network to form by itself. To overcome the problem of dispersion of CNTs issues many different

approaches have been proposed ranging from ultrasonic action, functionalization of surfaces, and use of surfactants [43, 44]. In terms of CNCs, several methods gain advantage as potential techniques to assure a good dispersion of CNTs in ceramic matrices: colloidal processing, sol-gel processing, electrophoretic deposition, *in situ* growth of CNTs on ceramics, and high shear compaction combined with spark plasma sintering.

Notwithstanding these dispersion issues, CNCs with addition of CNTs still attract much attention from the research community, due to potential significant improvements on mechanical and functional properties. Thanks to the brittle property of ceramic materials, most of studies aim to increase the fracture toughness. However, improvements extend to many other properties, such as flexural and bending strength, compressive strength, Young's modulus, and electrical properties. Estili and Kawasaki [45] developed an approach to mass-producing CNTs alumina composites with optimized and controlled compositions. Authors stated that homogeneous composites can only be obtained for CNT concentrations in the range of 2.4–16 vol%. However, an increase of 70% in the fracture toughness from $3.12 \times 10^6 \text{ Pa}\cdot\text{m}^{1/2}$ for monolithic to $5.20 \times 10^6 \text{ Pa}\cdot\text{m}^{1/2}$ was registered only for alumina composites with 3.5 vol% of CNTs. Also Jiang et al. [46] produced 10 vol% SWCNTs- Al_2O_3 composites by the spark plasma sintering (SPS) method that exhibit excellent toughness, ranging from $6.9 \times 10^6 \text{ Pa}\cdot\text{m}^{1/2}$ (221%) to $9.7 \times 10^6 \text{ Pa}\cdot\text{m}^{1/2}$ (310% increase related to monolithic alumina composite). Regarding fracture toughness, similar results were presented by other authors [19, 47].

Despite these positive results, the alumina composites with CNTs addition have not been sufficiently documented and recently some contrasting results came up. For example, Aguilar-Elguézabal and Bocanegra-Bernal [48] studied the fracture behaviour of alumina ceramic reinforced with a mixture of 0.05 wt% MWCNTs + 0.05 wt% SWCNTs. Although the small amounts of CNTs added to the alumina matrix, the results showed a general decrease in Vickers hardness and fracture toughness for these samples compared to monolithic alumina matrix (Figure 6). The hardness and fracture toughness of the CNCs with different types of

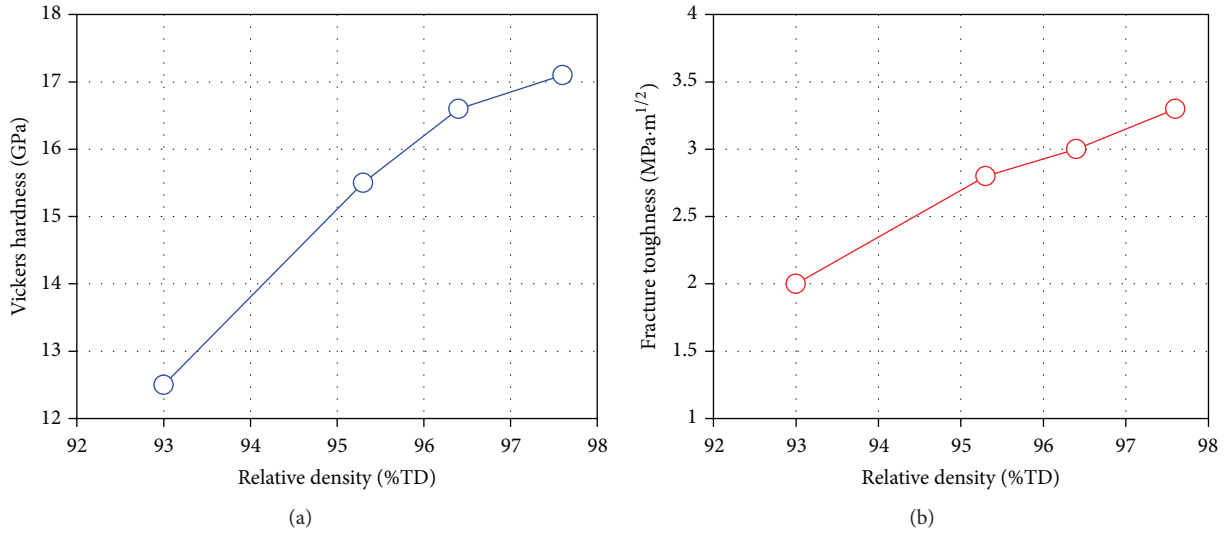


FIGURE 6: Variation of (a) Vickers hardness and (b) fracture toughness with relative density for various nanocomposites [48].

CNTs were much lower than those of pure Al_2O_3 (17.05 GPa and $3.34 \times 10^6 \text{ Pa}\cdot\text{m}^{1/2}$, resp.). The lowest hardness and fracture toughness values were registered for the composites reinforced with the mixture of SWCNTs and MWCNTs (12.45 GPa and $1.96 \times 10^6 \text{ Pa}\cdot\text{m}^{1/2}$, resp.), due to the higher porosity and the presence of clusters or bundles of CNTs that undoubtedly act as defects with no load-carrying ability.

As mentioned previously, the main difficulty to achieve a CNTs-ceramic composite is the homogeneous dispersion of CNTs in the ceramic powder. The technique proposed by Peigney et al. [49, 50], based on a catalysis method for the *in situ* production (in a composite powder) of a huge amount of CNTs bundles, was very successful. SEM observations proved that the CNT bundles were present in CNCs but in a smaller quantity than in the starting powder. Although SEM observations indicated that the CNT bundles could dissipate some fracture energy, Peigney et al. [49, 50] also concluded that the obtained mechanical properties were not improved because the reinforcement effect expected from the addition of very long CNT bundles was not observed.

Very recently, Dassios et al. [51] proposed a technique that combines high shear compaction and spark plasma sintering for the massive, cheap, and sustainable production of 100% dense ceramics containing CNTs. This technique was systematically found associated with 100% dense final materials, which dramatically improves current CNT-ceramic densification standards. MWCNT loadings of 0.5 wt.% provided optimal stiffness improvement of the borosilicate glass under both shear and axial elastic loads. Due to indications of nanoscale-specific energy dissipation mechanisms, these authors propose further research on the toughening and functional aspects of the material for a wide range of reinforcing and multifunctional applications.

Also Gallardo-López et al. [52] tested the effects of SWCNTs on the hardness and flexural strength of alumina matrix composites. Samples of fully dense Al_2O_3 and SWCNTs composites with 1, 2, 5, and 10 vol% of SWCNTs were fabricated by colloidal processing and tested. The results showed neither

increase nor decrease of hardness for samples with 1 vol% SWCNTs with respect to monolithic alumina. Moreover, a 25% decrease in hardness was found for composites with higher SWCNTs content (3, 5, and 10 vol%). Similar trends were found for flexural strength where a significant decrease was found for samples with higher contents of SWCNTs addition (48.7% decrease for 2 vol%).

These contradicting results show that much has to be done to determine ideal experimental conditions and materials processing to obtain consistent results in the addition of CNTs in ceramic matrices. From the literature, authors put forward for reflection the following aspects.

- (i) Mechanical properties are strongly affected by grain size. The CNT refinement effect on the matrix grains is greater at higher temperatures (1550–1600°C) [52]. Recently, Hanzel et al. [53] developed a new approach based on the functionalization of MWCNTs by acid treatment and stabilization of alumina/MWCNT dispersion at high temperatures (1550°C) with subsequent freezing. Figure 7 shows the high levels of dispersion obtained for the samples tested in this study.
- (ii) Many authors [47, 54] questioned the validity of the method used to measure fracture toughness using the microhardness method based on the following equation:

$$K_{IC} = \alpha \left(\frac{E}{H} \right)^{1/2} \cdot \left(\frac{P}{C^{3/2}} \right), \quad (1)$$

where E and H are Young's modulus and hardness, respectively, P is the applied load, C is the radial crack length, and α is an empirical constant which depends on the geometry of the indenter. The authors argue that the validity of the fracture toughness results depends critically on the elastic/inelastic contact-mechanical response of the material under test.

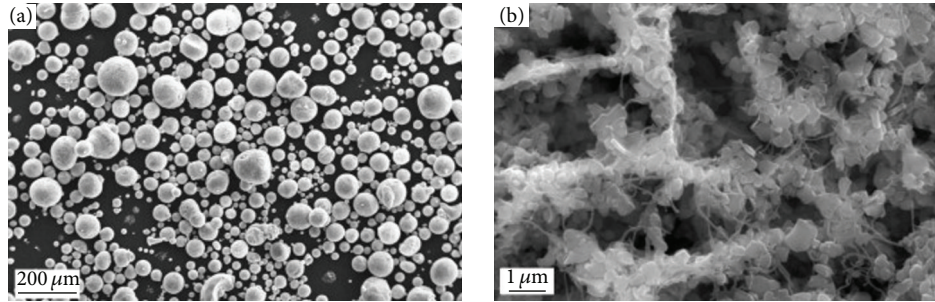


FIGURE 7: SEM images of (a) granulated alumina/CNT composite powder and (b) detail of granulate surface with distribution of MWCNTs and alumina grains [53].

According to Estili and Sakka [55], CNTs embedded in ceramic matrices experience a combination of tensile and bending loads during the bridging of the cracks of the ceramic matrix. Additionally, the rupture and/or frictional pullout of the single-walled CNT bundles during the crack bridging process contributed marginally to the energy dissipation and the mechanical improvement. Estili and Kawasaki [56] proposed a stronger intergraphene shear strength in multiwalled CNTs by embedding these into a compressive-stressing ceramic environment to exploit the exceptional strength of tube inner walls during tensile loading. A relevant enhancement in the tensile failure load of multiwalled CNTs was obtained in the ceramic environment and a new “multiwall” failure mechanism was discovered. Microstructural investigations by Dassios [57] specified the existence of highly dissipating nanoscale-specific toughening mechanisms acting complementary to CNT bridging and pullout, stipulating high potential and capabilities in a wide range of reinforcing and multifunctional applications.

The before-mentioned issues should be considered and studied to fully take advantage of CNTs potential in ceramic products. Despite these important aspects, CNTs have also been tested to increase the electrical properties and structural health monitoring capabilities of CNCs. For example, Inam et al. [58] developed a novel method for analysing the structural health of alumina nanocomposites filled with graphene nanoplatelets CNTs and carbon black nanoparticles. A change in electrical conductivity was analysed after indentation to understand the structural damage and try to establish some kind of correlation. The results showed that the change in electrical conductivity is highly dependent on the type of filler and number of indentations or damage. Damage was indicated by an irreversible decrease in electrical conductivity for the indented nanocomposite bars.

Moreover, despite the massive advantage of the use of alumina as ceramic matrix in the literature, due to its high resistance to corrosion, chemical stability, and hardness, other ceramic matrices were used. For example, SiO₂ matrices were used with various contents of CNTs additions and the results showed similar trends to those obtained with alumina [59, 60]. Still, the attention of current research is mainly aimed at achieving good dispersion of CNTs in all of these types of cement matrices.

5. Graphene-Based CNCs

Graphene (GO) has gained increasing interest from the research community in almost all areas. However, probably due to problems with the dispersion of CNTs in CNCs, studies involving the incorporation of graphene in ceramic matrices have increased highly in the last few years. Graphene, with its combination of a large specific surface area, two-dimensional high aspect ratio sheet geometry, and increased mechanical properties, shows great potential as nanofiller in composite materials. It has been shown that graphene is mainly used to reinforce polymeric matrices, as the majority of research works have dealt with graphene-reinforced polymer matrix composites (PMCs). However, the improvements in mechanical and thermal properties in PMCs have opened new perspectives for its use in bulk ceramics. The first reports on graphene/alumina composites occurred in 2009 [61], when 5% of carbon was added to the alumina matrix via milling alumina and graphite in ethanol at room temperature. Since then, much has been done. Records of improvements involve mainly properties like fracture toughness, electrical conductivity, or Vickers hardness. For example, Centeno et al. [62] prepared GO/Al₂O₃ powders and tested their mechanical and electrical properties. Regardless of the well-known problems of aggregation when reduced oxide is directly used as the second phase in hydrophilic matrices, the resulting slurries of GO/Al₂O₃ showed very good dispersion. As a consequence, the authors registered good impacts in both electrical and mechanical properties. As Figure 8 shows, an increase of 50–80% in fracture strength compared to monolithic Al₂O₃ was registered. For an optimum value of 0.22 wt% GO addition, an increase of approximately 80% was observed. Moreover, Vickers hardness of the composites was very similar to the one of the monolithic alumina. This means a good dispersion of the graphene phase that avoids the deterioration of this important property (Figure 8).

Wang et al. [64] developed another example of a graphene/alumina CNC. GO nanoplatelets were added to an Al₂O₃/water dispersion. Among several improvements, the authors registered an increase of approximately 53% of the fracture toughness compared to that of pure alumina. Moreover, an increase of the electrical conductivity up to 172 S m⁻¹ was achieved. Also, Chen et al. [63] added GO

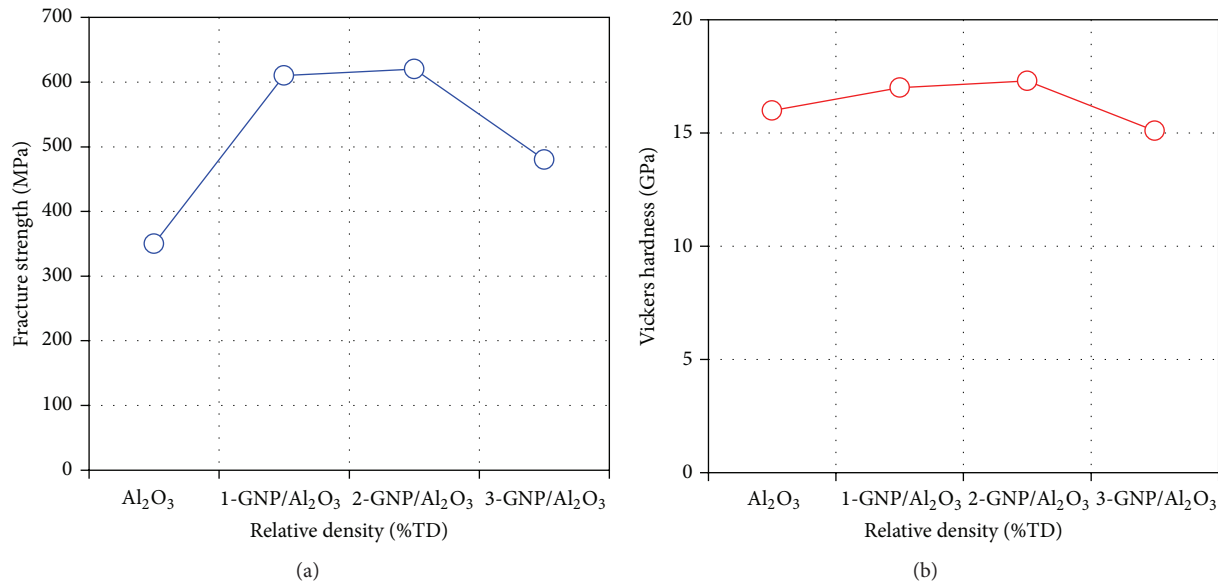


FIGURE 8: Mechanical properties of the composites and alumina: (a) fracture toughness and (b) Vickers hardness [62].

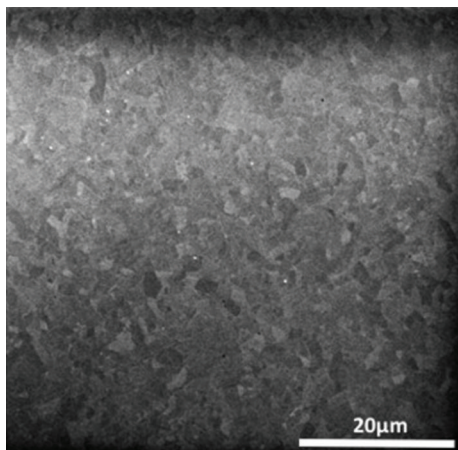


FIGURE 9: SEM image of 0.22 wt% GO/Al₂O₃ polished surface [62].

nanosheets to alumina composites by hot pressing in contents ranging from 0.1 to 1.0 wt%. These additions had impact in almost all the properties of the resulting samples. Primarily, a decrease of approximately 20% (from 2.51 μm to 2.0 μm) in average grain size was observed when GO was added to alumina matrix. The introduction of GO nanosheets hinders the growth of alumina particles making much finer particles resulting in more homogeneous materials as shown in Figure 9. Figure 10(a) shows large and uneven grains for the monolithic alumina. Contrarily, GO composites exhibit a remarkable decrease in grain size (Figure 10(b)).

Consequently, the authors registered an increase of approximately 43.5% of the fracture toughness for an optimum value of 0.2 wt% of GO/alumina composite. Also the bending strength increased by 28% (from 420 MPa to 540 MPa) with GO addition for an optimum value 0.1 wt%.

Moreover, GO addition has high impacts on cracks propagation. The authors registered four toughening mechanisms: crack deflection, enhanced by the large specific surface area of GO nanosheets (Figure 11(a)); crack stopping when cracking slows down or even stops by the action of graphene nanosheet (Figure 11(b)); crack bridging when GO nanosheets effectively dissipate fracture energy (Figure 11(c)); crack branching which constitutes cracks in lengths of several micrometres, which contributes to the increase of toughness (Figure 11(d)). Similar phenomena were reported by several other authors [18, 20, 62, 65].

Although the great majority of works regard the application of GO in alumina matrices, these outstanding results extend to other types of matrices. For example, Hvizdoš et al. [66] tested a series of silicon nitride based CNCs containing 1 and 3 wt% of four types of graphene platelets. The results showed that graphene does not tend to extensive clustering; that is, only occasional stacks are observed. This is in fact a great advantage of GO addition in ceramic matrices, especially when compared to the application of CNTs. Moreover, the incorporation of GO leads to better wear resistance. A decrease of 60% was registered in samples with 3 wt% addition of graphene nanosheets. Fan et al. [20] also registered a remarkable 235% improvement in fracture toughness due to the addition of only 1.5 vol% of graphene in silicon nitride.

Although the number of publications of GO Ceramics Nanocomposites is relatively limited when compared to other nanomaterials, such as silicon carbide or CNTs, there are no claims of a decrease in mechanical and functional properties of these nanomaterials. In fact, the potential of using these nanoparticles is so high that some authors are recently patenting processes and methods to produce these composite materials. For example, Corral et al. [67] patented novel graphene-reinforced ceramic composites and methods for making such composites materials with small amounts of these nanomaterials (0.02 to 1.5 vol%). The perspectives of using

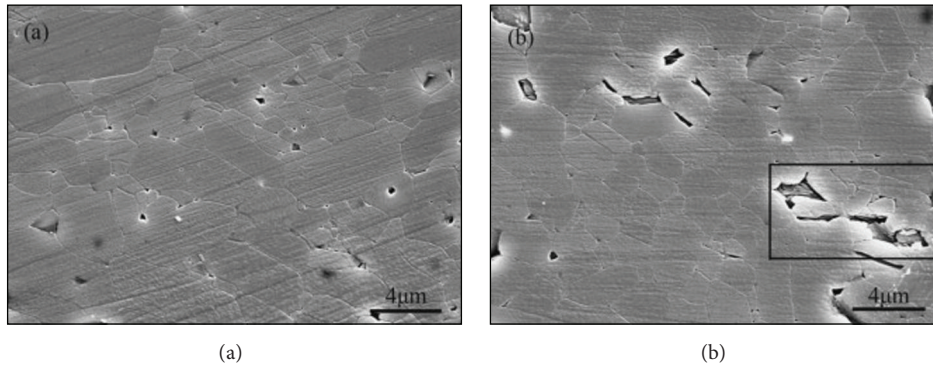


FIGURE 10: Mechanical properties of the composites and the alumina [63].

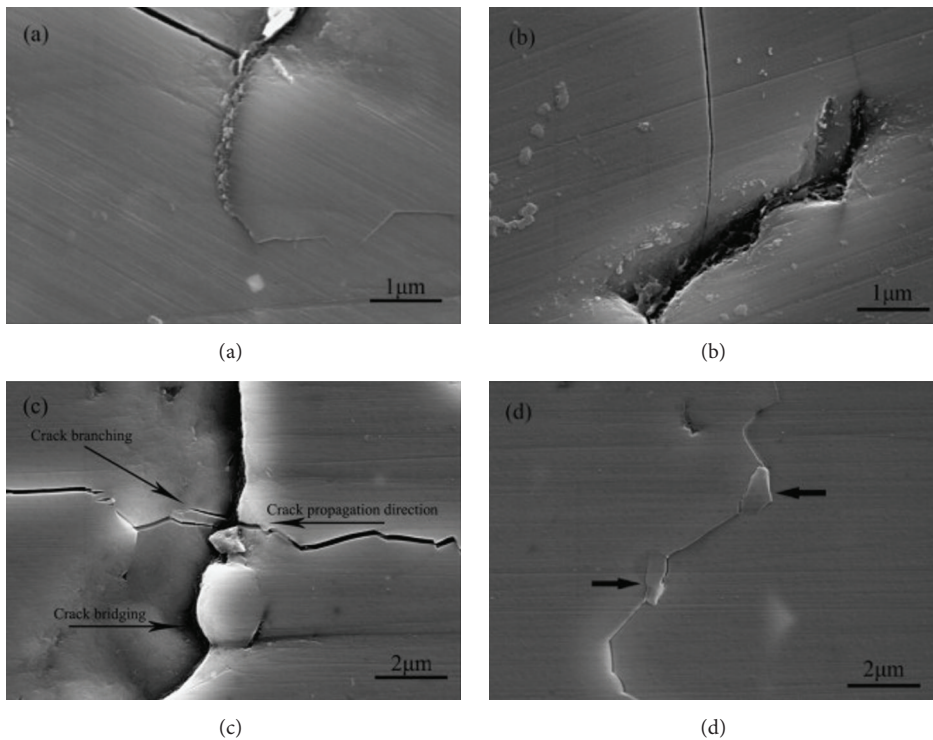


FIGURE 11: FESEM images of Vickers indentation fractured surfaces indicating the toughening mechanisms: crack deflection (a), crack stopping (b), crack bridging (c), and crack branching (d) [63].

GO in CNCs production for high temperatures applications justified their efforts to publish and protect such methods.

6. Concluding Remarks

This paper reviewed the current research status of the field of ceramic nanocomposites (CNCs) and recent developments in this area. The range of application of CNCs compared to polymer nanocomposites (PMCs) is considerably smaller, especially within the construction industry. Ceramics usually play a nonstructural role in construction, with the main applications ranging from floor, wall, and roofing tiles to bricks or glass. For example, ceramic tiles are used in floors and walls and similar materials are used to furnish bathrooms. These ceramic products are durable, relatively hygienic, and

normally used to add aesthetical value. Additionally, for these types of applications, ceramic products show high stiffness and strength, good corrosion resistance, and low thermal and electrical conductivity. The introduction of nanotechnology has allowed increasing all of these properties. Moreover, with nanotechnology new features can be added to ceramic products. For example, the introduction of CNTs or graphene allowed some ceramics to exhibit high thermal conductivity and/or high electrical conductivity.

In terms of thermal behaviour, fracture toughness and chemical resistance, silicon carbide, zirconia, and alumina show more consistent results. Their incorporation in ceramic matrix has as a primary impact an improvement of the microstructural composition with high densification, low grain growth, and elimination of porosity. Consequently, it impacts

other properties. For example, silica carbide shows the potential to increase the thermal behaviour up to a maximum of 35% for a 20 vol% addition. For additions under 20 vol%, both silica carbide and zirconia additions increase the fracture toughness up to 35% and 50–100%, respectively. Besides these improvements, the dispersion of these nanopowders in ceramic matrices is currently relatively controlled, justifying the investment of some manufacturers in producing these nanopowders, such as CoorsTek [38, 39].

Still, the biggest potential of development of hi-tech ceramic materials is the opportunity of adding carbon derived nanomaterials, particularly CNTs and graphene. Regarding CNTs, their incorporation has a tremendous impact on almost all properties of ceramic materials. For example, the results showed up to 310% increase in fracture toughness for 10 vol% addition of SWCNTs. Also, the electrical conductivity can increase up to 45% with the addition of CNTs for 5–15 vol% addition. However, the dispersion of CNTs in ceramic matrices represents a critical issue that has been preventing further developments. CNTs tend to form agglomerations, particularly in cement matrices, acting as defects leading to stress concentration and premature failure. The techniques used to process CNCs with CNTs have gradually provided better and more consistent properties compared to traditional powder processing methods. However, further developments are still required to develop higher quality samples in sufficient quantities to provide reliable results.

The problems related to the addition of CNTs enabled graphene to gain preference in the application in CNCs. The results indicate similar improvements in mechanical properties to those of CNTs, such as improvements up to 235% in fracture toughness for only 1.5 vol% addition. Much attention has been focused on describing the toughening mechanisms with the addition with these types of nanoparticles. Also the electrical conductivity increased up to 172 S m^{-1} . Despite these positive results, more research is needed in order to define optimal contents and processing methods to consistently achieve these improvements. If these issues are increasingly controlled and the impact on other mechanical properties (such as compressive strength, and bending strength) is accurately estimated, it will be possible to use CNCs as a structural material in the near future. Future developments of CNCs will be developed for aerospace applications. CNCs might be applicable to propulsion systems and hot structures with interest in both SiC-based and oxide composites. As reported by Steyer [1], whereas CMCs may be preferred for hot structure in hypersonic vehicles, CNC applications might be possible for materials supporting higher heat loads, such as ultra-high-temperature ceramics. Additionally, fundamental and applied research domains remain open for CNCs including, such as damage accumulation mechanisms/models, life predictions methodologies/modeling, nondestructive inspection techniques, and robust field and depot-level repair methods [1].

Conflict of Interests

The authors declare that there is no conflict of interests regarding the publication of this paper.

Acknowledgments

The corresponding author gratefully acknowledges the financial support given by FCT (Fundação para a Ciência e Tecnologia), in the context of the project “Modelling and Analysis of Nanostructures: Carbon Nanotubes and Nanocomposites” (PTDC/ECM/103490/2008). This work was supported by FCT, through IDMEC, under LAETA, project UID/EMS/50022/2013.

References

- [1] T. E. Steyer, “Shaping the future of ceramics for aerospace applications,” *International Journal of Applied Ceramic Technology*, vol. 10, no. 3, pp. 389–394, 2013.
- [2] T. Nozawa, T. Hinoki, A. Hasegawa et al., “Recent advances and issues in development of silicon carbide composites for fusion applications,” *Journal of Nuclear Materials*, vol. 386–388, pp. 622–627, 2009.
- [3] X.-M. Yu, W.-C. Zhou, F. Luo, W.-J. Zheng, and D.-M. Zhu, “Effect of fabrication atmosphere on dielectric properties of SiC/SiC composites,” *Journal of Alloys and Compounds*, vol. 479, no. 1–2, pp. L1–L3, 2009.
- [4] X.-H. Shi, J.-H. Huo, J.-L. Zhu et al., “Ablation resistance of SiC–ZrC coating prepared by a simple two-step method on carbon fiber reinforced composites,” *Corrosion Science*, vol. 88, pp. 49–55, 2014.
- [5] X. Zhang, C. Liu, M. Li, and J. Zhang, “Research on toughening mechanisms of alumina matrix ceramic composite materials improved by rare earth additive,” *Journal of Rare Earths*, vol. 26, no. 3, pp. 367–370, 2008.
- [6] X. H. Zhang, C. X. Liu, M. S. Li, J. H. Zhang, and J. L. Sun, “Toughening mechanism of alumina-matrix ceramic composites with the addition of AlTiC master alloys and ZrO₂,” *Ceramics International*, vol. 35, no. 1, pp. 93–97, 2009.
- [7] R. H. J. Hannink, P. M. Kelly, and B. C. Muddle, “Transformation toughening in zirconia-containing ceramics,” *Journal of the American Ceramic Society*, vol. 83, no. 3, pp. 461–487, 2000.
- [8] W.-C. Tu, F. F. Lange, and A. G. Evans, “Concept for a damage-tolerant ceramic composite with ‘strong’ interfaces,” *Journal of the American Ceramic Society*, vol. 79, no. 2, pp. 417–424, 1996.
- [9] M. Schmücker, B. Kanka, and H. Schneider, “Temperature-induced fibre/matrix interactions in porous alumino silicate ceramic matrix composites,” *Journal of the European Ceramic Society*, vol. 20, no. 14–15, pp. 2491–2497, 2000.
- [10] M. E. Westwood, J. D. Webster, R. J. Day, F. H. Hayes, and R. Taylor, “Oxidation protection for carbon fibre composites,” *Journal of Materials Science*, vol. 31, no. 6, pp. 1389–1397, 1996.
- [11] D. L. McDanel, “Analysis of stress-strain, fracture, and ductility behavior of aluminum matrix composites containing discontinuous silicon carbide reinforcement,” *Metallurgical Transactions A*, vol. 16, no. 6, pp. 1105–1115, 1985.
- [12] R. M. Laine and F. Babonneau, “Pre-ceramic polymer routes to silicon carbide,” *Chemistry of Materials*, vol. 5, no. 3, pp. 260–279, 1993.
- [13] X.-L. Su, W.-C. Zhou, F. Luo, Z.-M. Li, and D.-M. Zhu, “A cost-effective approach to improve dielectric property of SiC powder,” *Journal of Alloys and Compounds*, vol. 476, no. 1–2, pp. 644–647, 2009.
- [14] K. K. Chawla, Z. R. Xu, and J.-S. Ha, “Processing, structure, and properties of mullite fiber/mullite matrix composites,” *Journal of the European Ceramic Society*, vol. 16, no. 2, pp. 293–299, 1996.

- [15] O. Vasylykiv, Y. Sakka, and V. V. Skorokhod, "Low-temperature processing and mechanical properties of zirconia and zirconia-alumina nanoceramics," *Journal of the American Ceramic Society*, vol. 86, no. 2, pp. 299–304, 2003.
- [16] S. Sarkar and P. K. Das, "Effect of sintering temperature and nanotube concentration on microstructure and properties of carbon nanotube/alumina nanocomposites," *Ceramics International*, vol. 40, no. 5, pp. 7449–7458, 2014.
- [17] O. Tapasztó, H. Lemmel, M. Markó, K. Balázsi, C. Balázsi, and L. Tapasztó, "The influence of sintering on the dispersion of carbon nanotubes in ceramic matrix composites," *Chemical Physics Letters*, vol. 614, pp. 148–150, 2014.
- [18] P. Kun, O. Tapasztó, F. Wéber, and C. Balázsi, "Determination of structural and mechanical properties of multilayer graphene added silicon nitride-based composites," *Ceramics International*, vol. 38, no. 1, pp. 211–216, 2012.
- [19] H. Porwal, S. Grasso, and M. J. Reece, "Review of graphene-ceramic matrix composites," *Advances in Applied Ceramics*, vol. 112, no. 8, pp. 443–454, 2013.
- [20] J.-P. Fan, D.-M. Zhuang, D.-Q. Zhao et al., "Toughening and reinforcing alumina matrix composite with single-wall carbon nanotubes," *Applied Physics Letters*, vol. 89, no. 12, Article ID 121910, 4 pages, 2006.
- [21] L. S. Walker, V. R. Marotto, M. A. Rafiee, N. Koratkar, and E. L. Corral, "Toughening in graphene ceramic composites," *ACS Nano*, vol. 5, no. 4, pp. 3182–3190, 2011.
- [22] X. J. Zhao, L. R. Xiao, Z. W. Zhao et al., "Fabrication and mechanical properties of silicon carbide-aluminum oxynitride nanocomposites," *Ceramics International*, vol. 40, no. 9, pp. 14295–14303, 2014.
- [23] J. B. Casady and R. W. Johnson, "Status of silicon carbide (SiC) as a wide-bandgap semiconductor for high-temperature applications: a review," *Solid-State Electronics*, vol. 39, no. 10, pp. 1409–1422, 1996.
- [24] L. Latu-Romain and M. Ollivier, "Silicon carbide based one-dimensional nanostructure growth: towards electronics and biology perspectives," *Journal of Physics D: Applied Physics*, vol. 47, no. 20, Article ID 203001, 18 pages, 2014.
- [25] M. Parchovianský, D. Galusek, M. Michálek et al., "Effect of the volume fraction of SiC on the microstructure and creep behavior of hot pressed $\text{Al}_2\text{O}_3/\text{SiC}$ composites," *Ceramics International*, vol. 40, no. 1, pp. 1807–1814, 2014.
- [26] R. Barea, M. Belmonte, M. I. Osendi, and P. Miranzo, "Thermal conductivity of $\text{Al}_2\text{O}_3/\text{SiC}$ platelet composites," *Journal of the European Ceramic Society*, vol. 23, no. 11, pp. 1773–1778, 2003.
- [27] D. P. H. Hasselman and L. F. Johnson, "Effective thermal conductivity of composites with interfacial thermal barrier resistance," *Journal of Composite Materials*, vol. 21, no. 6, pp. 508–515, 1987.
- [28] A. Sawaguchi, K. Toda, and K. Niihara, "Mechanical and electrical properties of $\text{Al}_2\text{O}_3/\text{SiC}$ nano-composites," *Journal of the American Ceramic Society*, vol. 99, no. 6, pp. 510–513, 1991.
- [29] D. Stauffer and A. Aharony, *Introduction to Percolation Theory*, Taylor & Francis, 2nd edition, 1992.
- [30] Y. L. Dong, F. M. Xu, X. L. Shi et al., "Fabrication and mechanical properties of nano-/micro-sized $\text{Al}_2\text{O}_3/\text{SiC}$ composites," *Materials Science and Engineering A*, vol. 504, no. 1–2, pp. 49–54, 2009.
- [31] D. Djjenkal, D. Goeuriot, and F. Thevenot, "SiC-reinforcement of an Al_2O_3 - γ -AlON composite," *Journal of the European Ceramic Society*, vol. 20, no. 14–15, pp. 2585–2590, 2000.
- [32] C.-Y. Bai, X.-Y. Deng, J.-B. Li et al., "Fabrication and properties of cordierite-mullite bonded porous SiC ceramics," *Ceramics International*, vol. 40, no. 4, pp. 6225–6231, 2014.
- [33] A. Smirnov and J. F. Bartolomé, "Microstructure and mechanical properties of ZrO_2 ceramics toughened by 5–20 vol% Ta metallic particles fabricated by pressureless sintering," *Ceramics International*, vol. 40, no. 1, pp. 1829–1834, 2014.
- [34] CoorsTek—Amazing Solutions, 2014, <http://www.dynacer.com/materials/silicon-carbide/>.
- [35] R. Benavente, M. D. Salvador, F. L. Penaranda-Foix, E. Pallone, and A. Borrell, "Mechanical properties and microstructural evolution of alumina-zirconia nanocomposites by microwave sintering," *Ceramics International*, vol. 40, no. 7, pp. 11291–11297, 2014.
- [36] A. S. A. Chinelatto, A. L. Chinelatto, C. L. Ojaimi, J. A. Ferreira, and E. M. D. J. A. Pallone, "Effect of sintering curves on the microstructure of alumina-zirconia nanocomposites," *Ceramics International*, vol. 40, no. 9, pp. 14669–14676, 2014.
- [37] I. Danilenko, F. Glazunov, T. Konstantinova, G. Volkova, and V. Burkhovetski, "Effect of oxide nanofillers on fabrication, structure, and properties of zirconia-based composites," *Journal of the European Ceramic Society*, vol. 33, no. 12, pp. 2321–2325, 2013.
- [38] CoorsTek—Amazing Solutions, 2014, <http://www.dynacer.com/>.
- [39] Technox zirconia—CoorsTek—Amazing Solutions, 2014, <http://www.dynacer.com/materials/zirconia/>.
- [40] J. Cho, A. R. Boccaccini, and M. S. P. Shaffer, "Ceramic matrix composites containing carbon nanotubes," *Journal of Materials Science*, vol. 44, no. 8, pp. 1934–1951, 2009.
- [41] M. Estili, A. Kawasaki, H. Sakamoto, Y. Mekuchi, M. Kuno, and T. Tsukada, "The homogeneous dispersion of surfactantless, slightly disordered, crystalline, multiwalled carbon nanotubes in α -alumina ceramics for structural reinforcement," *Acta Materialia*, vol. 56, no. 15, pp. 4070–4079, 2008.
- [42] K. G. Dassios, P. Alafogianni, S. K. Antiohos, C. Leptokaridis, N. Barkoula, and T. E. Matikas, "Optimization of sonication parameters for homogeneous surfactant-assisted dispersion of multiwalled carbon nanotubes in aqueous solutions," *The Journal of Physical Chemistry C*, vol. 119, no. 13, pp. 7506–7516, 2015.
- [43] N. A. Fedosova, P. P. Faikov, N. A. Popova et al., "Effect of the nature of carbon nanotubes on the structure and strength of ceramic composites," *Glass and Ceramics*, vol. 71, no. 3–4, pp. 128–131, 2014.
- [44] J. Hilding, E. A. Grulke, Z. G. Zhang, and F. Lockwood, "Dispersion of carbon nanotubes in liquids," *Journal of Dispersion Science and Technology*, vol. 24, no. 1, pp. 1–41, 2003.
- [45] M. Estili and A. Kawasaki, "An approach to mass-producing individually alumina-decorated multi-walled carbon nanotubes with optimized and controlled compositions," *Scripta Materialia*, vol. 58, no. 10, pp. 906–909, 2008.
- [46] D. Jiang, K. Thomson, J. D. Kuntz, J. W. Ager, and A. K. Mukherjee, "Effect of sintering temperature on a single-wall carbon nanotube-toughened alumina-based nanocomposite," *Scripta Materialia*, vol. 56, no. 11, pp. 959–962, 2007.
- [47] G.-D. Zhan, J. D. Kuntz, J. Wan, and A. K. Mukherjee, "Single-wall carbon nanotubes as attractive toughening agents in alumina-based nanocomposites," *Nature Materials*, vol. 2, no. 1, pp. 38–42, 2003.
- [48] A. Aguilar-Elguézabal and M. H. Bocanegra-Bernal, "Fracture behaviour of α - Al_2O_3 ceramics reinforced with a mixture of

- single-wall and multi-wall carbon nanotubes,” *Composites Part B: Engineering*, vol. 60, pp. 463–470, 2014.
- [49] A. Peigney, C. Laurent, F. Dobigeon, and A. Rousset, “Carbon nanotubes grown in situ by a novel catalytic method,” *Journal of Materials Research*, vol. 12, no. 3, pp. 613–615, 1997.
- [50] A. Peigney, C. Laurent, E. Flahaut, and A. Rousset, “Carbon nanotubes in novel ceramic matrix nanocomposites,” *Ceramics International*, vol. 26, no. 6, pp. 677–683, 2000.
- [51] K. G. Dassios, G. Bonnefont, G. Fantozzi, and T. E. Matikas, “Novel highly scalable carbon nanotube-strengthened ceramics by high shear compaction and spark plasma sintering,” *Journal of the European Ceramic Society*, vol. 35, no. 9, pp. 2599–2606, 2015.
- [52] A. Gallardo-López, R. Poyato, A. Morales-Rodríguez, A. Fernández-Serrano, A. Muñoz, and A. Domínguez-Rodríguez, “Hardness and flexural strength of single-walled carbon nanotube/alumina composites,” *Journal of Materials Science*, vol. 49, no. 20, pp. 7116–7123, 2014.
- [53] O. Hanzel, J. Sedláček, and P. Šajgalík, “New approach for distribution of carbon nanotubes in alumina matrix,” *Journal of the European Ceramic Society*, vol. 34, no. 7, pp. 1845–1851, 2014.
- [54] X. Wang, N. P. Padture, and H. Tanaka, “Contact-damage-resistant ceramic/single-wall carbon nanotubes and ceramic/graphite composites,” *Nature Materials*, vol. 3, no. 8, pp. 539–544, 2004.
- [55] M. Estili and Y. Sakka, “Recent advances in understanding the reinforcing ability and mechanism of carbon nanotubes in ceramic matrix composites,” *Science and Technology of Advanced Materials*, vol. 15, no. 6, Article ID 064902, 2014.
- [56] M. Estili and A. Kawasaki, “Engineering strong intergraphene shear resistance in multi-walled carbon nanotubes and dramatic tensile improvements,” *Advanced Materials*, vol. 22, no. 5, pp. 607–610, 2010.
- [57] K. G. Dassios, “Carbon nanotube-reinforced ceramic matrix composites: processing and properties,” in *High Temperature Ceramic Matrix Composites 8: Ceramic Transactions*, L. Zhang and D. Jiang, Eds., vol. 248, pp. 133–157, Wiley, 2014.
- [58] F. Inam, T. Vo, and B. R. Bhat, “Structural stability studies of graphene in sintered ceramic nanocomposites,” *Ceramics International*, vol. 40, pp. 16227–16233, 2014.
- [59] M. J. de Andrade, M. D. Lima, C. P. Bergmann et al., “Carbon nanotube/silica composites obtained by sol-gel and high-pressure techniques,” *Nanotechnology*, vol. 19, no. 26, Article ID 265607, 7 pages, 2008.
- [60] C. Zheng, M. Feng, X. Zhen, J. Huang, and H. Zhan, “Materials investigation of multi-walled carbon nanotubes doped silica gel glass composites,” *Journal of Non-Crystalline Solids*, vol. 354, no. 12–13, pp. 1327–1330, 2008.
- [61] T. He, J. Li, L. Wang, J. Zhu, and W. Jiang, “Preparation and consolidation of alumina/graphene composite powders,” *Materials Transactions*, vol. 50, no. 4, pp. 749–751, 2009.
- [62] A. Centeno, V. G. Rocha, B. Alonso et al., “Graphene for tough and electroconductive alumina ceramics,” *Journal of the European Ceramic Society*, vol. 33, no. 15–16, pp. 3201–3210, 2013.
- [63] Y.-F. Chen, J.-Q. Bi, C.-L. Yin, and G.-L. You, “Microstructure and fracture toughness of graphene nanosheets/alumina composites,” *Ceramics International*, vol. 40, no. 9, pp. 13883–13889, 2014.
- [64] K.-D. Wang, Y.-B. Jia, Z.-J. Lai, and Y.-F. Liu, “Ab initio study on ionization energies of 3-amino-1-propanol,” *Chinese Journal of Chemical Physics*, vol. 24, no. 3, pp. 315–318, 2011.
- [65] H. J. Kim, S.-M. Lee, Y.-S. Oh et al., “Unoxidized graphene/alumina nanocomposite: fracture- and wear-resistance effects of graphene on alumina matrix,” *Scientific Reports*, vol. 4, article 5176, 10 pages, 2014.
- [66] P. Hvizdoš, J. Dusza, and C. Balázs, “Tribological properties of Si₃N₄-graphene nanocomposites,” *Journal of the European Ceramic Society*, vol. 33, no. 12, pp. 2359–2364, 2013.
- [67] E. L. Corral, L. S. Walker, V. R. Marotto, M. A. Rafiee, and N. Koratkar, “Graphene-Reinforced Ceramic Composites and Uses Therefor,” Patent 20130184143, 2013.

Research Article

In Situ Synthesis of Reduced Graphene Oxide-Reinforced Silicone-Acrylate Resin Composite Films Applied in Erosion Resistance

Yang Cao,¹ Xiaoyong Tian,¹ Yan Wang,¹ Youyi Sun,¹ Hailin Yu,¹
Dian-sen Li,² and Yaqing Liu¹

¹Research Center for Engineering Technology of Polymeric Composites of Shanxi Province, North University of China, Taiyuan 030051, China

²Key Laboratory of Bio-Inspired Smart Interfacial Science and Technology of Ministry of Education, Beijing Key Laboratory of Bio-Inspired Energy Materials and Devices, School of Chemistry and Environment, Beijing University of Aeronautics and Astronautics, Beijing 100191, China

Correspondence should be addressed to Youyi Sun; syyi@pku.edu.cn and Yaqing Liu; lyqzgz2010@163.com

Received 24 May 2015; Revised 19 August 2015; Accepted 24 August 2015

Academic Editor: Konstantinos I. Tserpes

Copyright © 2015 Yang Cao et al. This is an open access article distributed under the Creative Commons Attribution License, which permits unrestricted use, distribution, and reproduction in any medium, provided the original work is properly cited.

The reduced graphene oxide reinforced silicone-acrylate resin composite films (rGO/SAR composite films) were prepared by in situ synthesis method. The structure of rGO/SAR composite films was characterized by Raman spectrum, atomic force microscope, scanning electron microscopy, and thermogravimetric analyzer. The results showed that the rGO were uniformly dispersed in silicone-acrylate resin matrix. Furthermore, the effect of rGO loading on mechanical properties of composite films was investigated by bulge test. A significant enhancement (ca. 290% and 320%) in Young's modulus and yield stress was obtained by adding the rGO to silicone-acrylate resin. At the same time, the adhesive energy between the composite films and metal substrate was also improved to be about 200%. Moreover, the erosion resistance of the composite films was also investigated as function of rGO loading. The rGO had great effect on the erosion resistance of the composite films, in which the R_{corr} (ca. 0.8 mm/year) of composite film was far lower than that (28.7 mm/year) of pure silicone-acrylate resin film. Thus, this approach provides a novel route to investigate mechanical stability of polymer composite films and improve erosion resistance of polymer coating, which are very important to be used in mechanical-corrosion coupling environments.

1. Introduction

An intense effort is underway to find coatings that inhibit the process of metal corrosion, a problem costing US industries more than \$200 billion annually [1]. Corrosion can be inhibited or controlled by introducing a stable protective layer made of inert metals [2], conductive polymers [3], or even thiol-based monolayers [4] between a metal and a corrosive environment. In particular, polymeric coating has attracted considerable interest due to lightweight, low-cost, and being fabricated easily and inexpensively by employing cost-effective techniques, for instance, inkjet and spray coating [5–7]. Most of these works have focused more on erosion

resistance of polymeric coating. However, the application environment of corrosion-resistant polymeric coating was multienvironmental fields of corrosion, mechanics, and thermo in practical engineering [8]. In addition to this, the erosion resistance of polymeric coatings was usually closely related to their mechanical properties such as Young's modulus, ultimate tensile strength, and adhesive energy. For example, when the coating barrier was mechanically damaged and the corrosive species penetrate the metal surface, the corrosion process could not be avoided [8, 9]. So, the study of mechanical behavior was very important to design and practical application of corrosion-resistant polymer thin film. However, there were few works reporting on the

mechanical behavior of corrosion-resistant polymer thin film because these mechanical properties (i.e., elastic modulus, yield strength, and adhesive energy) of corrosion-resistant polymeric coatings were difficult to be measured by the conventional tensile test [10]. Therefore, it is of great necessity to find a new method to investigate the mechanical properties of corrosion-resistant polymer thin film with metal substrate. Silicone-acrylate resin was a common polymeric coating that inhibited the process of metal corrosion [11]. And graphene was the strongest material and effective corrosion-inhibiting materials known to man [12]. So, graphene nanosheets (GNS) reinforced silicone-acrylate resin thin film is expected to be a good kind of anticorrosive material with high performance. To the best of our knowledge, the erosion resistance of polymer composite thin film based on graphene materials was rarely reported.

In this study, the GNS reinforced silicone-acrylate resin composite thin film was prepared by the in situ synthesis method. Furthermore, their mechanical properties (i.e., elastic modulus, yield stress, and adhesive energy) were characterized by the modified bulge test. Moreover, erosion resistance of GNS-based silicone-acrylate resin coating was also investigated by electrochemical measurements. These results are very important to improve the mechanical properties and erosion resistance of polymer coating, which is used as a stable protective layer applied in metal corrosion.

2. Experimental

2.1. Materials. Nature graphite flakes (325 mesh, 99.8%), sodium hydroxide emulsion (37.0 wt%), and other chemicals and reagents used in this work are of analytical grade. Deionized water was used for preparation, dilution, and analytical purpose.

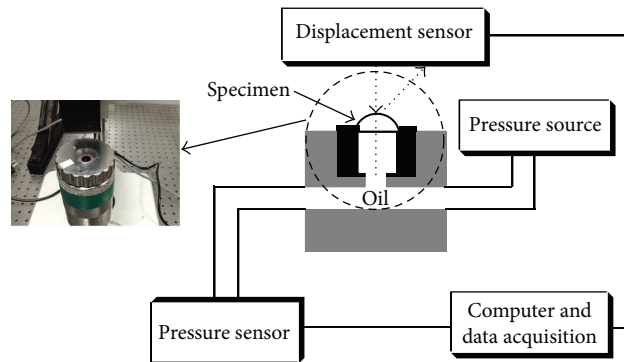
2.2. Preparation of rGO/Silicone-Acrylate Resin Composite Film. rGO was prepared from natural graphite by our own group, and the preparation process was shown in previous work [13]. An appropriate amount of rGO aqueous solution (2.5 mg/mL), calculated by 0, 0.27, 1.1, and 1.93 wt% with respect to silicone-acrylate resin, was introduced into the solution containing silicone-acrylate and then further mixed under magnetic stirring for 1 h at room temperature. The resultant mixture was coated onto a clean Zn plate and then cured at 80°C for 2 h.

2.3. Characterization. Raman spectrum was collected on a Jobin-Yvon LabRam HR800 Raman spectroscope equipped with a 514.5 nm laser source.

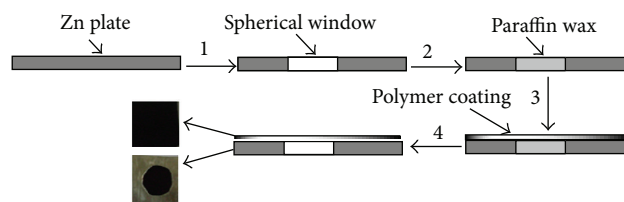
AFM images were taken of rGO by a NTMDT NTEGRA SPM instrument with NSG03 noncontact “golden” cantilevers.

The morphology of samples was observed by scanning electron microscopy (SEM) (Su-1500, HITACHI, Japan) with an accelerating voltage of 20 kV.

Thermogravimetric analysis (TGA) was carried out using a TA Q600 instrument in a temperature range from 20 to 600°C with a heating rate of 10°C min⁻¹ in air.



SCHEME 1: The bulge test setup used in present work.



SCHEME 2: Schematic illustration for the stepwise preparation of the sample used in bulge test.

2.4. Mechanics Measurement by Bulge Test

2.4.1. Bulge Test System. Mechanical properties of polymeric coating were characterized by the bulge test as shown in Scheme 1. The system contains a small inner chamber used to control the pressure exerted on the coating and a large outer chamber for ambient control. The pressurizing medium was dry nitrogen and the flow rate was controlled by a mass flow controller. A pressure gauge was installed to the chamber and the pressure signals were transferred to a computer for recording and to a processor controller for regulating a proportional valve to maintain an intended pressure. The Michelson type of interferometer was used to measure the bulging of the coating. The difference between our optical setup and a typical Michelson interferometer was that the optical window used for the chamber acted as the reference mirror. An expander lens was used to expand the interference pattern onto a viewing screen. The interference pattern was then recorded using a digital video recorder with a frame rate of 30 frames/s. The recorded images and the bulge height were then transferred to a computer for analysis.

2.4.2. Preparation of Sample Used in Bulge Test. Preparation of sample used in bulge test was shown in Scheme 2. Firstly, chemical-etching method was used to fabricate spherical window in center of Zn plate (2.0 cm × 2.0 cm), in which the diameter of spherical window was about 10.0 mm. Secondly, paraffin wax was filled into spherical window in center of Zn plate. Thirdly, the rGO/silicone-acrylate resin mixture solution was coated onto surface of Zn plate with spherical window and cured at 60°C for 10.0 min. Finally, the paraffin

wax was removed by heating at 80°C and the rGO/silicone-acrylate resin composite film with Zn plate substrate was further cured at 80°C for 2 hours.

2.4.3. Theory. The generalized equation for bulge test has been established by Huang et al. [14] following the energy-minimization approach and can be expressed as

$$\begin{aligned} P &= \frac{4t}{a^2} \sigma_0 h + \frac{8tY}{3a^4} h^3, \\ \frac{P}{h} &= \frac{4t}{a^2} \sigma_0 + \frac{8tY}{3a^4} h^2, \end{aligned} \quad (1)$$

where P is the pressure, σ_0 is residual stress, h is bulge height measured at the center of the window, a is the dimension of the window, t is the coating thickness, and Y is the biaxial modulus of the polymer coating and is defined as $E/(1-\nu)$. E and ν are Young's modulus and Poisson ratio (ca. 0.45) of polymer coating [15], respectively.

For the small strain case, the yield stress expression can be expressed as [16]

$$\sigma = \frac{P_0 a^2}{4h_0 t}, \quad (2)$$

where σ is yield strength, P_0 is the pressure, and h_0 is bulge height, which are obtained from the cure of P versus h and correspond to elastic deformation transferred to plastic deformation.

For the elastic strain case, the adhesive energy expressions can be expressed as [17]

$$G = \frac{P_0 h_0}{f(\nu)} \left(\frac{1}{8\gamma} + \frac{\gamma^2 (1-\nu^2)}{2} \right), \quad (3)$$

$$f(\nu) = \sqrt[3]{\frac{3(1-\nu)}{7-\nu}}, \quad (4)$$

where G is the adhesive energy of interface between polymer composite coating and Zn plate substrate, P_0 is the pressure, and h_0 is bulge height, which are obtained from the cure of P/h versus h^2 and correspond to elastic deformation transferred to plastic deformation, and ν is Poisson ratio and is assumed as 0.45. And then $\gamma = g(\nu) = 0.362$.

2.5. Corrosion Measurements

2.5.1. Preparation of Sample Used in Corrosion Measurements.

As a typical procedure to prepare samples for corrosion measurements, freshly the rGO/silicone-acrylate resin mixture solution was coated onto the Zn plate (2.0 cm × 2.0 cm) and the rGO/silicone-acrylate resin composite film dried for 2 h at 80°C. The rGO/silicone-acrylate resin composite film with Zn plate substrate was then mounted to the working electrode. The other uncoated side and edges of Zn plate were sealed with super-fast epoxy cement (SPARR).

2.5.2. Electrochemical Measurements. All the electrochemical measurements of corrosion potential and corrosion current were performed on a Volta Lab model 21 Potentiostat/Galvanostat in a standard corrosion test cell equipped with a saturated calomel reference electrode (SCE) and a working electrode, and all experimental data were repeated at least three times. The electrolyte was an aqueous solution containing 3.5 wt% of sodium chloride. Open circuit potential (OCP) at the equilibrium state of the system was recorded as the corrosion potential [E_{corr} (V) versus SCE]. Corrosion current (I_{corr}) is determined by superimposing the straight line along the linear portion of the cathodic or anodic curve and extrapolating it through E_{corr} . Corrosion rate (R_{corr} , mm/year) is calculated from the following equation [18]:

$$R_{\text{corr}} \text{ (mm/year)} = \frac{(3270 \times I_{\text{corr}} \times EW)}{\rho}, \quad (5)$$

where EW is the equivalent weight (g), I_{corr} is the corrosion current density ($\mu\text{A}/\text{cm}^2$), and ρ is the density (g/cm^3).

3. Results and Discussion

3.1. Preparation of rGO/Silicone-Acrylate Resin Composite Film.

The Raman spectrum of rGO/silicone-acrylate resin composite film was shown in Figure 1(a). It clearly shows two peaks of 1340.3 cm^{-1} and 1594.6 cm^{-1} assigned to D and G bands of rGO, and the $I_{\text{D}}/I_{\text{G}}$ intensity ratio is about 1.1, implying the existence of rGO in the composite film [19]. The rGO/silicone-acrylate resin composite film was further characterized by the atomic force microscopy (AFM) as shown in Figure 1(b). It clearly showed some sheet-like fillers in silicone-acrylate resin matrix, which may be assigned to rGO sheets. At the same time, it clearly showed that the size and thickness of rGO sheets were about $5.5 \mu\text{m}$ and 2.4 nm , respectively. These results confirmed the formation of rGO/silicone-acrylate resin composite film with good dispersion.

The structure of rGO/silicone-acrylate resin composite film was investigated by the SEM as shown in Figure 2. The SEM images reveal very different morphologies for rGO/silicone-acrylate resin composite film with various contents of rGO. The smooth layer mainly consists of polymer while the interior ones (bright spots) are due to the rGO phase, which confirms the particles' distribution on the surface. The SEM images also show that the composite films consist of rGO fillers with sheet-like shape for the as-grown film and agglomerated mosaic structures observed for the composite films with rGO content of 1.9 wt%. In addition, the surfaces of all films were smooth, pin hole free, and free of cracks, which was very important to improve the corrosion resistance of coatings. The insets in Figures 2(b)–2(d) display the optical images of the composite films. The surface color of the pure silicone-acrylate resin film that changed from transparent (in inset in Figure 2(a)) to black also demonstrates the doping of rGO in silicone-acrylate resin matrix. In addition to this, the black color was uniform on composite films. These results indicate that the rGO could be uniformly dispersed in silicone-acrylate resin matrix by a simple method.

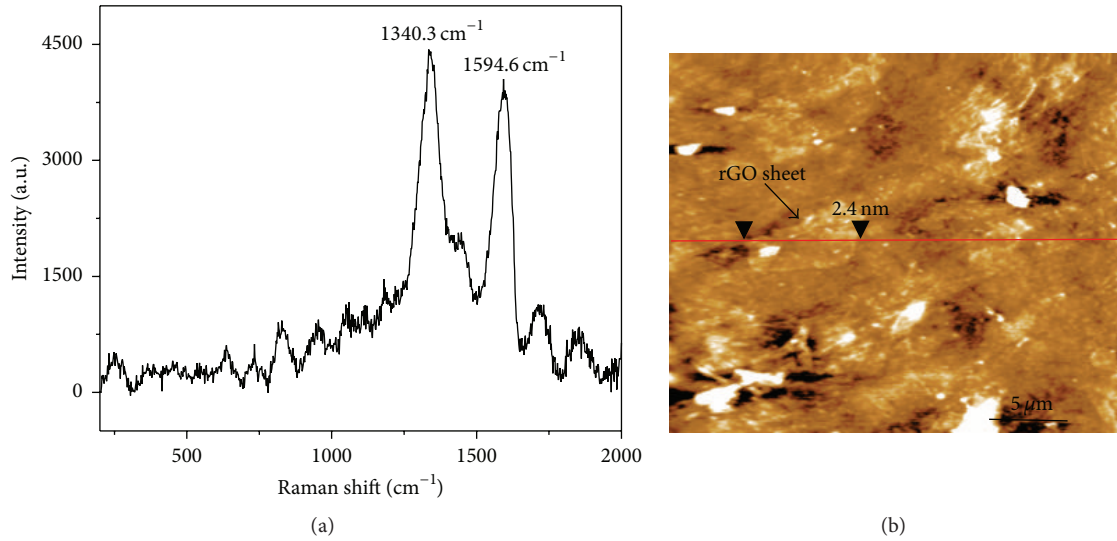


FIGURE 1: (a) Raman spectrum and (b) AFM of polymer composite film.

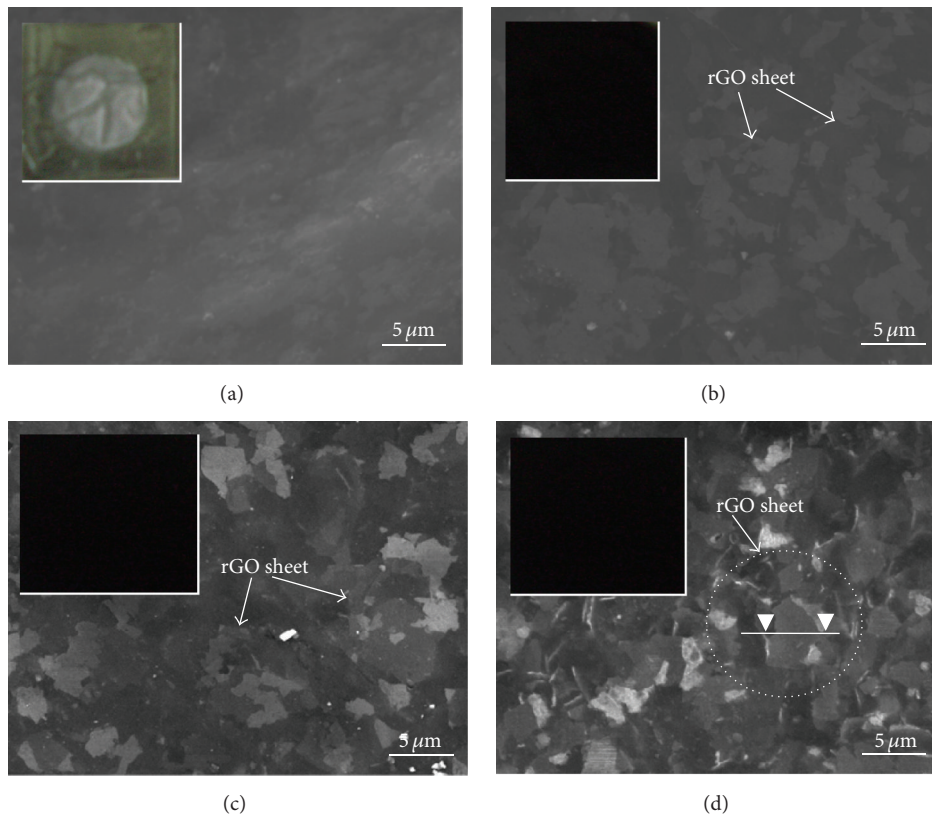


FIGURE 2: SEM of polymer composite film with various rGO contents of (a) 0, (b) 0.27 wt%, (c) 1.1 wt%, and (d) 1.93 wt%. The insets show the photographs of polymer composite films.

Figure 3 shows the thermogravimetric (TGA) analysis of rGO/silicone-acrylate resin composite film. As shown in Figure 3, all the samples have only one decomposition step. The thermal stability of rGO/silicone-acrylate resin composite films was clearly increased, which are determined from the thermal decomposition temperature at weight loss of

10.0 wt% (T_{10}). T_{10} of composite films increased from 307.0°C to 336.0°C , corresponding to doping content of 0 and 1.93 wt%. It may be due to the interactions between the rubber matrix and the fillers. The NR macromolecules are attached on GO surface, which thus decreased the amplitude of their thermal motions as well as the degradation probability [20].

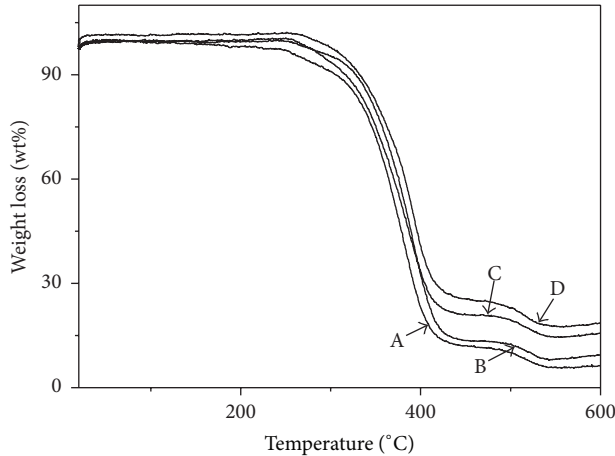


FIGURE 3: TG curves of polymer composite films with various rGO contents of (a) 0, (b) 0.27 wt%, (c) 1.1 wt%, and (d) 1.93 wt%.

Here, the good dispersion of rGO in silicone-acrylate resin matrix is also responsible for the improvement of T_{10} , resulting in formation of more physical cross-linking point between inorganic particles and polymer matrix.

3.2. Mechanical Properties and Erosion Resistance of rGO/Silicone-Acrylate Resin Composite Film. Figure 4 showed typical pressure versus deflection curves of rGO/silicone-acrylate resin composite film, which was measured by the bulge test. Regardless of the processing conditions, the mechanical properties of silicone-acrylate resin were altered significantly by the rGO sheets. All composite films showed increased modulus and strength versus neat silicone-acrylate resin film, and the modulus and strength have strong dependence on rGO loading. As shown in Table 1, the strength and moduli are improved rapidly with the increasing rGO content. However, they show a gradual decrease with further addition of rGO. The significant improvements of the strength and moduli are due to the very good exfoliation, high aspect ratio, uniform distribution of rGO in the silicone-acrylate resin matrix, and the hydrogen bonding between rGO and the polymer [21]. These interactions are believed to assist in forming a glassy layer at the filler-rubber interface. During the bulge test, the chains in this glassy layer could be easily reorientated and aligned together by slipping the chains along the filler [22]. After the chains' reorientation, the external stress can be distributed uniformly to avoid stress concentration [21]. When rGO content is more than 1.1 wt%, the strength and moduli start to slightly decrease because of the aggregation of excessive rGO content as shown in Figure 2. In addition, it can be seen that the experimental results coincide with the elastic theory only when the pressure is small. As the pressure increases, the results evidently deviate from that of elastic theory. It indicates that considerable viscoelastic deformation is induced under high stress. It can also be seen that the pressure versus deflection curves of these composite films trended toward that of a thermoplastic deformation at higher pressure comparing to pure silicone-acrylate resin film.

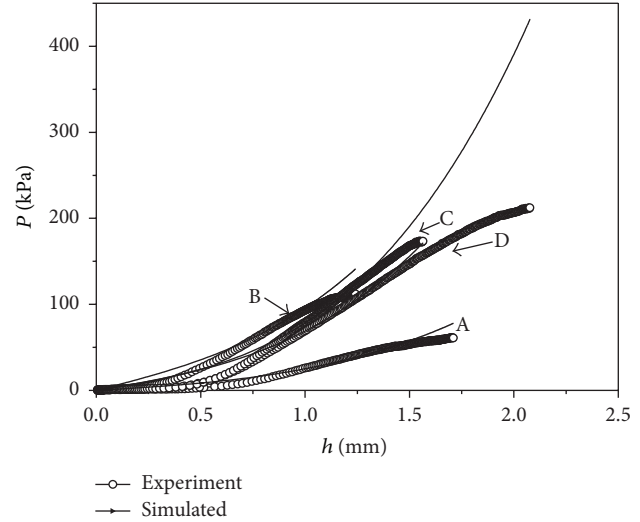


FIGURE 4: The bulge test data of polymer composite films with various rGO contents of (a) 0, (b) 0.27 wt%, (c) 1.1 wt%, and (d) 1.93 wt%.

Adhesion energy of rGO/silicone-acrylate resin composite film against the rGO content was calculated by (3) as shown in Table 1, too. The adhesion energy between rGO/silicone-acrylate resin composite film and Zn substrate was significantly improved compared with pure silicone-acrylate resin film. It also showed that adhesion energy increased with increase in the rGO content. The average adhesion energy for pure silicone-acrylate resin film was about 5.5 N/m. The adhesion energy gradually increased to 12.3 N/m for the polymer composite films with rGO content of 1.93 wt%, corresponding to an improvement of 224.0%. This indicated that the introduction of rGO into silicone-acrylate resin matrix could effectively improve the interface force between silicone-acrylate resin film and metal substrate. The result was attributed to the fact that the interatomic force between rGO and metal was stronger than the typical van der Waals force between silicone-acrylate resin and metal [22]. The stronger bonding was due to an increase in the electronic density at the interface between the rGO and the metal, although the bonding type was basically van der Waals adhesion [23]. To the best of our knowledge, this has not been explicitly demonstrated elsewhere and therefore requires further study.

The corrosion protection of Zn plates by rGO/silicone-acrylate resin composite film was investigated by electrochemical impedance spectroscopy as shown in Figure 5. And then the corrosion potential (E_{corr}), corrosion current (I_{corr}), and corrosion rate (R_{corr}) were listed in Table 2. It clearly showed that the Zn plates coated with GNS reinforced silicone-acrylate resin composite films all showed lower values of I_{corr} and R_{corr} than the pure silicone-acrylate resin film, implying that the rGO/silicone-acrylate resin composite films were nobler toward electrochemical corrosion relative to the pure silicone-acrylate resin. For example, the rGO/silicone-acrylate resin composite film (1.1 wt%) with Zn substrate showed a low I_{corr} value of $0.45 \mu\text{A}/\text{cm}^2$ in 3.5 wt% NaCl, which was about three orders of magnitude lower than the

TABLE 1: The mechanical properties of the polymer composite film measured by the bulge test.

Loading (wt%)	Biaxial modulus (GPa)	Young's modulus (GPa)	Residual stress (MPa)	Yielded stress (MPa)	G (N/m)
0	0.08	0.05	4.6	8.2	5.5
0.27	0.13	0.07	10.3	14.8	6.1
1.10	0.25	0.14	10.5	24.1	11.4
1.93	0.20	0.11	12.2	22.7	12.3

TABLE 2: Anticorrosive performance of polymer composite film measured from electrochemical measurements.

Loading	E_{corr} (mV)	I_{corr} ($\mu\text{A}/\text{cm}^2$)	R_{corr} (mm/year)
0	-327	13.8	28.7
0.27%	-878	6.2	4.6
1.1%	-585	0.45	0.8
1.93%	-976	6.7	5.0

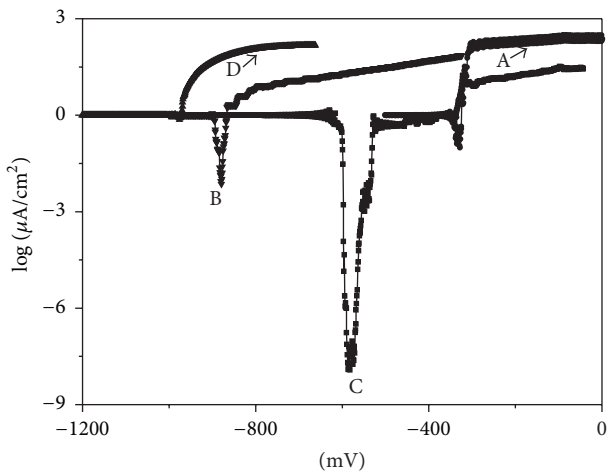


FIGURE 5: The Tafel plots for polymer composite films with various rGO contents of (a) 0, (b) 0.27 wt%, (c) 1.1 wt%, and (d) 1.93 wt%.

pure silicone-acrylate resin film with Zn substrate. The corresponding R_{corr} of rGO/silicone-acrylate resin composite film (1.1 wt%) with Zn substrate was ca. 0.8 mm/year, which was smaller than that (28.7 mm/year) of silicone-acrylate resin film. Although only a small proportion of rGO was incorporated into the silicone-acrylate resin film, high corrosion protection was afforded. By comparison with that of silicone-acrylate resin film in the previous works [11, 24, 25], the corresponding R_{corr} of rGO/silicone-acrylate resin composite film was smaller. The good corrosion resistance may be attributed to the following two reasons: (1) silicone-acrylate resin could act as a physical barrier coating and (2) the well-dispersed rGO embedded in silicone-acrylate resin matrix could prevent corrosion owing to a relatively higher aspect ratio than clay platelets, which enhances the oxygen barrier property of rGO/silicone-acrylate resin composite film [10, 25].

Figure 6 showed typical SEM images of the corroded surface of uncoated and coated Zn plates after 6 days of

immersion in 3.5 wt% NaCl solution. It clearly showed that no distinct cracks or pitting corrosion was observed for all Zn plates coated with rGO/silicone-acrylate resin composite thin film compared with the uncoated Zn specimen (in Figure 6(b)). Additionally, there were no changes in the surface of the coated specimen before and after corrosion (Figures 6(a) and 6(c)–6(f), resp.). These results indicated that silicone-acrylate resin film was a good kind of protective layer for inhibiting the process of metal corrosion. Surface of the all specimens coated with polymer coating after corrosion was furthermore compared as shown in Figures 6(c)–6(f). It was obvious that there were some holes on surface of Zn plates coated with pure silicone-acrylate resin and rGO/silicone-acrylate resin composite film (1.93 wt%), indicating the presence of local corrosion. Contrarily, there were no holes on surface of Zn plates coated with rGO/silicone-acrylate resin composite films (0.27 wt% and 1.1 wt%). Based on the results of the electrochemical tests and corroded surface analysis, the rGO/silicone-acrylate resin composite films (0.27 wt% and 1.1 wt%) exhibited better corrosion resistance than other samples. The results were similar to the mechanical properties of polymer composite films as function of rGO content. It is well-known that mechanical properties (such as Young's modulus and hardness) and erosion resistance play important roles in the corrosion behavior of materials: a low mechanical property with high porosity and erosion resistance allows for the penetration of solution, which leads to local corrosion [10]. The rGO/silicone-acrylate resin composite film (0.7 wt%) exhibited better mechanical properties and a finer and more dense surface as shown in Table 1 and Figure 2, respectively. In addition to this, rGO was a good inhibitor and rGO distributed on silicone-acrylate resin matrix could form a good protective layer to act as a barrier to the penetration of solution [26–28]. For these reasons, the rGO/silicone-acrylate resin composite film with good mechanical properties presented better corrosion resistance.

4. Conclusions

The rGO/silicone-acrylate resin composite films were prepared by in situ synthesis method and the rGO was well dispersed in the silicone-acrylate resin matrix and had good adhesion with silicone-acrylate resin matrix. Furthermore, the bulge tests were used to investigate the mechanical properties of rGO/silicone-acrylate resin composite films. The result measured by the bulge tests clearly showed that elastic modulus, yield stress, and adhesive energy of silicone-acrylate resin films were obviously improved by the introduction of rGO. Moreover, the erosion resistance of

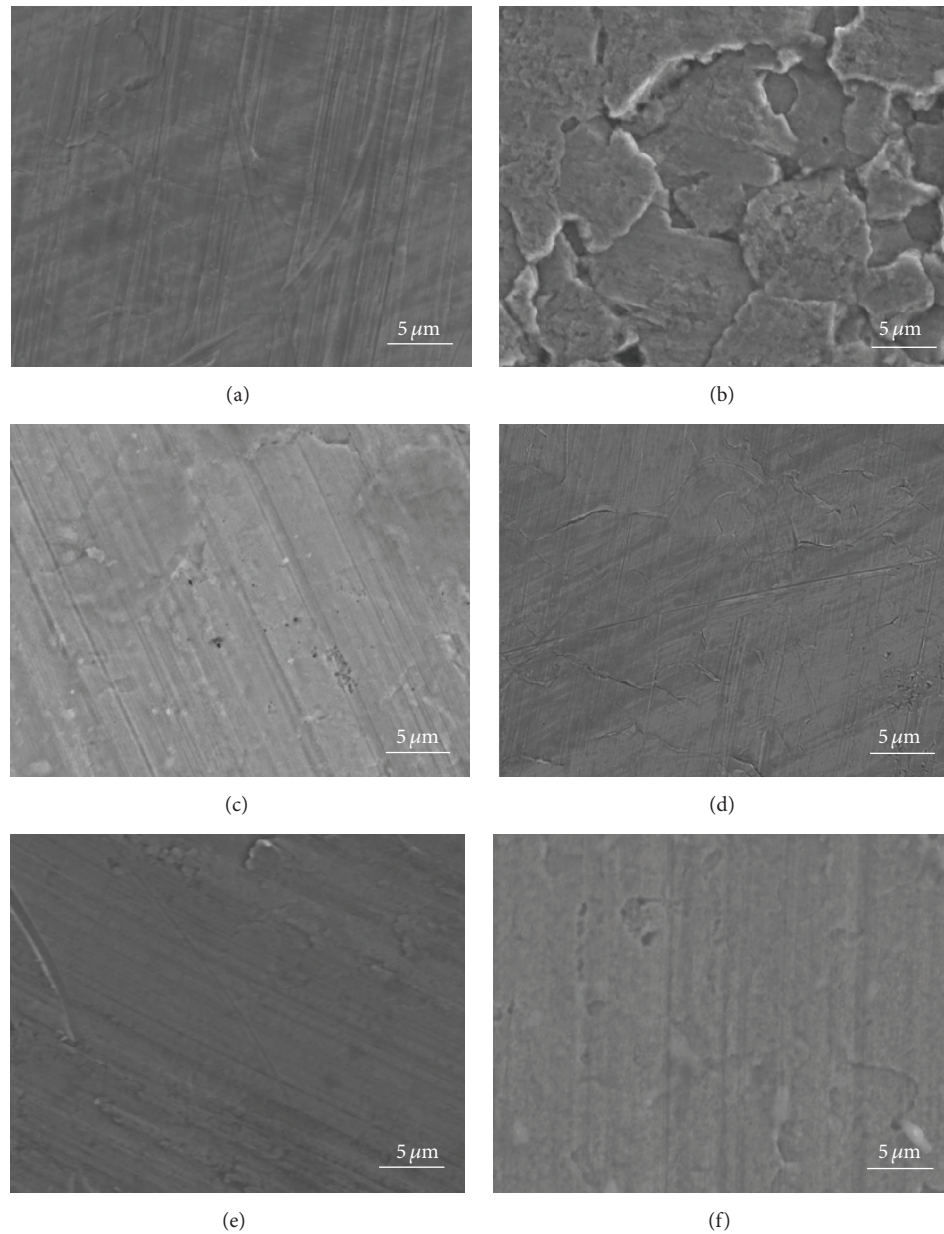


FIGURE 6: SEM images of uncoated Zn plate (a) before and (b) after corrosion; Zn plate coated polymer composite films with various rGO contents of (c) 0, (d) 0.27 wt%, (e) 1.1 wt%, and (f) 1.93 wt%.

rGO/silicone-acrylate resin composite film was also better comparing to the pure silicone-acrylate resin film. These results provide a novel route for studying and improving mechanical properties of rGO/polymer composite film with good erosion resistance. And the further investigations in erosion resistance of rGO/silicone-acrylate resin composite film under mechanic-corrosion coupled field have been carried out by our group.

Conflict of Interests

The authors declare that there is no conflict of interests regarding the publication of this paper.

Acknowledgments

The authors are grateful for the support by National Natural Science Foundation of China (under Grants 11202006 and 11202007), University's Science and Technology Exploiture of Shanxi Province (20121010), and the Shanxi Provincial Natural Science Foundation of China (2014021018-6).

References

- [1] Corrosion Costs and Preventive Strategies in the United States, 2002, <http://isddc.dot.gov/OLPFiles/FHWA/011536.pdf>.
- [2] C. Yang, W. M. Guo, H. X. Zhang, R. Qiu, J. Hou, and Y. B. Fu, "Study on the corrosion behavior of 7A52 Al alloy welded joint

- by electrochemical method," *International Journal of Electrochemical Science*, vol. 8, no. 7, pp. 9308–9316, 2013.
- [3] A. E. A. Hermas, M. A. Salam, and S. S. Al-Juaid, "In situ electrochemical preparation of multi-walled carbon nanotubes/polyaniline composite on the stainless steel," *Progress in Organic Coatings*, vol. 76, no. 12, pp. 1810–1813, 2013.
 - [4] M. Behpour and N. Mohammadi, "Investigation of inhibition properties of aromatic thiol self-assembled monolayer for corrosion protection," *Corrosion Science*, vol. 65, pp. 331–339, 2012.
 - [5] A. B. Chaudhari, A. Anand, S. D. Rajput, R. D. Kulkarni, and V. V. Gite, "Synthesis, characterization and application of *Azadirachta indica juss* (neem oil) fatty amides (AIJFA) based polyurethanes coatings: a renewable novel approach," *Progress in Organic Coatings*, vol. 76, no. 12, pp. 1779–1785, 2013.
 - [6] A. Zomorodian, M. P. Garcia, T. M. E. Silva, J. C. S. Fernandes, M. H. Fernandes, and M. F. Montemor, "Corrosion resistance of a composite polymeric coating applied on biodegradable AZ31 magnesium alloy," *Acta Biomaterialia*, vol. 9, no. 10, pp. 8660–8670, 2013.
 - [7] N. Ostrowski, B. Lee, N. Enick et al., "Corrosion protection and improved cytocompatibility of biodegradable polymeric layer-by-layer coatings on AZ31 magnesium alloys," *Acta Biomaterialia*, vol. 9, no. 10, pp. 8704–8713, 2013.
 - [8] S. M. Mirabedini and A. Kiamanesh, "The effect of micro and nano-sized particles on mechanical and adhesion properties of a clear polyester powder coating," *Progress in Organic Coatings*, vol. 76, no. 11, pp. 1625–1632, 2013.
 - [9] R. Verker, E. Grossman, and N. Eliaz, "Erosion of POSS-polyimide films under hypervelocity impact and atomic oxygen: the role of mechanical properties at elevated temperatures," *Acta Materialia*, vol. 57, no. 4, pp. 1112–1119, 2009.
 - [10] Y. Y. Sun, X. Zhou, Y. Q. Liu, G. Z. Zhao, and Y. Jiang, "Effect of magnetic nanoparticles on the properties of magnetic rubber," *Materials Research Bulletin*, vol. 45, no. 7, pp. 878–881, 2010.
 - [11] M. M. Shokrieh, M. R. Hosseinkhani, M. R. Naimi-Jamal, and H. Tourani, "Nanoindentation and nanoscratch investigations on graphene-based nanocomposites," *Polymer Testing*, vol. 32, no. 1, pp. 45–51, 2013.
 - [12] T. Kanai, T. K. Mahato, and D. Kumar, "Synthesis and characterization of novel silicone acrylate-soya alkyd resin as binder for long life exterior coatings," *Progress in Organic Coatings*, vol. 58, no. 4, pp. 259–264, 2007.
 - [13] Y. J. Zhang, H. J. Chi, W. H. Zhang et al., "Highly efficient adsorption of copper ions by a PVP-reduced graphene oxide based on a new adsorptions mechanism," *Nano-Micro Letters*, vol. 6, no. 1, pp. 80–87, 2014.
 - [14] C. K. Huang, W. M. Lou, C. J. Tsai, T.-C. Wu, and H.-Y. Lin, "Mechanical properties of polymer thin film measured by the bulge test," *Thin Solid Films*, vol. 515, no. 18, pp. 7222–7226, 2007.
 - [15] W. J. Liao, A. J. Gu, G. Z. Liang, and L. Yuan, "New high performance transparent UV-curable poly(methyl methacrylate) grafted ZnO/silicone-acrylate resin composites with simultaneously improved integrated performance," *Colloids and Surfaces A: Physicochemical and Engineering Aspects*, vol. 396, pp. 74–82, 2012.
 - [16] M. K. Small and W. D. Nix, "Analysis of the accuracy of the bulge test in determining the mechanical properties of thin films," *Journal of Materials Research*, vol. 7, no. 6, pp. 1553–1563, 1992.
 - [17] H. M. Jensen, "The blister test for interface toughness measurement," *Engineering Fracture Mechanics*, vol. 40, no. 3, pp. 475–486, 1991.
 - [18] J. M. Yeh, H. Y. Huang, C. L. Chen, W. F. Su, and Y. H. Yu, "Siloxane-modified epoxy resin-clay nanocomposite coatings with advanced anticorrosive properties prepared by a solution dispersion approach," *Surface and Coatings Technology*, vol. 200, no. 8, pp. 2753–2763, 2006.
 - [19] S. A. Shojaei, A. Zandiatashbar, N. Koratkar, and D. A. Lucca, "Raman spectroscopic imaging of graphene dispersion in polymer composites," *Carbon*, vol. 62, pp. 510–513, 2013.
 - [20] C. F. Matos, F. Galembeck, and A. J. G. Zarbin, "Multifunctional and environmentally friendly nanocomposites between natural rubber and graphene or graphene oxide," *Carbon*, vol. 78, pp. 469–479, 2014.
 - [21] S. G. Prolongo, A. Jimenez-Suarez, R. Moriche, and A. Ureña, "In situ processing of epoxy composites reinforced with graphene nanoplatelets," *Composites Science and Technology*, vol. 86, pp. 185–191, 2013.
 - [22] Y. Wang, Z. X. Shi, and J. Yin, "Kevlar oligomer functionalized graphene for polymer composites," *Polymer*, vol. 52, no. 16, pp. 3661–3670, 2011.
 - [23] M. Cano, U. Khan, T. Sainsbury et al., "Improving the mechanical properties of graphene oxide based materials by covalent attachment of polymer chains," *Carbon*, vol. 52, pp. 363–371, 2013.
 - [24] J. Singh-Beemat and J. O. Iroh, "Effect of clay on the corrosion inhibition and dynamic mechanical properties of epoxy ester-polyurea-polysiloxane hybrid coatings," *Polymer Engineering & Science*, vol. 52, no. 12, pp. 2611–2619, 2012.
 - [25] F. Khelifa, M.-E. Druart, Y. Habibi et al., "Sol-gel incorporation of silica nanofillers for tuning the anti-corrosion protection of acrylate-based coatings," *Progress in Organic Coatings*, vol. 76, no. 5, pp. 900–911, 2013.
 - [26] D. Prasai, J. C. Tuberquia, R. R. Harl, G. K. Jennings, and K. I. Bolotin, "Graphene: corrosion-inhibiting coating," *ACS Nano*, vol. 6, no. 2, pp. 1102–1108, 2012.
 - [27] P. K. Nayak, C.-J. Hsu, S.-C. Wang, J. C. Sung, and J.-L. Huang, "Graphene coated Ni films: a protective coating," *Thin Solid Films*, vol. 529, pp. 312–316, 2013.
 - [28] W. Zhang, M. Yi, Z. G. Shen, X. H. Zhao, X. J. Zhang, and S. L. Ma, "Graphene-reinforced epoxy resin with enhanced atomic oxygen erosion resistance," *Journal of Materials Science*, vol. 48, no. 6, pp. 2416–2423, 2013.

Research Article

Investigation of Theoretical Models for the Elastic Stiffness of Nanoparticle-Modified Polymer Composites

T. Thorvaldsen,¹ B. B. Johnsen,¹ T. Olsen,¹ and F. K. Hansen^{1,2}

¹Norwegian Defence Research Establishment (FFI), P.O. Box 25, 2027 Kjeller, Norway

²Department of Chemistry, University of Oslo, P.O. Box 1033 Blindern, 0315 Oslo, Norway

Correspondence should be addressed to T. Thorvaldsen; tom.thorvaldsen@ffi.no

Received 19 May 2015; Accepted 21 July 2015

Academic Editor: Abbas S. Milani

Copyright © 2015 T. Thorvaldsen et al. This is an open access article distributed under the Creative Commons Attribution License, which permits unrestricted use, distribution, and reproduction in any medium, provided the original work is properly cited.

Mathematical models are investigated and suggested for the calculation of the elastic stiffness of polymer nanocomposites. Particular emphasis is placed on the effect on the elastic stiffness from agglomerates and the particle interphase properties. The multiphase Mori-Tanaka model and an interphase model are considered as two relevant models. These models only include and require the designation of a few system independent parameters with a clear physical meaning. Extensions of the models are also presented. The model calculations are compared to results from other models, as well as experimental data for different nanocomposites. For nanocomposites with spherical particles and with fiber-like particles, the suggested models are found to be the most flexible ones and are applicable to estimate the stiffness increase of nanocomposites for both low and high particle volume fractions. The suggested theoretical models can hence be considered as a general multiscale “model toolbox” for analysis of various nanocomposites.

1. Introduction

Polymers are widely used in engineering applications, such as in adhesives and in fiber-reinforced composites, where it constitutes the continuous phase. Model analysis of lightweight materials is becoming more important in the design, development, and analysis of novel and complex structures. There is often a desire or need to improve the mechanical properties of the polymers, especially for advanced high-performance applications. The traditional approach has been to add particulate inclusions of microsize, such as inorganic or rubber particles, to the polymers. In recent years, however, a lot of effort has gone into investigating the effect of adding nanosized inclusions [1–3]. A range of nanosized inclusions with different shape and chemical composition has been investigated, such as nanoclay, nanosilica, carbon nanotubes (CNTs), and carbon nanofibers (CNFs). Since the required loading level of the nanoparticles in the polymer is much lower than that for inclusions of microsize, many of the intrinsic properties of the polymer will be retained after the addition of nanoparticles.

One mechanical property that is of significant interest is the nanocomposite elastic stiffness, that is, Young's modulus of the nanocomposite. Most of the commonly used inclusions have a higher elastic modulus than the polymer itself and may therefore contribute to an increased elastic stiffness. The elastic stiffness of a nanocomposite material will, among others, depend on the type, orientation, and the volume fraction of the nanoparticles (assuming that the remaining constituents and the production process are kept constant).

The macroscopic nanocomposite material parameters are required in finite element (FE) modeling, among others. There may be a need for FE modeling of the nanocomposite itself or of a composite material where the nanomodified polymer constitutes the matrix of a continuous fiber-reinforced material. It would therefore be of interest to establish a set of mathematical models that can be used to calculate the macroscopic elastic stiffness of various nanoparticle-reinforced polymer composites.

For the models to be able to handle inclusions of various geometries, they must be flexible, while at the same time giving accurate predictions. In practice, the nanocomposite

structure on the microlevel may be difficult to understand in detail. A detailed microstructural understanding may, however, not be required on a macroscopic level. Therefore, the mathematical models should have model parameters with physical meaning, without being directly system dependent, but they should still be sophisticated enough to give an accurate estimate and to predict the behavior observed in experimental testing.

The main aim of this work is to identify and establish flexible and system independent mathematical model tools for the prediction of the elastic stiffness of multiphase nanocomposites. The influence from the interphase around the nanoparticles and the influence from agglomerates are two effects that are of high interest to model for advanced and high-performance nanocomposites. Both effects will depend on the type of polymer, type of inclusion, loading level of the inclusion, and the processing conditions, and they thus have a practical interest for various nanoparticle/polymer systems. The main contribution from this work will therefore be more on defining a “model toolbox” rather than presenting new models for relevant nanocomposites. After the models are established and described, the model calculations are compared to experimental test data.

2. Mathematical Models

2.1. Nanoparticle/Polymer Characteristics. To actually increase, in this case, the elastic stiffness of a polymer material using particles of nanosize, several factors need to be considered and optimized. First of all, the nanoparticles are very small and therefore have a very large surface compared to larger particles; the surface area is inversely proportional to the particle size. The large surface area is, however, only available if the particles are well dispersed in the polymer. A good dispersion of the particles is believed to be a crucial requirement for obtaining a significant stiffness increase. If the particles form agglomerates, the inclusion phase will act more as defects/impurities in the homogenous polymer, which may instead reduce the bulk elastic stiffness [4, 5]. For nanocomposites with well-dispersed particles, significant increase of the stiffness (and also other properties, such as the toughness) is often explained by interphase effects. A precise description of the mechanical properties and behavior of the interphase is very challenging. Zhang et al. [6] describe these effects as the formation of a “three-dimensional physical network of interphase in a polymer matrix.” For the interphase, there may be other chemical and physical properties than in the bulk matrix, with differences in, among others, the polymer morphology and chain conformation [7], as well as the adhesive properties between the particle and the matrix. Several factors have been shown to affect the binding properties, such as the functionalization or surface treatment of the particles [8] and/or the choice of curing agent [9]. The stiffness of the composite is, furthermore, depending on the geometry and the orientation of the particles. Particles, where the size in one direction is significantly different from the others, such as for CNTs and CNFs, will introduce directional dependent changes in stiffness even for particles considered as isotropic.

Also, composites with curved fiber-like particles (i.e., with waviness) have been reported to give a lower stiffness compared to composites with straight fiber-like particles [10].

With a relatively large set of properties, partly inter-related, that will affect and alter the elastic stiffness of a given nanoparticle/polymer system, a study purely based on experiments will soon become too complex, time consuming, and expensive. As mentioned above, the understanding and development of new nanocomposites will therefore benefit from having flexible and accurate mathematical models on macrolevel with only a few model parameters to vary. This set of models will then function as the multiscale mathematical “model toolbox” for understanding the behavior of the nanocomposites. It is, however, important to have a strong coupling to experimental test results for verification of the models.

2.2. Modeling Approaches. Fisher and Brinson [10] refer to two main mathematical multiscale modeling approaches for nanocomposites, that is, the “top-down” and the “bottom-up” approach. In the “bottom-up” approach, one starts out with the atomistic structure of the nanoreinforcements and the matrix. Typical model techniques are quantum mechanics, molecular dynamics, and Monte-Carlo simulations [10, 11]. These simulations end up in fairly large systems to be solved for only a small part of the composite material, for example, a single CNT attached to a relatively short polymer chain. The output from these calculations should then be representative for the entire composite. Moreover, these simulations are very time consuming, even with large computing resources available.

The “top-down” approach, on the other hand, is based on continuum mechanics, where the polymer and the nano- and microinclusions are treated as continuum elements. The nanocomposite models often use short-fiber models and laminate theory [12] as a starting point. Equivalent models are then established for particles of smaller size. Additional effects, such as interphase effects, are often incorporated in the equivalent models, since these effects seem to be more significant when reducing the size of the particle. One main benefit of the “top-down” approach is that one is able to calculate for a larger part of the composite material (often referred to as a representative volume entity) to estimate the macroscopic properties of the materials.

Due to the size of the nanoparticle filler material, care must be taken when applying the continuum mechanics approach since the structure and interactions at the atomistic level are essential for a precise description of the mechanical properties. For this study, the “top-down” approach, employing continuum mechanics, is, however, assumed to be a valid approach.

2.3. Analytical Models. Several analytical models for the elastic stiffness of nanocomposites are based on the pioneer work by Cox [13]. Rule of mixtures models specially designed for nanocomposites with nonspherical particle geometry have also been presented [14]. Moreover, to include a random orientation of the particles, models for weighting of the properties for the different orientations have been defined,

for example [12]. Approaches employing laminate theory in describing the macroscopic properties of the composite have also been considered; see, for example, [15] and the references therein.

Most of these more “traditional” short-fiber based models assume a perfect dispersion of the particles in the matrix, that is, one inclusion phase in addition to the matrix phase, and a no-slip boundary condition at the particle-matrix interface. Moreover, the traditional models are often developed for a specific nanocomposite, that is, one type of nanoparticle with a given geometry, embedded in a given polymer system. The model parameters are then specific to the particular nanoparticle/polymer system and may not be transmissible to other nanocomposites. More flexible models with less system dependent parameters are therefore appropriate to establish.

In the following, a set of more flexible models for nanocomposites are described: the Mori-Tanaka approach and an interphase model. For comparison, the Halpin-Tsai equation and a slip/no-slip model are also included since these latter models are often applied in comparison with experimental data. It should also be mentioned at this point that expressions based on the Mori-Tanaka method have been established for specific nanocomposites and applied for comparison with experimental results [16–22], but, again, these expressions are not as flexible as the more general multiphase model.

2.3.1. The Halpin-Tsai Equation. For aligned particles, the Halpin-Tsai equations, which are based on empirical data, are often applied [23–26]. For the special case of spherical particles, these equations are reported in the literature to give a reliable estimate for the stiffness properties of the nanocomposite and are often applied for comparison with experimental test results. The modified version of the Halpin-Tsai equations has also been presented, including an orientation factor β that takes into account the randomness of discontinuous fibers.

The modified version of the Halpin-Tsai equation for the *longitudinal* elastic modulus can be expressed as [27, 28]

$$E_C = \frac{1 + \alpha\eta V_f}{1 + \eta V_f} E_m, \quad (1)$$

$$\eta = \frac{(\beta E_f/E_m) - 1}{(\beta E_f/E_m) + 2\alpha},$$

where in the above expression E_C is the elastic stiffness of the composite, E_f and E_m are the elastic stiffness of the inclusions and the matrix, respectively, and $\alpha = l/d$ is the aspect ratio, l being the length and d being the diameter of the particle. In the original Halpin-Tsai equation, β equals unity. For composites with a three-dimensional random orientation of fiber-like particles (where $l \neq d$), $\beta = 1/6$ is used.

2.3.2. The Mori-Tanaka Method. To include more than one inclusion phase, for example, the combination of dispersed nanoparticles and voids/agglomerates, or a second type of particle with other elastic properties and/or a different

geometric shape, more general multiphase models are established. The Mori-Tanaka method is one such attempt [29–31], which also has been reported to agree well with experimental results; see, for example, [10] and the references therein. Different model variants based on the Mori-Tanaka approach can be found in the literature; see, for example, [32] for a review.

The composite elastic stiffness C_C in the Mori-Tanaka model for a multiphase composite with *unidirectionally aligned inclusions* can generally, following the derivation in [10], be expressed as

$$C_C = V_0 C_0 A_0 + \sum_{r=1}^{N-1} V_r C_r A_r$$

$$= \left(V_0 C_0 + \sum_{r=1}^{N-1} V_r C_r A_r^{\text{dil}} \right) \left(V_0 I + \sum_{r=1}^{N-1} V_r A_r^{\text{dil}} \right)^{-1} \quad (2)$$

$$= \left(V_0 C_0 + \sum_{r=1}^{N-1} V_r C_r A_r^{\text{dil}} \right) A_0,$$

where

$$A_r^{\text{dil}} = [I + S_r C_r^{-1} (C_0 - C_r)]^{-1},$$

$$A_0 = \left[V_0 I + \sum_{r=1}^{N-1} V_r A_r^{\text{dil}} \right]^{-1}, \quad (3)$$

$$A_r = A_r^{\text{dil}} A_0.$$

In the above expressions, phase 0 is the continuous and homogeneous matrix phase, and phases 1 to $N - 1$ are the inclusion phases. Moreover, V_0 is the volume fraction of the matrix phase, C_0 contains the stiffness properties of the matrix phase, V_r is the volume fraction of the r th inclusion phase, and C_r contains the stiffness properties of the r th inclusion phase. The quantity I is the identity matrix and S_r is the (second-order) Eshelby tensor for the r th inclusion phase [30, 31]. For composites where the particles can be modeled as having a spheroidal shape (e.g., spherical, oblate, or prolate shape) and included in a homogeneous infinite matrix, the Eshelby tensor is constant. Expressions for the Eshelby tensor for relevant spheroidal inclusion geometries can be found in the literature, for example, [18, 22, 33].

For the special case of a two-phase composite, including the matrix (phase 0) and the nanoparticles (phase 1), the stiffness relation in (2) can be expressed as

$$C_C = (V_m C_m + V_p C_p A_p^{\text{dil}}) (V_m I + V_p A_p^{\text{dil}})^{-1}, \quad (4)$$

where now m indicates the matrix phase and p indicates the inclusion phase. Furthermore, V_m is the volume fraction of the matrix, V_p is the volume fraction of the inclusions, C_m is the stiffness matrix of the matrix, C_p is the stiffness matrix of the inclusions, I is the identity matrix, and

$$A_p^{\text{dil}} = [I + S_p C_p^{-1} (C_m - C_p)]^{-1}, \quad (5)$$

where S_p is the (second-order) Eshelby tensor for the inclusion phase.

The Mori-Tanaka model for a multiphase composite with *randomly oriented inclusions* can in a similar way be expressed as

$$\begin{aligned} C_{C,\text{random}} &= \left(V_0 C_0 + \sum_{r=1}^{N-1} V_r \{C_r A_r^{\text{dil}}\} \right) \left(V_0 I + \sum_{r=1}^{N-1} V_r A_r^{\text{dil}} \right)^{-1} \quad (6) \\ &= \left(V_0 C_0 + \sum_{r=1}^{N-1} V_r \{C_r A_r^{\text{dil}}\} \right) A_0, \end{aligned}$$

where the curly brackets indicate orientational averaging of all possible orientations, as described and shown in [10] (and also in [34] for another orientation of the local axes of the inclusion compared to that used in [10]). In the same way as for aligned inclusions, the elastic stiffness may for a two-phase composite be written as

$$C_{C,\text{random}} = \left(V_m C_m + V_p \{C_p A_p^{\text{dil}}\} \right) \left(V_m I + V_p A_p^{\text{dil}} \right)^{-1}. \quad (7)$$

For the special case of a three-phase composite, the contribution from the second inclusion phase is added to the expressions for aligned and random oriented composites, respectively.

An extension of the above model, also taking into account the curvature (waviness) of the fiber-like particles, has been included by performing a finite element method model calculation for a single curved fiber-like particle surrounded by matrix [10, 35]. Curved fiber-like particles have a reduced stiffness contribution to the composite compared to straight fiber-like particles.

2.3.3. Interphase Models. As for the rule of mixtures and short-fiber composite expressions described above, the Mori-Tanaka method assumes a no-slip condition at the interface between the particles and the surrounding matrix. Such an interface interaction condition may not be a correct description for all nanoparticle/polymer systems.

One approach for allowing a slippage at the interface is presented by Lewis and Nielsen [36] and McGee and McGulough [37]. In their model, the generalized Einstein coefficient (k_E) is altered for the “no-slip” and “slippage” conditions. This model parameter, however, has to be estimated for each nanoparticle/polymer system, which makes the model less flexible for estimating the elastic stiffness of different systems.

As an alternative approach, it can be assumed that the binding characteristics can be expressed in the form of an elastic stiffness for the interphase surrounding the particles, that is, a “second matrix phase.” The stiffness will typically vary (radially) through the interphase, with a smooth transition from the particle surface to the surrounding bulk polymer. As pointed out by Fornes and Paul [7], when employing a continuum mechanics approach, one should assume that each constituent material in the composite does not affect or alter the properties of the other constituents. The interphase should thus be defined as a geometrically

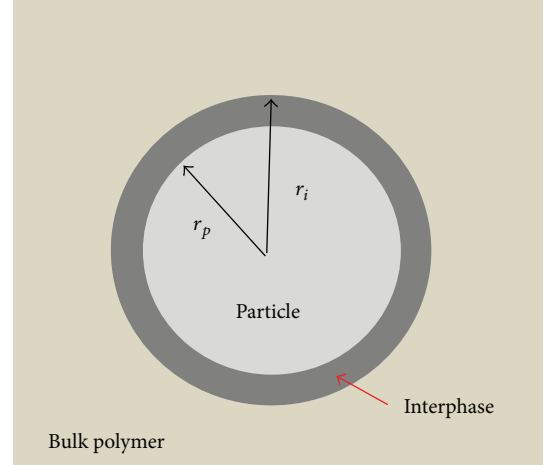


FIGURE 1: Representative volume entity (RVE) for the particle with interphase. The radius of the particles is r_p , whereas the radius of the interphase is r_i , $r_i \geq r_p$.

well-defined region with given elastic properties. A high interphase elastic stiffness indicates good bonding and less flexibility to deform when loaded, whereas a lower inclusion phase elastic stiffness indicates a weaker bonding with more flexibility to deform when loaded.

Measurements of the interphase elastic properties have been done, for example [38]. Since it may be difficult to perform stiffness measurements of the interphase without including the stiffness of the particle itself, molecular model calculations have instead been applied for estimating the interphase properties, for example [39]. Furthermore, the interphase properties may vary as a function of the volume fraction of nanoparticles in the composite. This change in interphase properties may thus indicate a variation in the thickness of the interphase surrounding the particles. Alternatively, the variation of the properties in the interphase can be due to variation in elastic stiffness. Tuning the elastic stiffness and the interphase thickness can therefore give an adequate description of the interphase properties and behavior. The interphase properties are discussed further in Section 4.1.

An effective interphase model has been presented by Odegard et al. [39, 40]. In this case, a no-slip condition at the interface between the particle and the interphase and between the interphase and the bulk matrix has been assumed. However, the interphase itself introduces the wanted flexibility. Note that Odegard et al. refer to their model as an “effective interface model.” To the authors’ knowledge and understanding, the *interface* is the surface of the particle being in contact with its surroundings. The *interphase*, on the other hand, is the polymer matrix region surrounding the particle. A sketch is given in Figure 1 for a spherical particle with radius r_p , surrounded by an interphase with thickness $t_i = r_i - r_p$, $r_i \geq r_p$. This latter terminology is also in accordance with Fisher and Brinson [10] and will be employed in this paper.

In the interphase model by Odegard et al., the elastic stiffness of the nanoparticle/polymer composite C_C , where the particles have a surrounding interphase and a bulk matrix phase outside the interphase, can be expressed as

$$C_C = C_m + \left[(V_p + V_i) (C_i - C_m) A_{pi} + V_p (C_p - C_i) A_p \right] \cdot \left[V_m I + (V_p + V_i) A_{pi} \right]^{-1}, \quad (8)$$

where in this case

$$A_p = I - S_p \left[S_p + (C_p - C_m)^{-1} C_m \right]^{-1},$$

$$A_{pi} = I - S_p \left\{ \frac{V_p}{V_i + V_p} \left[S_p + (C_p - C_m)^{-1} C_m \right]^{-1} + \frac{V_i}{V_i + V_p} \left[S_p + (C_i - C_m)^{-1} C_m \right]^{-1} \right\}. \quad (9)$$

In the same way as for the Mori-Tanaka model described in the previous section, m indicates the matrix phase and p indicates the inclusion phase, whereas i indicates the interphase. Furthermore, V_m is the volume fraction of the matrix, V_p is the volume fraction of the inclusions, and V_i is the volume fraction of the interphase. Moreover, C_m is the stiffness matrix of the matrix, C_p is the stiffness matrix of the inclusions, C_i is the stiffness matrix of the interphase, and I is the identity matrix. It should at this point also be noted that the geometric properties of the interphase are not explicitly given in the stiffness expressions in (8) and (9), but implicitly through the volume fraction calculations of the different constituents.

In the model presented by Odegard et al., the particles are assumed to be spherical (and thus aligned), and S_p hence refers to the Eshelby tensor for spheres. An extension of the Odegard et al. model is to include spheroidal shapes different from spheres (i.e., prolate and oblate spheroidal) and also random orientation of the inclusions. Including other spheroidal shapes is easily done by replacing the Eshelby tensor for spheres with the tensor for another spheroidal shaped inclusion. The random distribution may be more complex. In this paper, it is assumed that the same “averaging strategy” as was performed for the multiphase Mori-Tanaka model is applicable. By comparing the terms in the Mori-Tanaka model and the effective interphase model, we find the terms that are required to be orientationally averaged. The stiffness for such a composite can then be expressed as

$$C_C = C_m + \left[(V_p + V_i) \left\{ (C_i - C_m) A_{pi} \right\} + V_p \left\{ (C_p - C_i) A_p \right\} \right] \cdot \left[V_m I + (V_p + V_i) A_{pi} \right]^{-1}, \quad (10)$$

where the curly brackets indicate the average of the quantity over all possible orientations. To the authors' knowledge, the model extensions have not been published elsewhere.

2.3.4. Agglomerate Models. Agglomeration is highly relevant for nanocomposites with nonspherical particles since the particles in such cases are more likely to be entangled prior to the dispersion process. This situation can be handled by the multi-phase Mori-Tanaka model described in Section 2.3.2, by assuming that one of the particulate phases is an agglomerate phase.

Special models are also established for certain composites including a combination of free and agglomerated particles. As a first example, a model for composites with carbon nanotubes (CNTs) in a polymer system has been presented by Shi et al. [41, 42]. In their work, models are presented both for perfectly dispersed CNTs and for composites with a combination of dispersed particles and agglomerates of particles. In both approaches, the Mori-Tanaka method is employed. In their agglomerate model, the areas with concentrated CNTs are considered to be spherical inclusions with different elastic properties compared to the surrounding material. Two parameters are employed for describing the agglomeration. Based on the Voigt model, found in [43], and assuming that both the matrix and the CNTs have isotropic material properties, expressions for the elastic properties of the inclusions and the material outside the inclusions are established.

As a second example, Gershon et al. [5] presented an agglomerate model for CNFs in a polymer system. In their model, expressions are given for the volume fraction of agglomerated CNFs

$$V_{\text{CNFagglomerate}} = \frac{E_{\text{agglomerate}} V_{\text{agglomerate}}}{E_{\text{CNF}}}, \quad (11)$$

for the volume fraction of dispersed CNFs in the polymer, referred to as the matrix,

$$V_{\text{CNFmatrix}} = \frac{E_{\text{matrix}} - E_{\text{polymer}}}{E_{\text{CNF}} - E_{\text{polymer}}}, \quad (12)$$

and finally for the composite

$$E_{\text{composite}} = \frac{1}{(1 - V_{\text{agglomerate}}) / E_{\text{matrix}} + V_{\text{agglomerate}} / E_{\text{agglomerate}}}. \quad (13)$$

Experimental data for Young's modulus of the matrix, that is, the polymer with free and dispersed CNFs, and Young's modulus for the agglomerates are required. The values vary as a function of the volume fraction of CNFs.

3. Experimental Work

Experimental work was conducted with the main aim of comparing the experimental results with the model calculations (see Section 5) and to obtain realistic model parameters. In this work, the elastic stiffness variation of two silica/epoxy nanocomposite materials, upon increasing nanosilica content, was determined.

3.1. Materials. Two different epoxy polymers were investigated in this work: one amine-cured and one anhydride-cured system [44]. The amine-cured polymer system was Araldite LY 556/XB 3473, while the anhydride-cured polymer system was Araldite LY 556/Aradur 917/Accelerator DY 070. Both systems are from Huntsman. LY 556 is a standard bisphenol A based epoxy resin with an epoxy equivalent weight (EEW) of 183–189 g/eq. XB 3473 is an amine hardener containing two different diamines. The active hydrogen equivalent weight (AHEW) of XB 3473 is ≈ 43 g/eq. Aradur 917 is a methyltetrahydrophthalic acid anhydride hardener with an AHEW of 166 g/eq, whereas DY 070 is an imidazole accelerator.

A sol of silica (SiO_2) nanoparticles in an epoxy resin was employed to produce the silica/epoxy nanocomposites. The Nanopox F400 was supplied by Evonik Hanse, Geesthacht, Germany. The silica phase in Nanopox F400 consists of surface-modified silica spheres with an average particle diameter of 20 nm and a narrow particle size distribution. The silica content is 40 wt%, and the density of the silica ρ_r is 2100 kg/m^3 [45]. The silica particles have an elastic stiffness of 70 GPa and a Poisson ratio of 0.20. The epoxy phase is a bisphenol A diglycidyl ether, and the EEW for Nanopox F400 is 299 g/eq. Nanopox F400 has a comparatively low viscosity, due to the low degree of agglomeration of the nanoparticles in the resin.

3.2. Specimen Preparation. Plates of the neat epoxy polymers were prepared by first mixing stoichiometric ratios of epoxy resin and hardener (and the accelerator in the case of the anhydride-cured system). After mixing, the blends were stirred manually using a spatula, thereafter heated to 80°C to lower the viscosity, and then stirred thoroughly again. Finally, the blends were vacuum degassed and then cast in a preheated metal mold that had been coated with a release agent. The resulting plate thickness was 4 mm. The curing cycles employed were (1) 2 hours at 120°C , 2 hours at 140°C , and 2 hours at 180°C for the amine-cured system and (2) 4 hours at 80°C and 8 hours at 140°C for the anhydride-cured system.

The procedure for producing plates of the silica/epoxy nanocomposites was similar to that of the neat epoxy polymers, except that Nanopox F400 was also mixed into the blends. Plates with four different loadings of silica for each polymer system were prepared. The cured composite plates were visually observed to be free of air and blisters.

The density of the neat epoxy polymers ρ_m and the nanocomposites ρ_c was measured according to the immersion method described in ASTM D 792-08 [46]. Measurements were conducted on six pieces from each produced plate. The density was in the range from 1160 to 1315 kg/m^3 for the amine-cured system and in the range from 1200 to 1305 kg/m^3 for the anhydride-cured system. Based on the known weight fractions of silica in the nanocomposites, the density measurements were used to calculate the volume fraction V_p .

3.3. Material Characterization. Tensile testing was conducted on dumbbell specimens that were machined from the neat epoxy and silica/epoxy nanocomposite plates. The testing was

conducted according to the relevant ISO standard [47, 48] on a Zwick BZ2.5/TN1S material testing machine, employing specimens of type 1BA. The test speed was 1 mm/min, and the strain was recorded using a clip-gauge extensometer. Values for the tensile modulus of elasticity E_t , the maximum tensile stress, or the tensile strength σ_m , and the maximum elongation, or tensile strain at break ϵ_b , were determined. The tensile modulus E_t was determined from the linear part of the stress-strain curve in the strain range from 0.05% to 0.25%. Average values of six replicate specimens are reported. The ambient temperature during the testing was $23 \pm 1^\circ\text{C}$.

Dynamic mechanical analysis (DMA) was performed on a DMA 2980 Dynamic Mechanical Analyzer from TA Instruments. Rectangular specimens with the dimensions $3 \text{ mm} \times 10 \text{ mm} \times 60 \text{ mm}$ were cut from the produced plates. The analysis was conducted in a three-point bending mode employing a low friction three-point bending clamp with a specimen free length of 50 mm. The oscillation frequency was 1 Hz, the preload force was set to 0.05 N, and the “Force Track” was set to 150%. The heating rate was $3^\circ\text{C}/\text{min}$. The value of the storage modulus, E' , was measured at a temperature of 30°C , and the value of the glass transition temperature T_g of the epoxy polymer is reported as the peak value of the loss modulus, E'' . Average values of three replicate specimens are reported.

3.4. Experimental Test Results

3.4.1. Amine-Cured System. The results from the tensile testing and the DMA of the neat amine-cured epoxy and its silica/epoxy nanocomposites are shown in Table 1. The tensile testing showed a linear increase in the elastic modulus E_t with increasing content of silica. The value increased from 2.61 GPa for the neat epoxy polymer to 3.68 GPa for the composite containing 17.2 vol% (volume fraction $V_f = 0.172$) nanosilica. The tensile strength σ_m remained relatively constant, although the results show that the strength may have been slightly improved at the highest silica contents. The tensile strain at break ϵ_b , on the other hand, is significantly reduced by the addition of the silica nanoparticles. All specimens broke without yield being observed. The DMA also showed a linear increase in the elastic modulus, that is, for the storage modulus E' with increasing silica content. The glass transition temperature T_g remained almost constant at around 186°C , and a small decrease in T_g was observed only for the composite containing the highest amount of silica.

3.4.2. Anhydride-Cured System. The results from the tensile testing and the DMA of the neat anhydride-cured epoxy and its silica/epoxy nanocomposites are shown in Table 2. The elastic modulus E_t increased linearly from 3.03 GPa for the neat epoxy polymer, to 4.15 GPa for the composite containing 12.3 vol% silica (volume fraction $V_f = 0.123$). There was also a gradual increase in the tensile strength σ_m , whereas a minor reduction in the strain at break ϵ_b was observed.

A linear increase for the storage modulus E' was also observed. However, it is noteworthy that for the anhydride-cured system there was also a linear decrease in T_g with increasing silica content. The decrease in T_g was from 155°C

TABLE 1: Material properties of the amine-cured epoxy polymer and silica/epoxy nanocomposites, obtained from tensile testing and DMA testing.

Silica content		Tensile testing			DMA	
wt%	vol%	E_t (GPa)	σ_m (MPa)	ϵ_b (%)	E' (GPa)	T_g (°C)
0.0	0.0	2.61 ± 0.03	69 ± 4	4.8 ± 0.6	2.61 ± 0.03	186 ± 2
6.6	3.7	2.80 ± 0.05	68 ± 2	4.1 ± 0.2	2.87 ± 0.05	186 ± 2
13.4	7.8	3.04 ± 0.07	66 ± 2	3.5 ± 0.3	3.09 ± 0.03	187 ± 1
20.3	12.3	3.31 ± 0.08	69 ± 1	3.3 ± 0.2	3.37 ± 0.06	185 ± 1
27.5	17.2	3.68 ± 0.11	67 ± 4	2.7 ± 0.3	3.70 ± 0.05	182 ± 1

TABLE 2: Material properties of the anhydride-cured epoxy polymer and silica/epoxy nanocomposites, obtained from tensile testing and DMA testing.

Silica content		Tensile testing			DMA	
wt%	vol%	E_t (GPa)	σ_m (MPa)	ϵ_b (%)	E' (GPa)	T_g (°C)
0.0	0.0	3.03 ± 0.07	85 ± 1	5.8 ± 0.5	2.99 ± 0.04	155 ± 0
4.4	2.5	3.28 ± 0.05	89 ± 1	5.7 ± 0.4	3.24 ± 0.04	154 ± 1
9.1	5.4	3.53 ± 0.10	89 ± 2	4.9 ± 0.7	3.41 ± 0.08	151 ± 0
14.2	8.6	3.80 ± 0.09	88 ± 5	4.3 ± 1.1	3.75 ± 0.06	146 ± 1
19.8	12.3	4.15 ± 0.08	93 ± 0	5.1 ± 0.3	3.97 ± 0.10	143 ± 1

to 143°C. It has been shown in the literature that there may be a correlation between the observed T_g and the elastic modulus for neat polymer, for example [49]. In our case, by varying the resin/hardener ratio of the neat anhydride-cured epoxy polymer, we have observed by DMA that a reduction in T_g of 10°C may coincide with an increase of the elastic modulus by 0.15 GPa when there is an excess of hardener, resulting in different crosslink densities of the three-dimensional polymer network. The increased elastic modulus may be explained in terms of free volume, that is, a higher packing of the polymer chains and higher material density as the result of lower crosslink density [10, 49]. For the anhydride-cured nanosilica/epoxy system, this may indicate that nonstoichiometric amounts of hardener have also been used when producing the nanocomposite plates. In addition, this observation indicates that also the state of the epoxy matrix may contribute partly to the elastic modulus of the nanocomposites. A variation in T_g as a result of the presence of silica has also been observed and reported by others [6, 50].

4. Model Parameters

In the next sections, the flexibility, accuracy, and main areas of application for the models described above are discussed. This is done by comparing the model calculations with experimental results for some relevant nanocomposites. Polymer matrix nanocomposites with two different inclusions are then considered: (1) spherical particles (Section 5) and (2) randomly distributed fiber-like particles (Section 6).

Before comparing the model calculations with the experimental results for different composites, the general and system independent model parameters used to describe the stiffness properties of the different nanocomposites are considered.

4.1. Properties of the Interphase Region. As described for the interphase model by Odegard et al. in Section 2.3.3, the interphase is defined as the region surrounding the particles, with different elastic properties compared to the bulk matrix. As shown in Figure 1, we assume that the interphase has a constant thickness t_i and that the radius of the interphase r_i is expressed as

$$r_i = nr_p. \quad (14)$$

The dimensionless parameter n is here denoted as the *interphase thickness factor*. As also pointed out above, the elastic properties are assumed to be constant through the interphase.

The thickness of the interphase is included in the stiffness calculations through the expressions for the volume fractions. For the case of spherical particles, the volume of the particles is given by $v_p = 4/3\pi r_p^3$. From this, the volume of the interphase can be calculated as

$$\begin{aligned} v_i &= \frac{4}{3}\pi (nr_p)^3 - \frac{4}{3}\pi r_p^3 = \frac{4}{3}\pi r_p^3 (n^3 - 1) \\ &= (n^3 - 1)v_p. \end{aligned} \quad (15)$$

Hence, the volume of the interphase is $(n^3 - 1)$ times the volume of the particle. As a consequence of this, the volume fraction of the interphase is $(n^3 - 1)$ times the volume fraction of the particles; that is, $V_i = (n^3 - 1)V_p$. Moreover, the volume fraction of the matrix phase is given as $V_m = 1 - (n^3 - 1)V_p - V_p = 1 - n^3V_p$. For other spheroidal shapes we end up with the same expressions for the volumes and volume fractions; see [10] for the special case of volume fractions for carbon nanotubes in a matrix system.

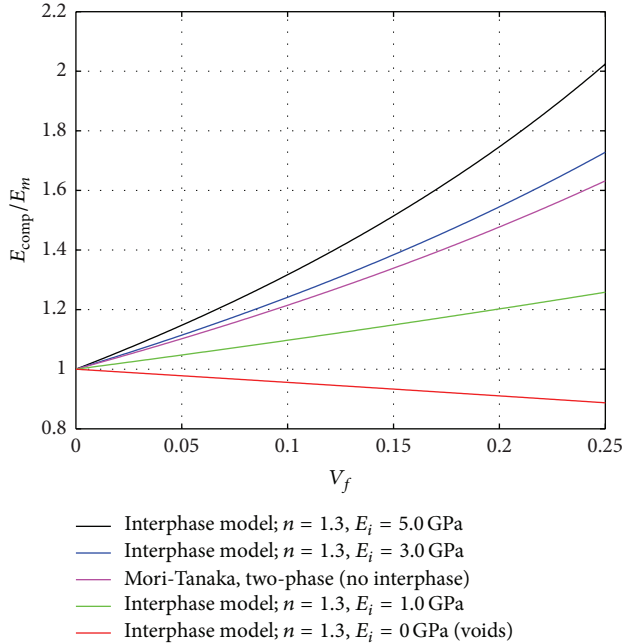


FIGURE 2: Model results for the silica/epoxy composite elastic stiffness. The interphase thickness factor is set to a constant value of 1.3, and the interphase elastic stiffness is varied.

To better explain the effect on the two key model parameters for the interphase (i.e., the interphase thickness factor and the interphase elastic stiffness), we now assume a nanocomposite where the bulk matrix has an elastic stiffness of 2.5 GPa and a Poisson's ratio of 0.35, with a small volume fraction of spherical nanoparticles with an elastic stiffness of 70 GPa (28 times the bulk matrix) and a Poisson's ratio of 0.2. The interphase model is applied in the calculations.

First, the interphase thickness factor is set to a constant value, say 1.3, and the interphase elastic stiffness is varied. An interphase elastic stiffness equal to the bulk matrix stiffness, which is the two-phase Mori-Tanaka model case, is in this case our reference. (Note that an elastic interphase stiffness equal to the bulk matrix stiffness results in inversion of a singular matrix, and, hence, this particular case is outside the area of application for the interphase model.) As can be observed in Figure 2, increasing the elastic stiffness of the interphase region will increase the stiffness of the composite, whereas a reduction of the same stiffness parameter will reduce the composite stiffness. When approaching the case of no interphase elastic stiffness, that is, a polymer with voids, the calculated composite stiffness is reduced to a value below the bulk stiffness.

Second, the stiffness of the interphase is set to a constant value, and the interphase thickness factor is varied. The case $n = 1.0$, that is, no interphase region, is now our reference, and in this case the composite stiffness overlaps the composite stiffness calculated using the two-phase Mori-Tanaka model. If the interphase elastic stiffness is set to 4 GPa, which is a bit higher than the bulk matrix stiffness, but still much lower than the particle inclusion stiffness, from Figure 3 we observe

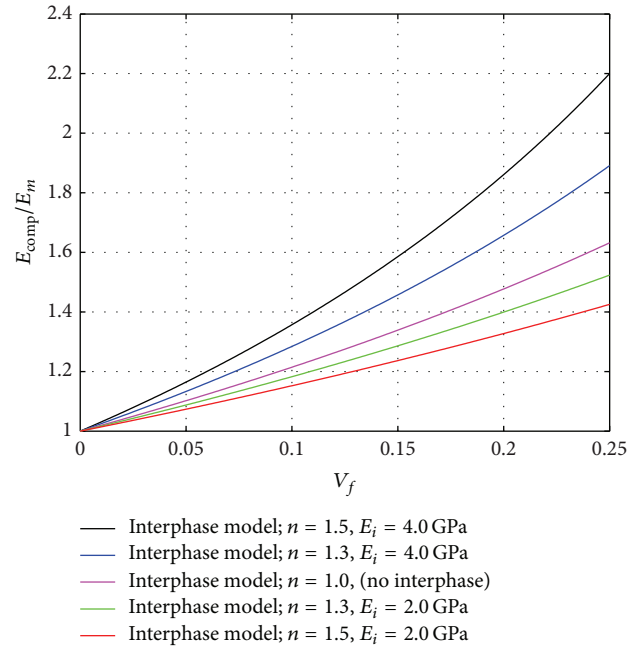


FIGURE 3: Model results for the silica/epoxy composite elastic stiffness. The interphase thickness factor and the interphase elastic stiffness are varied.

that the composite stiffness is increased with increasing n . With a constant interphase elastic stiffness of 2 GPa, which is a bit lower than the bulk matrix stiffness, the composite stiffness is shown to be reduced for increasing n . This seems like a logical behavior and confirms that the model provides the expected trend.

In the examples above, no precise estimate was given for the interphase elastic stiffness, and no restrictions were made for the interphase thickness factor. This will certainly vary for different nanocomposites, but some conclusions can be made. For the model calculations to actually match the stiffness improvement observed experimentally, the interphase elastic stiffness should be higher than the neat matrix stiffness. Also, taking into account the fact that the interphase volume fraction is $(n^3 - 1)$ times the volume fraction of the particles, the interparticle distance sets some restrictions on n [51–53].

For the interparticle distance, two idealized particle packing structures for the case of spherical particles, obtained from simple geometrical considerations taking the interphase into account, are shown in Figure 4. A contour map indicates the minimum distance between layers for each packing, where a negative value indicates particle interphase overlap (which is outside the area of application for the model). In case of hexagonal packing of the particles (Figure 4(a)), the interphase thickness factor should be less than 1.9 for particle volume fractions up to 0.10. In case of simple cubic packing of the particles (Figure 4(b)), the interphase thickness factor should be less than 1.75 for particle volume fractions up to 0.10. In a real situation, something between the two idealized packing structures would be expected. An equivalent plot has also been shown by Karger-Kocsis and Zhang [53] for

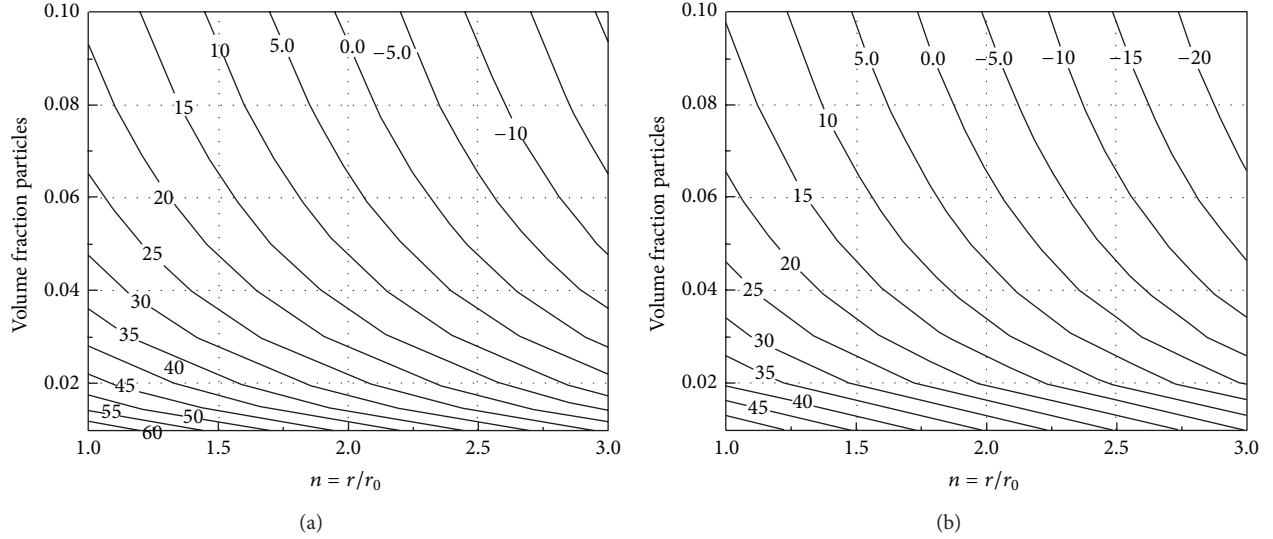


FIGURE 4: Packing structures of spherical particles in 3D. (a) Hexagonal packing; (b) simple cubic packing.

cubic distribution of spherical particles, for different particle diameters.

4.2. Degree of Exfoliation in Agglomerated Composites. For nanocomposites with fiber-like particle inclusions, it is likely that the particles are not fully dispersed and that a second inclusion phase is present in the form of particle agglomerates. In addition, one also needs to take into account the particle orientation distribution; without an enforced flow field as part of the production process, the particles are likely to be randomly oriented. The random orientation is taken care of by the models described above, by integrating over all orientations.

To quantify the amount of agglomerates and the volume fraction of particles inside the agglomerates, the two-parameter model by Shi et al. [41, 42] can be applied. Alternatively, the volume fractions of the dispersed (i.e., free) particles and agglomerates can be estimated using the degree of exfoliation (DOE) φ_{DOE} , which can be expressed as

$$\varphi_{\text{DOE}} = \frac{V_{p,f}}{V_p}, \quad (16)$$

where $V_{p,f}$ is the volume fraction of free particles and V_p is the total volume fraction of particles in the composite. In this latter case, φ_{DOE} can also be expressed by the volume fraction of the particles within the agglomerates of the composite. The DOE for a given nanocomposite can be estimated from a particle size analysis; see [55] for the case of dispersion of multiwall CNTs (MWCNTs) in a liquid solution. The DOE will vary as a function of volume fraction of V_p .

5. Model Results for Spherical Particle Inclusions

Three different nanosilica/epoxy composites are compared with the mathematical models in the following, including the

elastic stiffness results of the amine-cured and anhydride-cured composites given in Tables 1 and 2. For these systems, a perfect dispersion of the spherical silica particles is assumed, and, hence, a two-phase nanocomposite is considered. The stiffness can in this case be estimated from the Halpin-Tsai equation (with $\beta = 1.0$), the two-phase Mori-Tanaka model, and the interphase model. A Poisson's ratio of 0.35 is assumed for the neat epoxy polymers, as well as for the interphase (in the interphase model).

5.1. Results. First, for the amine-cured composite, the three different models are plotted together with the experimental data in Figure 5(a). To try to fit the interphase model results to the experimental data, the interphase thickness factor as a function of silica volume fraction was selected in the range from 1.05 to 1.1; see Figure 5(b). The elastic stiffness of the interphase is in this case set to a constant value of 4.0 GPa. As can be observed, the Halpin-Tsai equation overestimates the elastic stiffness of the composite. However, both the Mori-Tanaka two-phase model and the interphase model estimate the elastic stiffness very well for all volume fractions of silica (provided the selected interphase characteristics are employed for the interphase model). For higher volume fractions, the interphase model with a small interphase thickness resulted in best agreement with the experimental results.

Second, the modeling and experimental results for the anhydride-cured composite are given in Figure 6(a). In this case, again to try to fit with the experimental data, the interphase thickness factor was set much higher and varied between 1.7 and 1.4 as a function of the silica volume fraction; see Figure 6(b). The elastic stiffness of the interphase is also in this case set to a constant value of 4.0 GPa. As can be seen in the figure, the Halpin-Tsai equation and the interphase model estimate the elastic stiffness of the composite very well. The two-phase Mori-Tanaka model, on the other hand, underestimates the elastic stiffness of the composite.

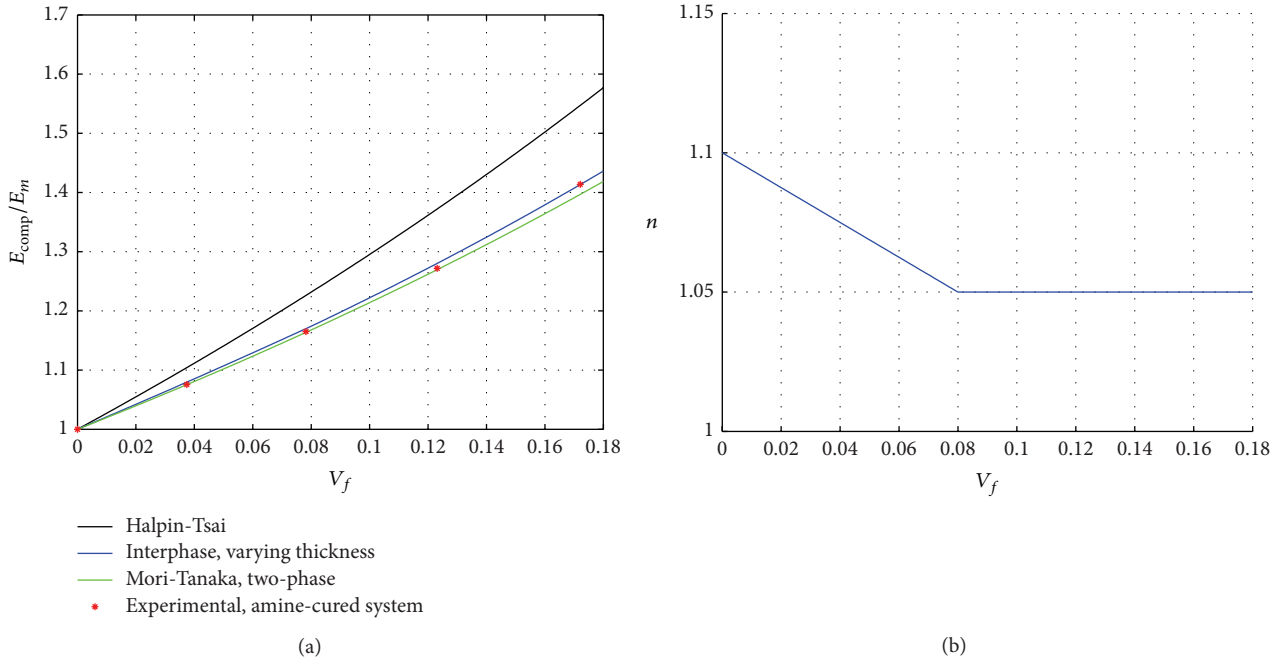


FIGURE 5: Model results and experimental data for the amine-cured nanosilica/epoxy system. (a) Composite elastic stiffness as a function of particle volume fraction; (b) interphase thickness factor.

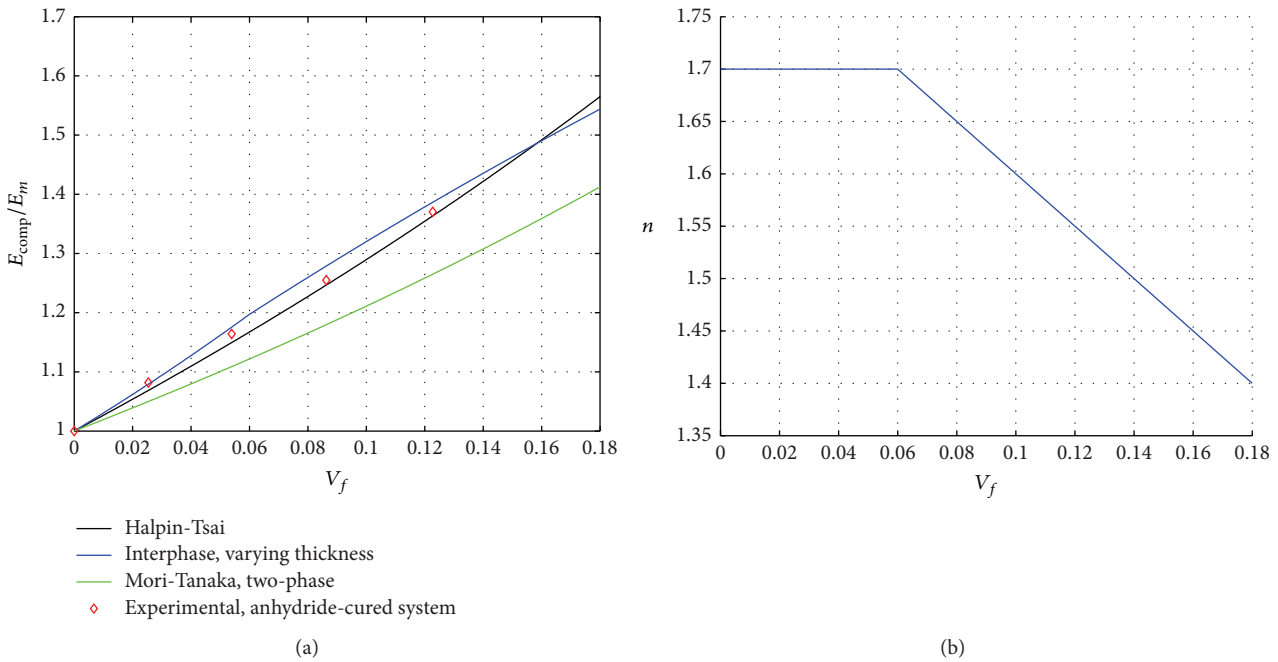


FIGURE 6: Model results and experimental data for the anhydride-cured nanosilica/epoxy system. (a) Composite elastic stiffness as a function of particle volume fraction; (b) interphase thickness factor.

Comparing the above two systems, a much lower interphase thickness factor was selected for the amine-cured composite. Therefore, the effect of selecting a lower and constant interphase thickness factor of 1.3 and varying the

interphase elastic stiffness of the anhydride-cured composite is a relevant case. This is shown in Figure 7. It can be seen that an interphase stiffness between 5.0 and 6.0 GPa agrees well with the experimental data. An elastic stiffness of 4.0 GPa

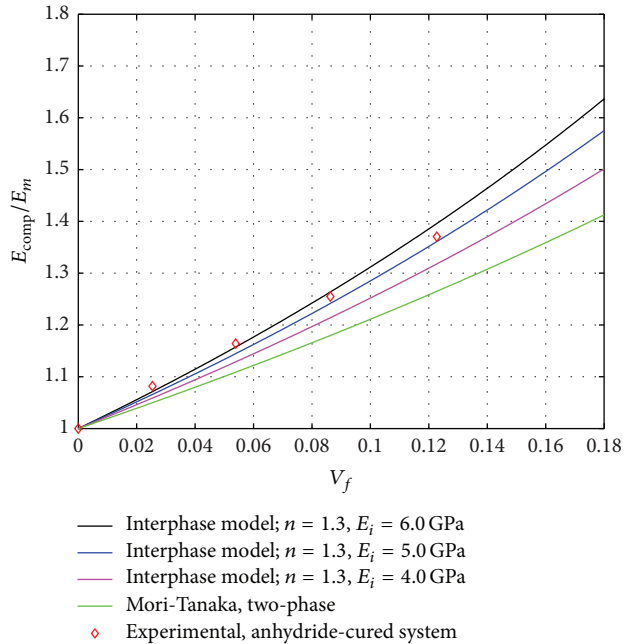


FIGURE 7: Model results and experimental data for the anhydride-cured nanosilica/epoxy system. The interphase thickness factor is set to a constant value of 1.3, and the interphase elastic stiffness is varied.

is observed to underestimate the composite stiffness. The two-phase Mori-Tanaka calculations are unchanged from the previous case and only included here for comparison.

Third, Johnsen et al. [54] reported results for a similar nanosilica/epoxy system. They used the same nanosilica particles, but the polymer was cured with a different anhydride hardener. Their measured composite elastic stiffness was compared to model calculations using the Halpin-Tsai equation, as well as the Lewis-Nielsen model for both no-slip ($k_E = 2.167$) and interfacial slippage ($k_E = 0.837$) conditions. A perfect dispersion of the nanoparticles was assumed. The experimental results and the calculated composite elastic stiffness are shown in Figure 8(a) [54]. In the figure, the results shown have been corrected to a silica density of $\rho_p = 2100 \text{ kg/m}^3$, which is identical to the density used in the above cases; the density applied by Johnsen et al. was $\rho_p = 1800 \text{ kg/m}^3$. The different silica density will affect the silica volume fraction, which again will slightly alter the slope of the elasticity curve. As can be observed in the plot, the Halpin-Tsai equation and the Lewis-Nielsen model with no-slip interface condition give the same stiffness increase for increasing volume fractions. The two models overestimate the stiffness for low volume fractions and overestimate the stiffness for higher volume fractions. The two-phase Mori-Tanaka model and the Lewis-Nielsen model with slippage at the interface underestimate the elastic stiffness for all volume fractions. On the other hand, the calculated elastic stiffness using the interphase model can be tuned (as was done for the above two nanocomposite systems), such that there is an agreement with the experimental results for both low and

high volume fractions. The elastic stiffness of the interphase is in this case set to 5.0 GPa, whereas the interphase thickness factor is varying between 1.6 and 1.2, as shown in Figure 8(b). With a reduced stiffness in the interphase region (i.e., $E_i < E_m$) and constant interphase thickness factor for all volume fractions, the interphase model would have given a similar curve to that of the Lewis-Nielsen model with the “slippage” condition.

In the previous case, the thickness of the interphase for low volume fractions was set to a very large value, which may be unphysical and not according to measurements (e.g., [38]). In the same way as for the anhydride-cured system above, the interphase thickness for the nanosilica/epoxy system from Johnsen et al. is therefore reduced and set to a constant value of 1.3, whereas the interphase elastic stiffness is varied. As can be seen in Figure 9 [54], an interphase stiffness $E_i = 9.0 \text{ GPa}$ agrees well with the available experimental data for low volume fractions. Similarly, an interphase stiffness of $E_i = 4.0 \text{ GPa}$ agrees well with the experimental data for higher volume fractions. The Mori-Tanaka model is included for comparison.

5.2. Discussion. In the results presented above, the extent of the interphase was varied significantly in order to fit the experimental data. It can be argued whether the (selected) values for the interphase thickness factor n are correct or not. However, some data can be found in the literature regarding the extent of the interphase around nanoparticles. According to Antonelli et al. [56], the extent of the interphase was 3 nm for a silica/epoxy system with 17 nm silica particles. For the silica particles used here, this gives a value of $n = 1.15$. Holt et al. [38] studied a silica/poly(2-vinylpyridine) system. They found that the interphase thickness was 4–6 nm for silica particles with a diameter of 30 nm and that it was independent of particle concentration (i.e., particle volume fraction). For 20 nm particles, this results in a value of n in the range from 1.2 to 1.3. Thus, these literature values and the values used in the interphase model are of the same order, although the highest values may be considered unrealistically high. Interphase layer thicknesses of 10 nm, here resulting in a value of n of 1.5, have, however, been reported; see [56] and the references therein.

The two silica/epoxy systems that were tested here (in Section 3) gave different values for the elastic stiffness of the neat epoxy polymer. It follows that the relative increase in elastic stiffness was also different. On the whole, the elastic stiffness was increased relatively more for the anhydride-cured system with the addition of silica, compared to the amine-cured system. The difference between the two systems is likely to be explained by chemical and physical differences, such as the difference in the polymer network structure, as well as differences in interfacial binding properties between the particles and the polymer. As already discussed in Section 3.4.2, T_g of the anhydride-cured system decreases for increasing volume fractions. The same behavior was not observed for the amine-cured system. In addition, DMA measurements of the neat anhydride-cured epoxy polymer showed that the elastic stiffness could be increased when T_g was decreased as a result of nonstoichiometric resin/hardener

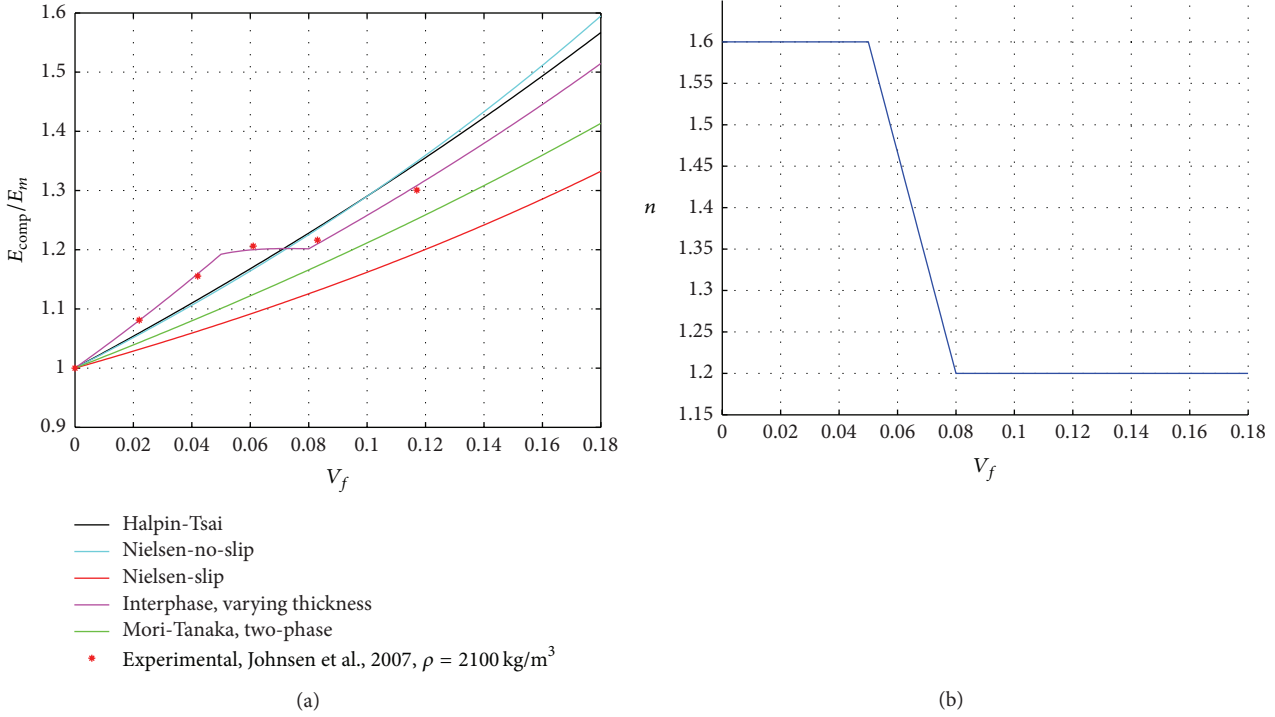


FIGURE 8: Model results and experimental data for the nanosilica/epoxy system in Johnsen et al. [54]. (a) Composite elastic stiffness as a function of particle volume fraction; (b) interphase thickness factor.

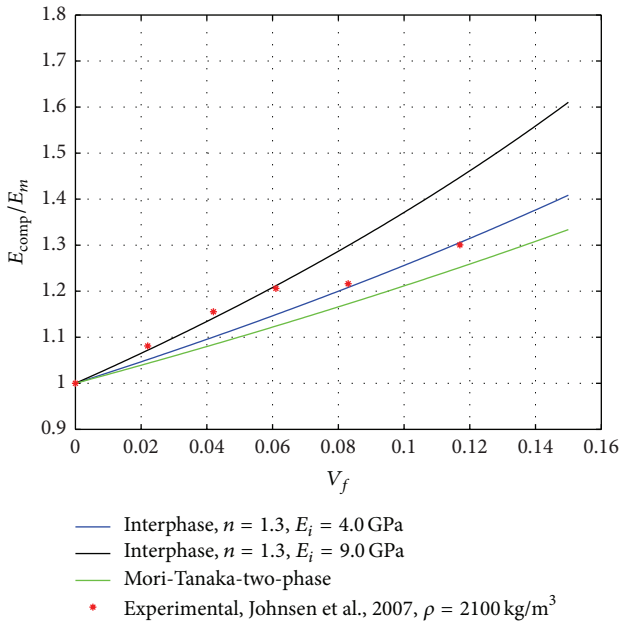


FIGURE 9: Model results and experimental data taken from Johnsen et al. [54]. Composite elastic stiffness of nanosilica/epoxy composite as a function of volume fraction. The interphase thickness factor and the interphase elastic stiffness are varied for the interphase model.

ratios (the elastic stiffness increase was around 0.15 GPa when T_g was decreased by 10°C). Since T_g of the anhydride-cured composite is decreased, it could mean that the elastic stiffness

is also influenced by an altered polymer structure. Hence, the effective increase in elastic stiffness, solely due to the addition of silica, may not be as high as that indicated by the experimental results.

When comparing the experimental results with the mathematical models, it can be presumed that the properties of the interphase region surrounding the particles are different for the amine-cured system and the anhydride-cured system. For the amine-cured system, the two-phase Mori-Tanaka model was found to agree well with the experimental results for all volume fractions. For the interphase model, only a small interphase thickness was required to obtain good agreement with the experimental results. This indicates that the molecular structure of the polymer network is not significantly influenced by the particle inclusions. This is also indicated by the stable T_g values. Moreover, the Halpin-Tsai equation was found to overestimate the stiffness and it did not describe the stiffness properties of the amine-cured system very well, even though a two-phase composite with no-slip condition at the interface between the particle and the polymer is assumed.

For the anhydride system, on the other hand, the stiffness calculated using the Halpin-Tsai equation agrees well with the experimental data, whereas the Mori-Tanaka model underestimated the elastic stiffness. The interphase model was also found to agree well, when assuming an interphase region, with a slightly higher elastic stiffness compared to the bulk matrix. This observation, combined with the observation of the reduction in T_g of the composites, indicates that the polymer network is altered due to the particle inclusions (or possibly also by the mixing ratio of the different components).

Mathematically it should then be plausible to model the stiffness increase by an interphase region with different elastic properties compared to the nonreinforced neat matrix. Since the two-phase Mori-Tanaka model does not include this additional stiffness region, it is predictable that the model underestimates the composite stiffness. However, the calculated stiffness from employing the Halpin-Tsai equation agrees well with the experimental results, even if the properties of the composite are different from what is assumed in the model. The reason for this is at present unknown.

For the system presented by Johnsen et al. [54], the silica particles were assumed to be fully dispersed in the polymer matrix, even for higher concentrations, and T_g of the composite was relatively stable. Thus, the system should be considered as a two-phase system with no significant interphase region surrounding the particles. As reported above, the Halpin-Tsai equation and the Lewis-Nielsen model with no-slip interface condition do not agree very well with the experimental results in this case but provide some kind of average stiffness estimate for all particle concentrations. The Mori-Tanaka model underestimates the stiffness for low volume fractions. For higher volume fractions, on the other hand, there is good agreement. Again, for the interphase model it is possible to vary the model parameters, so that the stiffness is in agreement with the experimental values for all volume fractions included. A plausible explanation is that the elastic properties, in fact, vary as a function of volume fraction, which then can be modeled either by an increased interphase region or by an increase in the elastic stiffness of this region. Finally, the Lewis-Nielsen model with the slippage interface conditions underestimates the elastic stiffness for all volume fractions and, hence, does not seem to mimic the interface conditions in an appropriate way, even though k_E is adjusted to fit the system considered.

6. Model Results for Fiber-Like Particle Inclusions

Fiber-like particle inclusions in polymer systems may require other models than those used for spherical inclusions. First of all, the orientation of the particles needs to be accounted for. Moreover, the particles are often more challenging to disperse, resulting in a second inclusion phase in the form of agglomerates of the particles. Two different nanocomposite systems are considered: (1) a CNF/epoxy composite and (2) a MWCNT/polystyrene composite.

6.1. CNF/Epoxy Composite. A model for a CNF/epoxy composite with agglomerates has been presented by Gershon et al. [5]. The amount of free, randomly orientated CNFs was expressed by the degree of exfoliation (DOE), which is calculated from the volume fractions of CNF in the agglomerates and in the polymer matrix. Based on their DOE curve, Gershon et al. concluded that the modulus of CNF is 30 GPa, even though a value of one order higher was expected. Now, if we instead assume a stiffness value for the CNFs of one order higher, say, 200 GPa, the DOE values are only slightly changed; both sets of values are shown in

Figure 10(b). The latter values should therefore be equally representative as the reported values, at least for defining a continuous DOE function from the discrete values. Based on the above discussion, a stepwise linear DOE function is defined and applied for the composite considered and also included in the figure.

In this case, only the three-phase Mori-Tanaka model is applicable for comparison since the interphase model is restricted to one inclusion phase. For the CNF/epoxy system considered, the bulk elastic stiffness of the matrix is 1.95 GPa. The matrix Poisson's ratio is not given but set to 0.35. Moreover, the CNFs are said to have a diameter of 100–200 nm and a length of 10–30 μm . The CNF aspect ratio is therefore set to 150 in our calculations. Furthermore, the elastic modulus of the CNFs is set to 200 GPa, and Poisson's ratio is set to 0.20. Finally, for the agglomerates, the measured average elastic stiffness is 4.2 GPa and Poisson's ratio is set to 0.35, which is equal to the matrix.

The three-phase Mori-Tanaka model results together with the stiffness values from Gershon et al. are shown in Figure 10(a) [5]. As can be observed, the Mori-Tanaka model agrees very well with the Gershon et al. calculations. It should also be noted that a slightly higher DOE value for the higher volume fractions would have given an even better match for all volume fractions in the range. However, this would have required a much higher DOE than that calculated by Gershon et al.

6.2. MWCNT/Polystyrene Composite. In this second case, we consider a MWCNT/polystyrene composite. Experimental values are reported by Andrews et al. [57]. Only the polystyrene elastic stiffness is given in the paper; that is, $E_m = 1.9$ GPa [57]. However, representative parameter values, which are needed for the modeling, can be found elsewhere in the literature. From the work by Shi et al. [41], who considered the same system, Poisson's ratio for polystyrene is given; $\nu_m = 0.3$. For the MWCNTs, the values are taken from the work of Lu [58]; $E_{\text{CNT}} = 975$ GPa and $\nu_{\text{CNT}} = 0.27$. The aspect ratio of the MWCNTs is set to 1000, based on the length and diameter range reported by Andrews et al. [57].

First, we investigate the applicability of the two-phase Mori-Tanaka model, the interphase model, and the modified Halpin-Tsai equation for randomly oriented fibers. The results are given in Figure 11 [57]. It can be seen that the model results agree with the calculated stiffness reported by Shi et al. [41, 42] for the same nanocomposite. Also, the Mori-Tanaka model and the interphase model with zero interphase thickness, that is, $n = 1$, result in overlapping stiffness curves. (The interphase model curve is not shown in the plot.) This shows that the averaging strategy employed for the extended version of the interphase model should be valid. Moreover, an interphase thickness factor larger than one and a reduced stiffness of the interphase region do not reduce the composite stiffness significantly. Hence, both model approaches overestimate the composite elastic stiffness compared to the experimental data. This could partly be due to a less than perfect dispersion of the MWCNTs in the experiments conducted by Andrews et al. [57], that

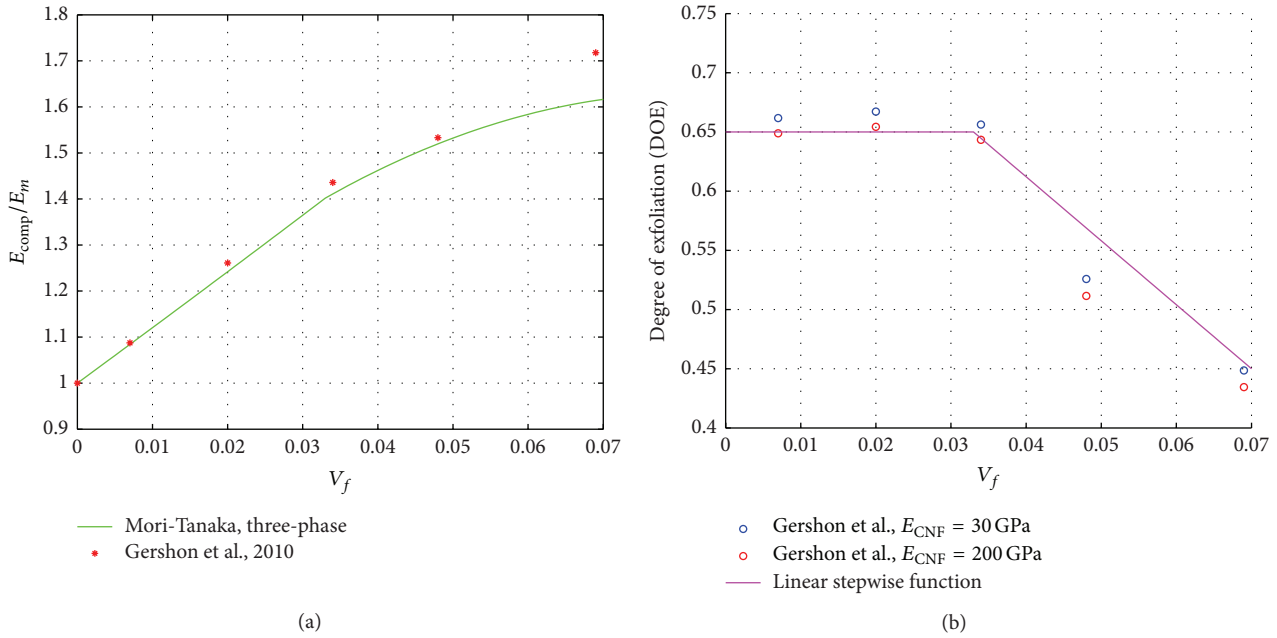


FIGURE 10: Model results for the CNF/epoxy composite in Gershon et al. [5]. (a) Composite elastic stiffness as a function of particle volume fraction; (b) DOE curve for the CNF/epoxy.

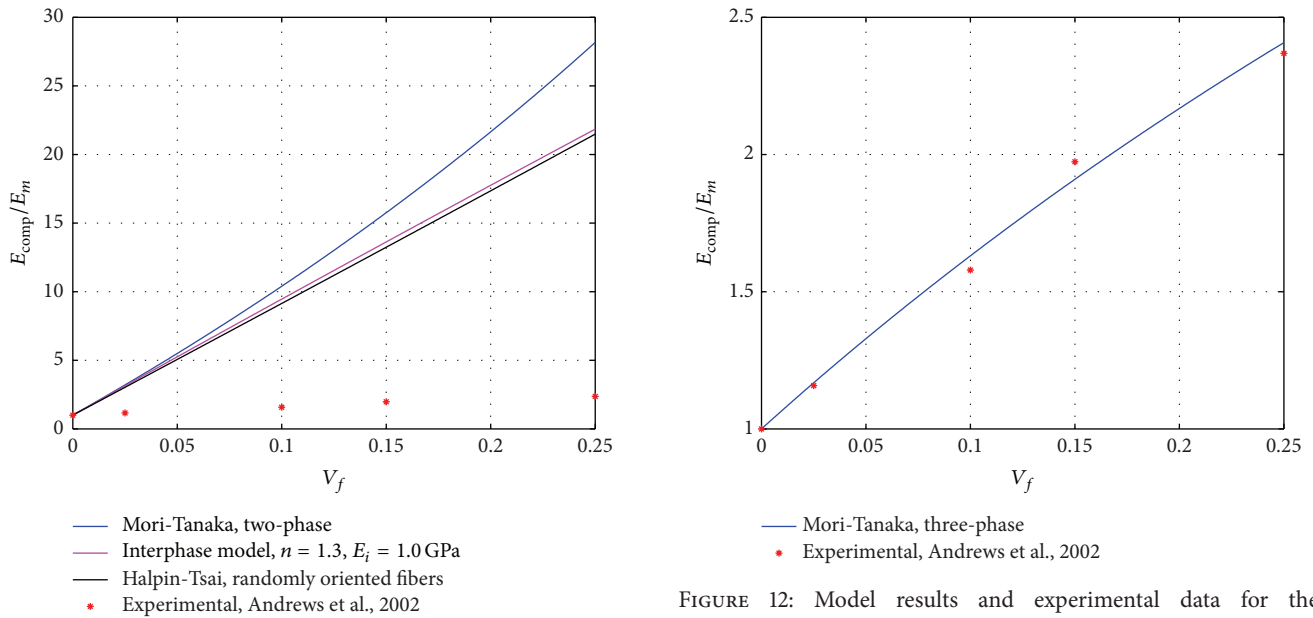


FIGURE 11: Model results and experimental data for the MWCNT/polystyrene composite in Andrews et al. [57]. Composite elastic stiffness as a function of particle volume fraction.

FIGURE 12: Model results and experimental data for the MWCNT/polystyrene composite in Andrews et al. [57]. Composite elastic stiffness as a function of particle volume fraction using the three-phase Mori-Tanaka model with voids.

is, $DOE < 1$. Finally, the modified Halpin-Tsai equation also overestimates the elastic stiffness.

From the above case, other effects than the interphase effects seem to significantly affect the composite stiffness in this case. We therefore instead apply the three-phase Mori-Tanaka model. Figure 12 [57] displays the model results and

the experimental data. To get agreement with the experimental results, the elastic stiffness of the agglomerated areas is set to zero, that is, assuming that the agglomerated MWCNTs do not contribute to the composite stiffness. Hence, the agglomerates are considered to be voids in the model. In this case, an assumed constant degree of exfoliation of 0.1 for all

volume fractions gives good correlation between the model and the experimental results.

6.3. Discussion. The first observation from the study of the two nanocomposites with fiber-like inclusions is that significant stiffness improvements can be obtained if the inclusions with extreme mechanical properties and high aspect ratio are perfectly dispersed in the matrix. This conclusion seems to yield even for the case of reduced load transfer at the interphase. The second observation is that the composite stiffness is significantly reduced due to agglomerates of the particles. But even a small amount of dispersed particles, that is, a very low value of the degree of exfoliation, will give a stiffness increase.

Considering the models and the experimental data, only the three-phase Mori-Tanaka model is applicable and relevant for composites with agglomerates. For the results presented by Gershon et al. and shown in Section 6.1, the volume fraction of the CNFs included in the agglomerates was found to give a stiffness increase compared to the bulk matrix. For the results presented by Andrews et al. [57], the agglomerates, on the other hand, seem not to improve the composite stiffness, but rather being the main factor for the large stiffness reduction (compared to the perfect dispersion case).

For the MWCNT/polystyrene case, the large stiffness reduction due to the agglomerates may not be in accordance with the results reported by Andrews et al., where the structural imperfections and impurities for the as-received MWCNTs were said to be removed (by heating to graphitization temperatures) before making the MWCNT/polystyrene composite of the well-dispersed MWCNTs. The model results presented here may therefore give some new insight. Our calculations have shown that a well-dispersed composite with optimal load transfer may actually not be the case. One parameter that can be changed in the calculations, to help support the conclusions by Andrews et al., is the elastic stiffness of the MWCNTs. A stiffness reduction of the MWCNTs from 975 GPa to 450 GPa is found to dramatically reduce the composite stiffness. The stiffness does, however, not seem to be significantly affected by the variation in aspect ratio in the same way; a reduction of the aspect ratio from 1000 to 250 is not found to significantly reduce the composite stiffness.

7. Summary and Conclusion

In this paper, the main objective has been on identifying models that are relevant to include in a “model toolbox” for estimation of different nanocomposites with varying geometry and constituent materials with different properties. Different mathematical models are described for the elastic modulus of nanoparticle/epoxy systems. Agglomerates and particle interphase properties are two relevant factors for the elastic stiffness increase. A set of flexible models for nanocomposites have been described, which are relevant in multiscale modeling, including finite element method analyses, of advanced high-performance composite structures. Extensions of the models are also presented to include more flexibility in the choice of particle geometry and orientation.

The suggested models for modeling of the nanocomposites, that is, the multiphase Mori-Tanaka model and the Odegard et al. interphase model, are composite system independent models containing a few general model parameters with a clear physical meaning. For the interphase model, only two parameters are included: the interphase thickness factor and the interphase elastic stiffness.

For the three nanosilica/epoxy systems considered, the calculated stiffness using the Mori-Tanaka model and the interphase model was compared to the experimental results, as well as the results from using the Halpin-Tsai equation and the slippage model by Lewis and Nielsen. Due to differences in the applied polymer systems, different stiffness increases were obtained for the nanocomposites. From adjusting the model parameters, the interphase model was found to agree well for all three systems, both for low and high volume fractions. Moreover, the two-phase Mori-Tanaka model agreed well for systems where the interphase properties do not seem to be significant for the stiffness increase. The Halpin-Tsai equation was applicable for predicting the stiffness increase for the anhydride-cured system, but not for the two other composites. The Lewis-Nielsen model only seems to give some kind of average stiffness for all volume fractions.

The calculated stiffness increase from employing the interphase model, the Halpin-Tsai equation, and the general multiphase Mori-Tanaka model was also compared to experimental and model results for a CNF/epoxy composite and a MWCNT/polystyrene composite. For fiber-like particles, the interphase properties seem to be less important for the stiffness increase, compared to other factors. One reason may be that the fiber-like particles are entangled, resulting in agglomerates with less or no stiffness contribution. The three-phase Mori-Tanaka model was found to agree well with the results for both nanocomposites considered.

As a final and overall conclusion, the multiphase Mori-Tanaka model and the Odegard et al. interphase model are found to be flexible, system independent, and applicable for calculating the elastic stiffness properties of the various nanocomposites, including both low and high volume fractions. These models are therefore preferred over more traditional models in estimation of the macroscopic elastic stiffness of multiphase nanocomposites.

Conflict of Interests

The authors declare that there is no conflict of interests regarding the publication of this paper.

Acknowledgments

The authors would like to thank Dr. Marie Bourgeaux-Goget for assistance with the experimental work. The authors would also like to thank Dr. Cato Dørum and Tomas Roll Frømyr for discussions and valuable input.

References

- [1] S.-Y. Fu, X.-Q. Feng, B. Lauke, and Y.-W. Mai, “Effects of particle size, particle/matrix interface adhesion and particle loading

- on mechanical properties of particulate-polymer composites,” *Composites Part B: Engineering*, vol. 39, no. 6, pp. 933–961, 2008.
- [2] D. R. Paul and L. M. Robeson, “Polymer nanotechnology: nanocomposites,” *Polymer*, vol. 49, no. 15, pp. 3187–3204, 2008.
 - [3] A. C. Taylor, “Adhesives with nanoparticles,” in *Handbook of Adhesion Technology*, L. F. da Silva, A. Öchsner, and R. D. Adams, Eds., pp. 1437–1460, Springer, Berlin, Germany, 2011.
 - [4] B. H. Cipriano, A. K. Kota, A. L. Gershon et al., “Conductivity enhancement of carbon nanotube and nanofiber-based polymer nanocomposites by melt annealing,” *Polymer*, vol. 49, no. 22, pp. 4846–4851, 2008.
 - [5] A. L. Gershon, D. P. Cole, A. K. Kota, and H. A. Bruck, “Nanomechanical characterization of dispersion and its effects in nano-enhanced polymers and polymer composites,” *Journal of Materials Science*, vol. 45, no. 23, pp. 6353–6364, 2010.
 - [6] H. Zhang, Z. Zhang, K. Friedrich, and C. Eger, “Property improvements of in situ epoxy nanocomposites with reduced interparticle distance at high nanosilica content,” *Acta Materialia*, vol. 54, no. 7, pp. 1833–1842, 2006.
 - [7] T. D. Fornes and D. R. Paul, “Modeling properties of nylon 6/clay nanocomposites using composite theories,” *Polymer*, vol. 44, no. 17, pp. 4993–5013, 2003.
 - [8] J. N. Coleman, U. Khan, W. J. Blau, and Y. K. Gun’ko, “Small but strong: a review of the mechanical properties of carbon nanotube-polymer composites,” *Carbon*, vol. 44, no. 9, pp. 1624–1652, 2006.
 - [9] T. H. Hsieh, A. J. Kinloch, K. Masania, A. C. Taylor, and S. Sprenger, “The mechanisms and mechanics of the toughening of epoxy polymers modified with silica nanoparticles,” *Polymer*, vol. 51, no. 26, pp. 6284–6294, 2010.
 - [10] F. Fisher and L. C. Brinson, “Nanomechanics of nanoreinforced polymers,” in *Handbook of Theoretical and Computational Nanotechnology: Functional Nanomaterials, Nanoparticles, and Polymer Design*, M. Rieth and W. Schommers, Eds., pp. 253–360, American Scientific Publishers, 2006.
 - [11] D. Srivastava, C. Wei, and K. Cho, “Nanomechanics of carbon nanotubes and composites,” *Applied Mechanics Reviews*, vol. 56, no. 2, pp. 215–230, 2003.
 - [12] B. D. Agarwal, L. J. Broutman, and K. Chandrashekhara, *Analysis and Performance of Fiber Composites*, John Wiley & Sons, 3rd edition, 2006.
 - [13] H. L. Cox, “The elasticity and strength of paper and other fibrous materials,” *British Journal of Applied Physics*, vol. 3, no. 3, pp. 72–79, 1952.
 - [14] J. D. Fidelus, E. Wiesel, F. H. Gojny, K. Schulte, and H. D. Wagner, “Thermo-mechanical properties of randomly oriented carbon/epoxy nanocomposites,” *Composites Part A: Applied Science and Manufacturing*, vol. 36, no. 11, pp. 1555–1561, 2005.
 - [15] T. Thorvaldsen, “A model study of the effective Young’s modulus for randomly distributed short-fiber composites,” FFI Report 2011/00212, 2011.
 - [16] L. J. Cohen and O. Ishai, “The elastic properties of three-phase composites,” *Journal of Composite Materials*, vol. 1, no. 4, pp. 390–403, 1967.
 - [17] O. Ishai and L. J. Cohen, “Elastic properties of filled and porous epoxy composites,” *International Journal of Mechanical Sciences*, vol. 9, no. 8, pp. 539–546, 1967.
 - [18] G. P. Tandon and G. J. Weng, “The effect of aspect ratio of inclusions on the elastic properties of unidirectionally aligned composites,” *Polymer Composites*, vol. 5, no. 4, pp. 327–333, 1984.
 - [19] G. J. Weng, “Some elastic properties of reinforced solids, with special reference to isotropic ones containing spherical inclusions,” *International Journal of Engineering Science*, vol. 22, no. 7, pp. 845–856, 1984.
 - [20] Y. P. Qiu and G. J. Weng, “On the application of Mori-Tanaka’s theory involving transversely isotropic spheroidal inclusions,” *International Journal of Engineering Science*, vol. 28, no. 11, pp. 1121–1137, 1990.
 - [21] B. Paul, “Prediction of elastic constants of multiphase materials,” *Transactions of the Metallurgical Society of AIME*, vol. 218, pp. 36–41, 1960.
 - [22] G. P. Tandon and G. J. Weng, “Average stress in the matrix and effective moduli of randomly oriented composites,” *Composites Science and Technology*, vol. 27, no. 2, pp. 111–132, 1986.
 - [23] J. C. Halpin and J. L. Kardos, “The Halpin-Tsai equations: a review,” *Polymer Engineering and Science*, vol. 16, no. 5, pp. 344–352, 1976.
 - [24] J. C. Halpin, “Stiffness and expansion estimates for oriented short fiber composites,” *Journal of Composite Materials*, vol. 3, pp. 732–734, 1969.
 - [25] J. C. Halpin and N. J. Pagano, “The laminate approximation for randomly oriented fibrous composites,” *Journal of Composite Materials*, vol. 3, no. 4, pp. 720–724, 1969.
 - [26] G. Swaminathan, M. Hossain, and K. N. Shivakumar, “Mechanical characterization of nanosilica/epoxy nanocomposites,” in *Proceedings of the 51st AIAA/ASME/ASCE/AHS/ASC Structures, Structural Dynamics, and Materials Conference*, Orlando, Fla, USA, April 2010.
 - [27] T. Gómez-del Río, P. Poza, J. Rodríguez, M. C. García-Gutiérrez, J. J. Hernández, and T. A. Ezquerro, “Influence of single-walled carbon nanotubes on the effective elastic constants of poly(ethylene terephthalate),” *Composites Science and Technology*, vol. 70, no. 2, pp. 284–290, 2010.
 - [28] T. Mura, *Micromechanics of Defects in Solids*, Martinus Nijhoff, The Hague, The Netherlands, 1982.
 - [29] T. Mori and K. Tanaka, “Average stress in matrix and average elastic energy of materials with misfitting inclusions,” *Acta Metallurgica*, vol. 21, no. 5, pp. 571–574, 1973.
 - [30] J. D. Eshelby, “Elastic inclusions and inhomogeneities,” in *Progress in Solid Mechanics*, I. N. Sneddon and R. Hill, Eds., vol. 2, pp. 89–140, North-Holland, Amsterdam, The Netherlands, 2 edition, 1961.
 - [31] J. D. Eshelby, “The determination of the elastic field of an ellipsoidal inclusion, and related problems,” *Proceedings of the Royal Society of London. Series A. Mathematical, Physical and Engineering Sciences*, vol. 241, no. 1226, pp. 376–396, 1957.
 - [32] C. L. Tucker III and E. Liang, “Stiffness predictions for unidirectional short-fiber composites: review and evaluation,” *Composites Science and Technology*, vol. 59, no. 5, pp. 655–671, 1999.
 - [33] C. Weinberger, W. Cai, and D. Barnett, *Lecture Notes—Elasticity of Microscopic Structures*, ME340B, Stanford University, 2004.
 - [34] T. Thorvaldsen, “Modeling the elastic stiffness of nanocomposites using the Mori-Tanaka method,” FFI Report 2014/00494, 2014.
 - [35] F. T. Fisher, R. D. Bradshaw, and L. C. Brinson, “Fiber waviness in nanotube-reinforced polymer composites—I: modulus predictions using effective nanotube properties,” *Composites Science and Technology*, vol. 63, no. 11, pp. 1689–1703, 2003.
 - [36] T. B. Lewis and L. E. Nielsen, “Dynamic mechanical properties of particulate-filled composites,” *Journal of Applied Polymer Science*, vol. 14, no. 6, pp. 1449–1471, 1970.

- [37] S. McGee and R. L. McGullough, "Combining rules for predicting the thermoelastic properties of particulate filled polymers, polymers, polyblends, and foams," *Polymer Composites*, vol. 2, no. 4, pp. 149–161, 1981.
- [38] A. P. Holt, P. J. Griffin, V. Bocharova et al., "Dynamics at the polymer/nanoparticle interface in poly(2-vinylpyridine)/silica nanocomposites," *Macromolecules*, vol. 47, no. 5, pp. 1837–1843, 2014.
- [39] G. M. Odegard, T. C. Clancy, and T. S. Gates, "Modeling of the mechanical properties of nanoparticle/polymer composites," *Polymer*, vol. 46, no. 2, pp. 553–562, 2005.
- [40] M. L. Dunn and H. Ledbetter, "Elastic moduli of composites reinforced by multiphase particles," *Journal of Applied Mechanics*, vol. 62, no. 4, pp. 1023–1028, 1995.
- [41] D.-L. Shi, X.-Q. Feng, Y. Y. Huang, K.-C. Hwang, and H. Gao, "The effect of nanotube waviness and agglomeration on the elastic property of carbon nanotube-reinforced composites," *Journal of Engineering Materials and Technology*, vol. 126, no. 3, pp. 250–257, 2004.
- [42] D.-L. Shi, X.-Q. Feng, Y. Y. Huang, and K.-C. Hwang, "Critical evaluation of the stiffening effect of carbon nanotubes in composites," *Key Engineering Materials*, vol. 261–263, pp. 1487–1492, 2004.
- [43] R. M. Jones, *Mechanics of Composite Materials*, Taylor & Francis, Philadelphia, Pa, USA, 1999.
- [44] B. B. Johnsen, M. Bourgeaux-Goget, and T. Olsen, "Material properties of silica/epoxy nanocomposites," FFI Report 2015/00366, 2015.
- [45] S. Sprenger, "Personal communication," 2014.
- [46] ASTM, "Standard test methods for density and specific gravity (relative density) for plastics by displacement," ASTM D792-08, 2008.
- [47] International Organization for Standardization, "Plastics—determination of tensile properties—part 1: general principles," ISO 527-1:2012, International Organization for Standardization, London, UK, 2012.
- [48] International Organization for Standardization, "Plastics—determination of tensile properties—part 2: test conditions for moulding and extrusion plastics," International Organization for Standardization 527-2:1996, 1996.
- [49] F. Meyer, G. Sanz, A. Eceiza, I. Mondragon, and J. Mijović, "The effect of stoichiometry and thermal history during cure on structure and properties of epoxy networks," *Polymer*, vol. 36, no. 7, pp. 1407–1414, 1995.
- [50] Y.-L. Liu, C.-Y. Hsu, W.-L. Wei, and R.-J. Jeng, "Preparation and thermal properties of epoxy-silica nanocomposites from nanoscale colloidal silica," *Polymer*, vol. 44, no. 18, pp. 5159–5167, 2003.
- [51] S. Torquato and F. Lado, "Effective properties of two-phase disordered composite media: II. Evaluation of bounds on the conductivity and bulk modulus of dispersions of impenetrable spheres," *Physical Review B*, vol. 33, no. 9, pp. 6428–6435, 1986.
- [52] S. Torquato, "Nearest-neighbor statistics for packings of hard spheres and disks," *Physical Review E*, vol. 51, no. 4, pp. 3170–3182, 1995.
- [53] J. Karger-Kocsis and Z. Zhang, "Structure-property relationships in nanoparticle/semicrystalline thermoplastic composites," in *Mechanical Properties of Polymers based on Nanostructure and Morphology*, G. H. Michler and F. J. Baltá-Calleja, Eds., pp. 553–602, Taylor & Francis Group, 2005.
- [54] B. B. Johnsen, A. J. Kinloch, R. D. Mohammed, A. C. Taylor, and S. Sprenger, "Toughening mechanisms of nanoparticle-modified epoxy polymers," *Polymer*, vol. 48, no. 2, pp. 530–541, 2007.
- [55] T. R. Frømyr, M. Bourgeaux-Goget, and F. K. Hansen, "A comparative study of the dispersion of multi-wall carbon nanotubes made by arc-discharge and chemical vapour deposition," *Journal of Nanoscience and Nanotechnology*, vol. 15, no. 5, pp. 3496–3506, 2015.
- [56] C. Antonelli, B. Serrano, J. Baselga, R. Ozisik, and J. C. Cabanelas, "Interfacial characterization of epoxy/silica nanocomposites measured by fluorescence," *European Polymer Journal*, vol. 62, pp. 31–42, 2015.
- [57] R. Andrews, D. Jacques, M. Minot, and T. Rantell, "Fabrication of carbon multiwall nanotube/polymer composites by shear mixing," *Macromolecular Materials and Engineering*, vol. 287, no. 6, pp. 395–403, 2002.
- [58] J. P. Lu, "Elastic properties of carbon nanotubes and nanoropes," *Physical Review Letters*, vol. 79, no. 7, pp. 1297–1300, 1997.